

# ABSTRACT

Title of Thesis: **INTERACTION OF ACOUSTIC WAVES  
WITH A LAMINAR LINE-FLAME**

Adam N. Friedman, Master of Science, 2016

Thesis directed by: Professor Stanislav I. Stoliarov  
Department of Fire Protection Engineering

A systematic study was conducted to elucidate the effects of acoustic perturbations on laminar diffusion line-flames and the conditions required to cause acoustically-driven extinction. Flames were produced from the fuels n-pentane, n-hexane, n-heptane, n-octane, and JP-8, using fuel-laden wicks. The wicks were housed inside of a burner whose geometry produced flames that approximated a two dimensional flame sheet. The acoustics utilized ranged in frequency between 30-50 Hz and acoustic pressures between 5-50 Pa. The unperturbed mass loss rate and flame height of the alkanes were studied, and they were found to scale in a linear manner consistent with Burke-Schumann. The mass loss rate of hexane-fueled flames experiencing acoustic perturbations was then studied. It was found that the strongest influence on the mass loss rate was the magnitude of oscillatory air movement experienced by the flame. Finally, acoustic perturbations were imposed on flames using all fuels to determine acoustic extinction criterion. Using the data collected, a model was developed which characterized the acoustic conditions required to cause flame extinction. The model was based on the ratio of an acoustic Nusselt Number to the Spalding B Number of the fuel, and it was found that at the minimum speaker power required to cause extinction this ratio was a constant. Furthermore, it was found that at conditions where the ratio was below this constant, a flame could still exist; at conditions where the ratio was greater than or equal to this constant, flame extinction always occurred.

# Interaction of Acoustic Waves with a Laminar Line-Flame

by

Adam N. Friedman

Thesis submitted to the Faculty of the Graduate School of the  
University of Maryland, College Park in partial fulfillment  
of the requirements for the degree of

Master of Science

2016

**Advisory Committee:**

Professor Stanislav I. Stoliarov, Chair

Professor Michael J. Gollner

Professor Andre W. Marshall

© Copyright by  
Adam N. Friedman  
2016

All rights reserved. No part of this work may be reproduced or transmitted in any form or by any means, electronic or mechanical, including photocopying, recording, or by any information storage and retrieval system, without permission in writing from the author.

*Dedicated to Zaydie...*

# *Acknowledgements*

This project has required considerable help from many people along the way, and there isn't enough room to thank them all. I would especially like to thank though Dr. Ed Hattour and Mr. Brent Mills from the U.S. Army Research Lab. This project would not have been possible without them, and their efforts on my behalf have truly been appreciated. I would also like to thank the Federal Aviation Administration for providing the initial funding for this project. Lastly, I would like to give a special thanks to my adviser, Dr. Stanislav Stoliarov. He graciously indulged my idiosyncrasies while guiding me through the process of producing quality research and succinct writing.

This research was supported in part by an appointment to the Student Research Participation Program at the U.S. Army Research Laboratory administered by the Oak Ridge Institute for Science and Education through an inter-agency agreement between the U.S. Department of Energy and USARL

# Contents

<b>Acknowledgements</b>	<b>iii</b>
<b>List of Figures</b>	<b>vii</b>
<b>List of Tables</b>	<b>ix</b>
<b>Physical Constants</b>	<b>x</b>
<b>Symbols</b>	<b>xi</b>
<b>1 Introduction</b>	<b>1</b>
1.1 Motivation . . . . .	1
1.2 Background . . . . .	2
1.2.1 Flame Extinction . . . . .	2
1.2.2 Interaction of Acoustics and Flames . . . . .	5
1.3 Scope of Work . . . . .	11
<b>2 Testing Apparatus</b>	<b>13</b>
2.1 Overview . . . . .	13
2.2 Acoustic Source . . . . .	15
2.2.1 Signal generation . . . . .	15
2.2.2 Sub-Woofer . . . . .	15
2.3 Burner . . . . .	17
2.4 Testing Enclosure . . . . .	19
<b>3 Data Acquisition</b>	<b>23</b>
3.1 Overview . . . . .	23
3.2 Acoustic Pressure . . . . .	24
3.2.1 Microphone Calibration . . . . .	24
3.3 Anemometry . . . . .	26
3.4 High Speed Video . . . . .	26
3.5 Mass Readings . . . . .	27

<b>4</b>	<b>System Characterization</b>	<b>28</b>
4.1	Overview . . . . .	28
4.2	System Harmonics . . . . .	28
4.2.1	Predicted Resonant Frequencies . . . . .	29
4.2.2	Observed Resonant Frequencies . . . . .	30
4.2.3	Comparison of Predicted and Observed Resonance . . . . .	33
4.3	Pressure Scaling . . . . .	33
4.4	Acoustic Pressure Profiles . . . . .	37
4.4.1	Profiles Without Burner . . . . .	37
4.4.2	Profiles with Burner . . . . .	37
4.4.3	Comparison of Profiles . . . . .	39
4.5	Acoustically Induced Flows . . . . .	41
4.5.1	PIV Analysis of Acoustic Flow . . . . .	41
<b>5</b>	<b>Free Burn Characterization</b>	<b>47</b>
5.1	Overview . . . . .	47
5.2	Mass Loss Rate . . . . .	48
5.3	Flame Height . . . . .	50
5.4	Flame Width . . . . .	56
5.5	Flame Height Scaling . . . . .	58
<b>6</b>	<b>Burning Rate in an Acoustic Field</b>	<b>61</b>
6.1	Overview . . . . .	61
6.2	MLR Profiles . . . . .	63
6.3	MLR Profile Comparisons . . . . .	66
6.3.1	Comparable Acoustic Pressures . . . . .	66
6.3.2	Comparable Air Speeds . . . . .	67
6.3.3	Average Mass Loss Rates . . . . .	69
<b>7</b>	<b>Acoustic Extinction</b>	<b>72</b>
7.1	Experimental Summary . . . . .	72
7.1.1	Acoustic Extinction Results . . . . .	72
7.1.2	Fan-Driven Extinction Results . . . . .	75
7.2	Proposed Acoustic Extinction Theory . . . . .	76
7.2.1	Comparison of Results . . . . .	76
7.2.2	Discussion of Results . . . . .	77
7.2.3	Heuristic Framework . . . . .	80
7.2.4	Proposed Extinction Criterion . . . . .	81
7.3	B - Mass Transfer Number . . . . .	83
7.3.1	Fuel Specific Parameters . . . . .	83
7.3.2	Air Properties . . . . .	86
7.3.3	B Number Calculation . . . . .	87

7.4	Nusselt Number Correlation . . . . .	88
7.4.1	Reynolds Number . . . . .	88
7.4.2	Mathematical Formulation . . . . .	88
7.4.3	Modified Nusselt Number . . . . .	89
7.4.4	Exponent of Best Fit . . . . .	90
7.5	Calculated Values of $\Theta'$ . . . . .	91
7.5.1	Acoustic Results . . . . .	91
7.5.2	Hypo and Hyper Critical Values . . . . .	92
7.5.3	Fan Driven Results . . . . .	94
7.6	Limitations and Considerations . . . . .	96
7.6.1	System Limitations . . . . .	96
7.6.2	Considerations of Applicability . . . . .	97
<b>8</b>	<b>Conclusions</b>	<b>101</b>
<b>A</b>	<b>Error Analysis</b>	<b>105</b>
A.1	Data Uncertainties . . . . .	105
A.2	Fuel Parameter Uncertainties . . . . .	108
A.2.1	Model Uncertainties . . . . .	108
A.2.2	Uncertainties in Acoustic Analysis . . . . .	109
A.2.3	Uncertainties in Fan Driven Analysis . . . . .	110
<b>B</b>	<b>Product Data Sheets</b>	<b>112</b>
B.1	Agilent 3220A Function Generator . . . . .	112
B.2	Infinity Reference 860w 8" Woofer . . . . .	116
B.3	AE Techron 8102 Amplifier . . . . .	118
B.4	Kaowool Ceramic Insulation . . . . .	120
B.5	BSWA MPA 231 Microphone . . . . .	122
B.6	BSWA MC102 Signal Conditioner . . . . .	123
B.7	BSWA CA111 Calibrator . . . . .	124
B.8	Tektronix 2024C Digital Oscilloscope . . . . .	125
B.9	Extech Termo-Anemometer . . . . .	128
B.10	Phantom High Speed Camera . . . . .	129
B.11	Mettler Toledo Precision Balance . . . . .	132
	<b>Bibliography</b>	<b>134</b>

# List of Figures

2.1	Testing Apparatus Overview . . . . .	14
2.2	Plan and View of Woofer Sabot . . . . .	16
2.3	Speaker Sabot Placement . . . . .	17
2.4	Burner Plan . . . . .	18
2.5	Burner Assembly Sequence . . . . .	20
2.6	Views of Flame Sheet . . . . .	21
2.7	Plan of Testing Enclosure . . . . .	21
2.8	Views of Testing Enclosure . . . . .	22
2.9	Equipment Placement . . . . .	22
3.1	Burner Balance Stand . . . . .	27
4.1	1 <sup>st</sup> Harmonic Tube Interior . . . . .	31
4.2	2 <sup>nd</sup> Harmonic Tube Interior . . . . .	31
4.3	3 <sup>rd</sup> Harmonic Tube Interior . . . . .	32
4.4	1 <sup>st</sup> Harmonic Tube Exterior . . . . .	34
4.5	2 <sup>nd</sup> Harmonic Tube Exterior . . . . .	34
4.6	3 <sup>rd</sup> Harmonic Tube Exterior . . . . .	35
4.7	Exterior Acoustic Pressure Decay . . . . .	36
4.8	Pressure Profiles Without Burner . . . . .	38
4.9	Pressure Profile Placement Schematic . . . . .	39
4.10	Pressure Profiles With Burner . . . . .	40
4.11	Air Speed vs Acoustic Pressure . . . . .	42
4.12	PIVLab Output . . . . .	45
4.13	PIV Calculated Velocity Components . . . . .	45
4.14	PIV vs. Anemometer . . . . .	46
5.1	Alkane MLR Profiles . . . . .	49
5.2	Flame Height Video Sample . . . . .	51
5.3	Flame Height ROI . . . . .	51
5.4	Hexane Flame Luminous Intensity Profiles . . . . .	53
5.5	Flame Height Determination . . . . .	54
5.6	Alkane Flame Height Profiles . . . . .	55

5.7	Flame Width Determination . . . . .	57
5.8	MLR and Flame Height . . . . .	58
5.9	Flame Height vs. HRR' . . . . .	59
6.1	Burner on Balance . . . . .	62
6.2	Hexane MLR Profiles with Acoustics . . . . .	64
6.3	Hexane MLR Profiles with Fan Driven Flow . . . . .	65
6.4	MLR Profiles at Comparable Pressures . . . . .	67
6.5	MLR Profiles at Comparable Air Speeds . . . . .	68
6.6	Average MLR's . . . . .	71
7.1	Average Values of $P$ and $U_A$ at Extinction . . . . .	74
7.2	Heptane Extinction Boundaries . . . . .	75
7.3	Average Values of $U_F$ at Extinction . . . . .	76
7.4	Comparison of Acoustic and Fan Extinction Flows . . . . .	78
7.5	Fan-Drive Flow Visualization . . . . .	79
7.6	Flame Displacement Sequence . . . . .	82
7.7	Coefficient of Variation for Model . . . . .	91
7.8	Calculated Values of $\Theta'_{A_{ext}}$ . . . . .	92
7.9	Hypo and Hyper Critical Extinction Data Points . . . . .	94
7.10	Calculated Values of $\Theta'_F$ . . . . .	95
7.11	Speaker and Acoustic Wave Power . . . . .	97
7.12	Ratio of acoustic power to speaker power . . . . .	97
7.13	Ratio of $\ell$ to $w_b$ . . . . .	99

# List of Tables

4.1	Calculated Resonant Frequencies . . . . .	30
4.2	Predicted and Measured Resonant Frequencies . . . . .	32
4.3	Pressure Profile Comparison . . . . .	41
5.1	Flame Height Data Structure . . . . .	52
7.1	Acoustic Flame Extinction Test Results . . . . .	73
7.2	Fan-Driven Flame Extinction Test Results . . . . .	76
7.3	Selected Properties of Fuels and Gases . . . . .	85
7.4	Selected Properties of Air for Different Fuels . . . . .	87
7.5	Calculated Fuel Properties . . . . .	87
7.6	Analysis of Hypo and Hyper Critical Extinction Conditions . . . . .	93
A.1	Uncertainty Analysis Data Structure . . . . .	106

# Physical Constants

Constant Name	Symbol	Constant Value
Speed of Sound	$c_s$	340.3 m/s
Ambient Air Temperature	$T_\infty$	298 K
Ambient Air Density	$\rho_\infty$	1.23 kg/m <sup>3</sup>

# Symbols

Symbol	Name	Unit
$A$	Flam Height Scaling Factor	m/W
$a_E$	Extinction Strain Rate	1/s
$c_p$	Specific Heat	J/kg·K
$D$	Diameter	m
$\mathcal{D}$	Diffusivity	m <sup>2</sup> /s
dB	Decibels	
$e$	Correction Factor	m
$\Delta F$	Frame Smoothing Kernel	
$h_v$	Heat of Vaporization	J/kg
$\Delta H_c$	Heat of Combustion	J/mol
$\Delta h_c$	Heat of Combustion	J/kg
$\Delta h_{f,liq}^\circ$	Liquid Heat of Formation	J/kg
$\Delta h_{f,gas}^\circ$	Gaseous Heat of Formation	J/kg
$I$	Pixel Intensity	
$k$	Calibration Constant	Pa/mV
$L$	Latent Heat of Gassification	J/kg
$L_f$	Flame Height	m
$L_o$	Length of Acoustic Column	m
$\ell$	Characteristic Length	m
$\dot{m}$	Mass Loss Rate	kg/s
$\tilde{m}$	Average Mass Loss Rate	kg/s
$N$	Number of Elements in Set	
$n$	Harmonic Mode	
$P$	Pressure	Pa

$\dot{Q}$	Heat Release Rate	W
$r$	Stoichiometric Fuel to Air Ratio	
$S$	Uncertainty	
$T$	Temperature	K
$T_b$	Boiling Temperature	K
$U_A$	Acoustic <i>rms</i> air speed	m/s
$U_F$	Fan Driven Air Speed	m/s
$u$	$u$ Velocity Component	m/s
$V$	Voltage	V
$v$	$v$ Velocity Component	m/s
$W_f$	Flame Width	m
$w_b$	Burner Width	m
$x$	Distance	m
$Y$	Mass Fraction	
$y$	Distance	m
$Z$	Specific Acoustic Impedance	Pa·s/m
$z$	Distance	m
$\gamma$	Reynolds Number Exponent	
$\delta$	Prandtl Number Exponent	
$\Theta$	Acoustic Extinction Criterion	
$\lambda$	Wavelength	m
$\mu$	Arithmetic Mean	
$\nu$	Kinematic Viscosity	m <sup>2</sup> /s
$\rho$	Density	kg/m <sup>3</sup>
$\sigma$	Standard Deviation	
$\tau$	Characteristic Time	s
$\omega$	Frequency	Hz
$\omega_{R_n}$	Resonant Frequency of $n^{th}$ mode	Hz
B	Spalding Mass Transfer Number	
Da	Damköhler Number	
Nu	Nusselt Number	
Pr	Prandtl Number	

Re Reynolds Number

# Chapter 1

## Introduction

### 1.1 Motivation

Since the early 1900's halon has been used to effectively extinguish fires [1]. By the 1960's, halon began to see widespread use in the U.S. Military and quickly become one of its primary means for suppressing fires and explosions [2]. Due to the ozone depleting properties of halon though, the United States became a signatory to the Montreal Protocol in 1987, which effectively ended the production of halon worldwide [3]. In order to meet its present needs for halon, the U.S. Military maintains a reserve that is supplemented with product acquired from decommissioned systems.

With no new halon available, finding a suitable halon replacement technology has become an active area of research for the U.S. Military [2]. In August 2013, the

U.S. Army Research Lab (ARL) approached the Department of Fire Protection Engineering at the University of Maryland, College Park, to initiate a joint research project in the field of novel fire suppression. The objective of this research was to explore the feasibility of using acoustics to achieve flame extinction. Prior research funded by the Defense Advanced Projects Research Agency (DARPA) had explored acoustic flame suppression using gaseous fuel sources [4], and the proposed research was meant to be a continuation of DARPA's work. Of particular interest to ARL was whether acoustics could be used to suppress flames from a liquid fuel source and, if so, the development of a model that could predict the conditions required. The following work is the fulfillment of that research goal.

## **1.2 Background**

### **1.2.1 Flame Extinction**

In a general sense, diffusion flame extinction occurs when heat losses from a flame become sufficiently large that the heat released during combustion can no longer maintain a temperature which will sustain chemical kinetics [5]. In this context, Quintiere and Rangwala have proposed that for every flame there exists a critical temperature, below which flame extinction will occur [6]. Using this framework, a qualitative understanding of the conditions that cause flame extinction can be gained. For example, the introduction of a diluent reduces the oxidizer's

concentration, thereby reducing the chemical reaction and heat release rates (HRR) [7]; the application of liquid water not only cools a fuel source and inhibits pyrolysis, but also causes significant heat losses from the flame during the conversion process to steam [8]. Flame extinction occurs in both these examples because heat losses cause chemical kinetics to slow, which reduces the HRR, thereby further lowering temperatures in the flame and retarding chemical kinetics.

Chemical kinetics alone though do not fully explain extinction phenomenon [9]. Closely coupled with kinetics are heat and mass transport processes, and these are needed to create an environment where combustion chemistry can occur. The amount of strain (or stretch) experienced by the flame is of particular interest when considering transport processes, and there are multiple ways to conceptualize this.

If a diffusion flame is conceptualized in the context of a reactive flow, then it is useful to consider strain as a measure of the rate of deformation in the flow [10]. As strain in the reactant flow increases, the residence time of the reactants decreases [11]. This in turn has the effect of lowering both the reaction and HRR [11, 12].

If a diffusion flame is conceptualized in the context of a “cellular” entity with a surface, then it may be useful to consider strain in the context of flame stretch. In this context, flame stretch is a measure of curvature in the flame’s surface. As flame stretch increases, the symmetry between the fuel and oxidizer sides of the flame decreases, and this causes imbalances in heat and mass fluxes on either side of the flame sheet [13]. For steady state diffusion flames in particular, Liñán showed

through theoretical analysis that increased flame stretch caused increased heat losses from the flame on both sides of the reaction zone [14].

For unsteady flames it may also be useful to conceptualize flame stretch as the proportional rate of change in the flame's surface area with respect to time [15]. Using this conceptualization, Katta *et al* showed that the effects of stretch on the unsteady flame also created transport imbalances. In their study of an unsteady opposing jet flame, they found that as flame stretch increased, the amount of reactant that was able to enter the reaction zone also increased. The net effect was that while the HRR increased, there was also an increase in the amount of products from incomplete combustion. These products acted as a heat sink within the flame and actually lowered the flame's temperature [16].

With its multiple physical interpretations and strong effects on flame chemistry, flame stretch has become a commonly used criterion for predicting flame extinction [5, 9, 11, 12, 17–19]. Underlying all these interpretations, though, is the understanding that increased flame stretch enhances transport processes, which in turn competes with combustion chemical kinetics. Using an Asymptotic Energy Analysis (AEA), Lecoustre *et al* showed in fact that as flame stretch increased, the temperature required to sustain a diffusion flame also increased. Since the effects of transport processes and chemical kinetics are so closely coupled, it is often desirable to represent them in relationship to each other. Such a comparison is commonly done through the use of a Damköhler number.

The Damköhler number (Da) of a flame is generally defined as the ratio of a characteristic mixing (transport or residence) time ( $\tau_{mix}$ ) to a characteristic chemistry time ( $\tau_{chem}$ ) [5, 17–20]. Mathematically, this is expressed as  $Da = \tau_{mix} / \tau_{chem}$ . Rates, though, are inversely proportional to time, and it is sometimes useful to express the Damköhler number as  $Da = \text{rxn rate} / \text{mix rate}$ . For large values of Da, it is expected that the effects of slow transport processes will dominate, and flame chemistry will occur at a faster rate. As values of Da become smaller, though, the effects of increased transport rates and slower chemical kinetics begin to dominate until the system becomes non-reactive [20]. Therefore, for every flame there exists a critical value of Da, below which flame extinction will occur [5, 18, 21].

### **1.2.2 Interaction of Acoustics and Flames**

The interaction of acoustic waves and flames has been a field of study since the 1960's [22]. The primary focus of this early research was the effects of acoustics on droplet burning in turbine engines and combustion chambers; this continues to be an active field of research [5, 22–24]. The results of this research showed that acoustics do influence droplet combustion by altering the rates of heat and mass transfer [24]. Of particular interest in this field of study are the instabilities that form within a combustion chamber [5]. These instabilities can often lead to combustion inefficiencies and damage to the chamber [5, 25]. The causes of these phenomena are due to disturbances in the reaction flow field and are reviewed in detail by O'Connor *et al* [26].

Although acoustics can lead to inefficiencies during droplet combustion, they can also be used to enhance combustion. For example, during spray processes fuel droplets often break up into even smaller droplets, and some of these sub-droplets may be inhomogeneous with lower boiling temperatures. Rapid boiling of these sub-droplets can create micro-explosions which cause further droplet breakup and leads to instabilities within the reactor. Miglani *et al* found that the application of acoustics in the narrow bandwidth of 80 to 120 Hz could stabilize the fuel droplets and reduce the number of sub-droplets formed [27].

Acoustics can also be used to modulate the burning rate and combustion chemistry of fuel droplets. Sevilla-Esparza *et al* studied the droplet combustion of ethanol, methanol, JP-8, and a synthetic fuel at various frequencies within a standing wave. The acoustics were produced with two movable speakers, which allowed them to also study the droplets at different phase angles within the standing wave. Their results showed that the burning rate of each fuel was sensitive to both frequency and phase angle, and they attributed this sensitivity to the deflection angle of the droplet within the wave. By measuring OH\* chemiluminescence, they were also able to quantify the HRR for methanol droplets at different frequencies. They found that at low acoustic frequency, there was a strong coupling between the relative OH\* concentration and the acoustic pressure. As the acoustic frequency was increased, the strength of this coupling was seen to diminish. They concluded that the coupling was attributable to the magnitude of the velocity perturbations experienced by the droplet, which decreased as the acoustic frequency increased

[24].

Within the context of this research, there have also been investigations into the acoustically-driven extinction of droplet flames. McKinney and Dunn-Rankin studied this phenomenon using a streaming flow of methanol droplets. Droplets of various sizes were injected into a resonating tube and exposed to acoustic waves at various frequencies and pressures to identify extinction criteria. They found that at the same frequency, the acoustic pressure required to cause extinction increased with droplet size. They also found that for droplets of the same size, the acoustic pressure required to cause extinction increased with frequency. The authors determined that extinction occurred when the flame was displaced far enough from the droplet that evaporation was shut down. Key to their findings was that the magnitude of displacement had to be at least the radius of the droplet [23].

More recently, there has been a growing body of research on the interaction of acoustics with both premixed and diffusion flames using gaseous fuel sources [4, 21, 28–34]. The breadth of this research has included a myriad of topics such as pollutant reduction [32], combustion instabilities [34], and even acoustic flame extinction [4, 21, 31]. Key to this research has been the need to understand the effects of an oscillatory strain rate on a flame. Of particular interest are the effects when a flame is near its extinction limit, where flames show an increased sensitivity to acoustic excitations [28].

The response of a flame to acoustic excitations can be classified as either linear or non-linear with respect to the excitation frequency [33]. Kim and Williams studied linear responses and acoustic extinction criteria by applying a theoretical analysis to a counter-flow diffusion flame. In their analysis, they adopted the model developed by Liñán, where the reactive layer is shifted to the oxidizer side of the stagnation plane and sandwiched between two convective-diffusive layers [14]. They then considered the effects of acoustic perturbations on the reactive layer in the frequency range of  $10^3$ - $10^4$  Hz, which is on the same order of magnitude as the extinction strain rate for most hydrocarbon fuels. To evaluate their results, the authors used a Rayleigh criterion, which states that acoustic instabilities become greatest when the acoustic pressure and flame's HRR are in phase [35]. The results of their analysis showed that linear responses in the flame's position, HRR, and values of Da were caused by oscillations in the position of the reaction sheet and magnitude of field variables (e.g. pressure, velocity, density) in the transport zone. Near the flame's extinction limit they found that it was the oscillations in the reaction sheet which were dominant and produced the most dramatic effect. When closer to equilibrium conditions though, they found that oscillations in the field variables that were dominant, although these produced much less dramatic effects [21].

Wang *et al* studied the non-linear effects of acoustics on the puffing frequency and flame height of a buoyant diffusion methane flame. In their study, they used a bluff-body stabilized burner and introduced acoustics of varying frequency and

amplitude into the fuel flow prior to its exit. The frequencies tested ranged from 6-100 Hz, and the acoustic pressures tested ranged from 1.1-90 Pa. A high speed camera was used to measure the flame's height, from which the puffing frequency could be determined. Their results showed that while acoustics produced effects over the entire frequency range tested, the effects were particularly pronounced in the range of 6-20 Hz. Within this range, they found that the puffing frequency of the flame was half the excitation frequency, which they attributed to sequential bulges in the flame's natural puffing cycle being merged into one. At higher frequencies, they found there was a "doubling" effect on the flame's puffing, which they attributed to breakdowns in the flow structures occurring at a faster rate. [30].

Complimenting the work of Wang *et al* was a study by Chen *et al*, who also examined the effects of acoustics on a buoyant diffusion flame. In their study, they placed a propane burner at the approximate midpoint of a 1.1 m long glass tube with a square cross section and speaker mounted at the bottom. Acoustic waves at frequencies of 90, 150, and 200 Hz were then produced and Schlieren imaging was used to study the effects on the flame's flow field. They also noted that the most dramatic effects on the flame's height occurred at the lowest frequency, and that at the highest frequency there was a non-linear response in the flame's flickering frequency [33].

Interspersed throughout this body of work have been several studies that explored acoustic extinction for gaseous-fueled flames[4, 21, 31, 36]. Although Kim and

Williams did identify acoustic extinction criteria in their theoretical work, their results only applied to oscillations of the flame's reaction zone and its effects on flame chemistry [21]. Other authors have examined the phenomenon for flames in the context of a buoyant flow field. For example, Hardalupas and Selbach studied acoustic extinction for a methane flame [31], and Whiteside studied the phenomenon for methane along with several other gaseous fuels [4].

Hardalupas and Selbach used a co-axial swirl stabilized burner with acoustics introduced in the fuel and oxidizer flows below the flame. Using frequencies of 200-920 Hz, they created a flame in a lifted state, from which they determined conditions for reattachment. They found that at certain frequencies the acoustic perturbations could cause a lifted flame to reattach. They attributed this phenomenon to the creation of vortex rings by the waves and the impulses they impressed on the flame as they shed from the flow. They also explored flame extinction at 200 Hz and 350 Hz, and concluded that the mechanism of flame extinction was blow off. While the work of Wang [30] and Chen [33] indicated that the flame's response was more sensitive to acoustic frequency than amplitude, Hardalupas and Selbach came to a different finding. They concluded that it was the acoustic amplitude which has the strongest effect, since that caused the largest movement of air [31].

Whiteside looked specifically at acoustic flame extinction from a burner using methane, ethanol, hexane, and heptane. In contrast to the work of other authors, Whiteside used acoustics that propagated in a transverse direction to the flame. Frequencies ranging from 35-150 Hz were employed, with acoustic pressures ranging

from 0.2-112 Pa. Whiteside's data showed that as the molar mass of the fuel increased, so too did the acoustic pressure required to cause flame extinction. The extinction pressure though for each fuel was independent of the burner's cross-sectional area. The author concluded that there was a minimum acoustic velocity required to cause extinction for each fuel, and that acoustic extinction could be achieved at any frequency provided the acoustic pressure was high enough to achieve that velocity. Whiteside also concluded that blow off alone did not fully explain the extinction mechanism, since the flame could exist in a lifted state for short periods [4].

### **1.3 Scope of Work**

While other authors have explored acoustic extinction criterion for fuel droplet flames [23] and gaseous flames from a burner [4, 31], there has been no work in this context on flames fueled by a stagnant liquid. The flame from a stagnant liquid though represents the most realistic scenario from a fire-protection perspective. In addition, the governing phenomena of the observed extinctions, especially in the case of Whiteside's work, are not fully understood. An investigation into acoustically-driven flame extinction, especially for flames with liquid fuel sources, is therefore ripe for inquiry.

An apparatus was constructed that produced collimated acoustic waves which could interact with a laminar diffusion line-flame that approximated a flame sheet.

The flame was fed by a liquid fuel source, and to limit the transient effects of heat feedback, the fuel was supplied through a wick. The fuels chosen for testing were n-pentane, n-hexane, n-heptane, n-octane, and JP-8. By modulating the frequency and amplitude of the acoustics produced, the conditions required to cause acoustic extinction of flames from each fuel could be determined. The work was supplemented with studies of the alkanes' burning rate and flame height unperturbed, and the study of a hexane flame's burning rate experiencing acoustic perturbation.

# Chapter 2

## Testing Apparatus

### 2.1 Overview

A testing apparatus was designed that facilitated the study of a laminar flame experiencing acoustic perturbation. The primary objective of the design was to create a line-flame that approximated a flame sheet, and which could interact with a planar acoustic wave front simultaneously across the flame's entire surface. Other key design features included minimizing the transient effects of heat feedback into the fuel and errant air flows around the flame.

The apparatus involved three main components: an acoustic source and collimator, burner, and testing enclosure. The acoustic source and collimator consisted of a sub-woofer mounted inside a  $2.54 \times 10^{-1}$  m diameter, 3.05 m long PVC tube. In some experiments, the sub-woofer was replaced with a fan to study the effects of

a forced flow on the flame. At the opposing end, a line-flame was created from a fuel laden wick mounted inside the burner. The burner was housed in a screened enclosure which was large enough to accommodate both it and the data acquisition equipment (DAQ). Depending on the experiment being conducted, the burner was either supported on a fixed stand or a mass balance. A schematic of the testing apparatus is shown in Fig. (2.1). Detailed descriptions of the acoustic source, burner, and testing enclosure are provided in Sec.'s (2.2), (2.3), and (2.4) respectively.

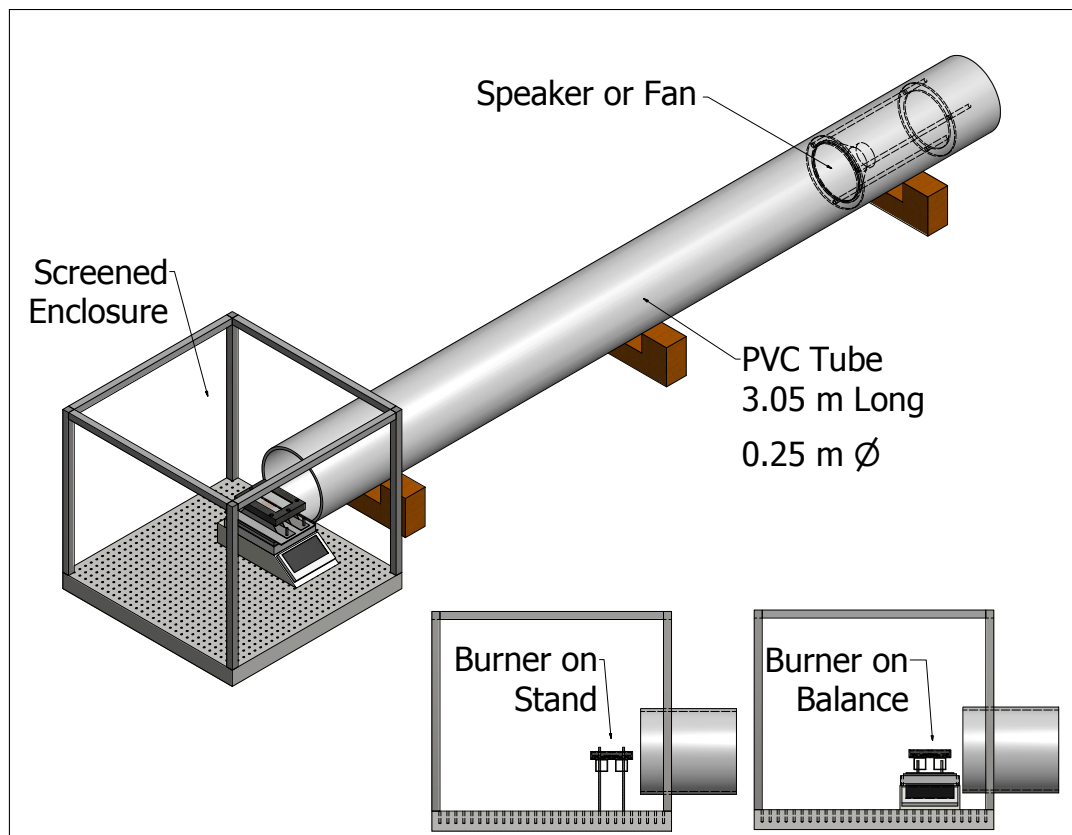


Figure 2.1: Testing Apparatus Overview

## **2.2 Acoustic Source**

The acoustics used for testing were generated using a  $2.03 \times 10^{-1}$  m diameter sub-woofer which was mounted on a sabot and placed inside the tube. The signal sent to the sub-woofer originated at a signal generator, which was used to modulate both the frequency and amplitude of the signal. The signal was then sent to an amplifier, which increased the power of the signal to sub-woofer's operational range.

### **2.2.1 Signal generation**

Signals for the sub-woofer were generated using the Agilent 3220A, 20 MHz signal generator; its data sheet is included in Appendix (B.1). The signals used for testing ranged in frequency from 30-50 Hz, and voltages from 50-1500 mV<sub>rms</sub>. Upon generation, the signals were sent along 16-gauge stranded copper wire to an AE Techron 8102 Amplifier, where the voltage was increased by a factor of 20; the amplifier's data sheet is included in Appendix (B.3). The electrical power developed by the amplifier ranged between  $2.50 \times 10^{-1}$  W and  $2.25 \times 10^2$  W, which was also delivered along 16-gauge stranded copper wire to the sub-woofer.

### **2.2.2 Sub-Woofer**

The sub-woofer used was an Infinity Reference 860w; its data sheet is included in Appendix (B.2). The outside diameter of the sub-woofer measured  $2.03 \times 10^{-1}$

m, which was  $5.1 \times 10^{-2}$  m less than the inside diameter of the tube. A sabot was, therefore, constructed which held the sub-woofer in place at the tube's center.

The sabot was made from two annular rings cut from  $3.18 \times 10^{-3}$  m thick aluminum plating. The rings had an outside diameter of  $2.54 \times 10^{-1}$  m and an inside diameter  $2.03 \times 10^{-1}$  m. The rings were spaced  $4.19 \times 10^{-1}$  m apart using three  $1.27 \times 10^{-2}$  m diameter threaded rods. A schematic and picture of the sabot with the speaker are shown in Fig.'s (2.2a) and (2.2b) respectively.

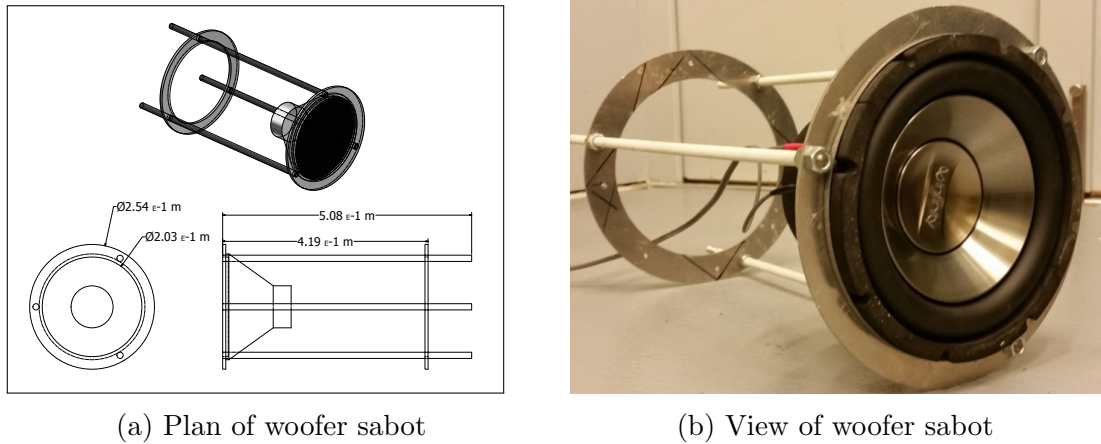


Figure 2.2: Plan and view of woofer sabot

The sabot was placed inside the tube with the sub-woofer's face located  $6.1 \times 10^{-1}$  m from the tube opening, as shown in Fig. (2.3). Rubber door stops (not shown) were wedged between the protruding sections of the threaded rods and the sidewall of the tube to help dampen the sabot's vibrations. A foam disk measuring  $7.62 \times 10^{-2}$  m thick (not shown) was used to plug the back of the tube.

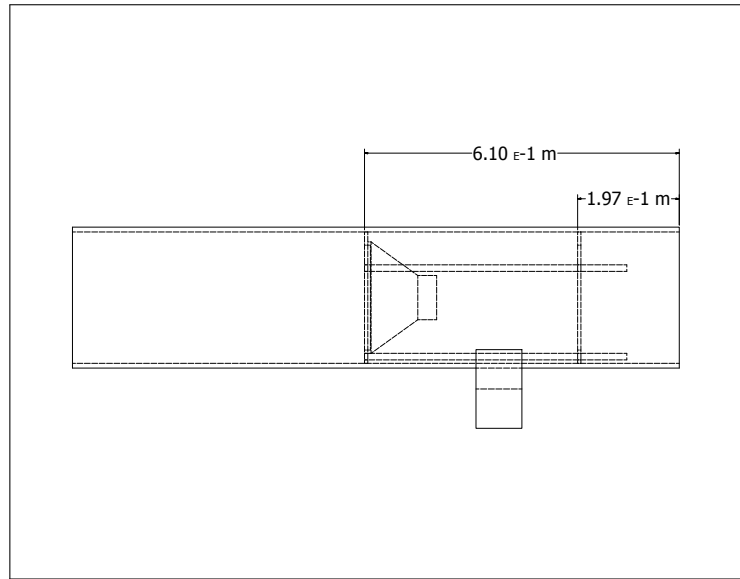


Figure 2.3: Speaker Sabot Placement

## 2.3 Burner

The burner was constructed from  $3.18 \times 10^{-3}$  m thick steel sheet metal, cut by high pressure water jets, and welded at the component interfaces. The burner consisted of three main components: support rails, a base plate, and a lid. Sandwiched between the lid and the base plate was insulation, the wick, and two sheets of borosilicate glass spaced  $5 \times 10^{-3}$  m apart. A schematic of the burner's overall design is shown in Fig. (2.4).

For consistency, a new wick holding 3.5 mL of fuel was placed in the burner for every trial. The material used for both the wick and surrounding insulation was Type PM Kaowool<sup>®</sup>; its product data sheet is included in Appendix (B.4). An annotated visualization of the wick's preparation process is presented in Fig. (2.5).

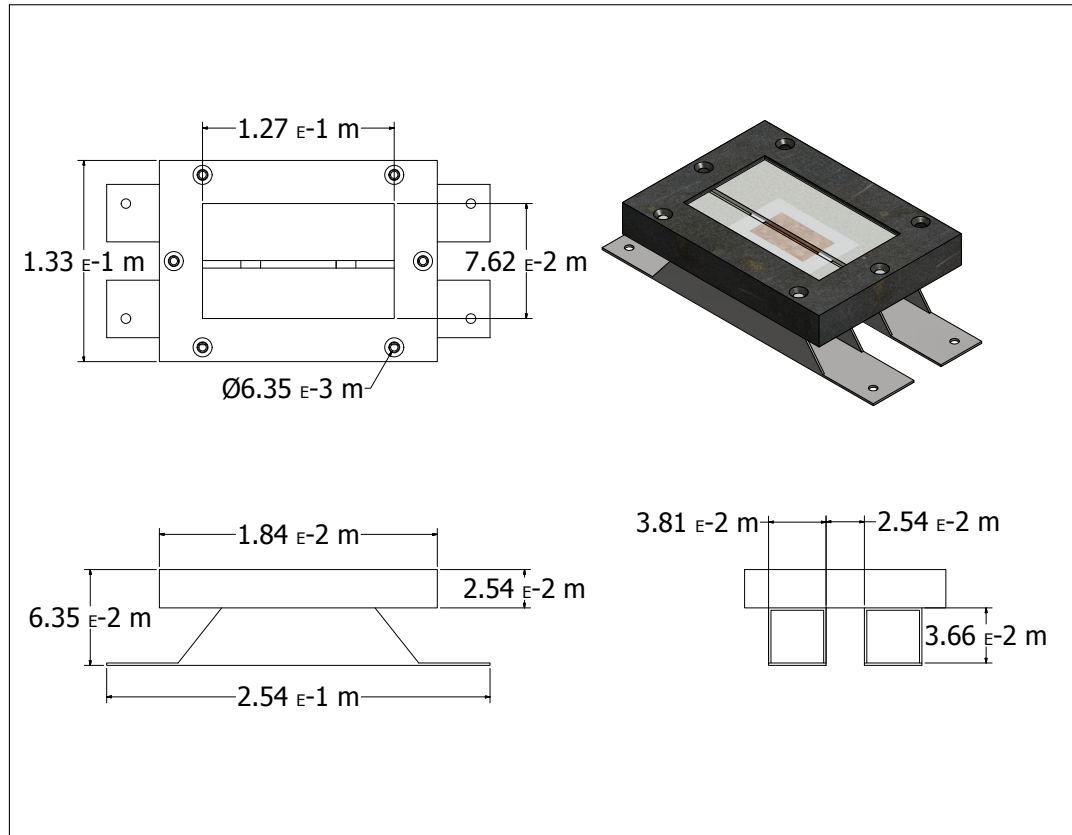


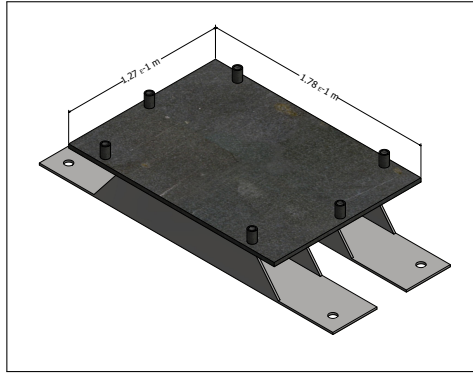
Figure 2.4: Burner Plan

Once ignited and allowed to burn undisturbed, the burner produced a nearly two dimensional laminar line-flame through the gap in the glass panes. The height of flame ranged from  $2 \times 10^{-2}$  m to  $1.00 \times 10^{-1}$  m, depending on the fuel type and elapsed time in the flame's evolution. A hexane flame at approximately 20 sec after ignition is shown from the the coronal and sagittal planes in Fig.'s (2.6a) and (2.6b) respectively.

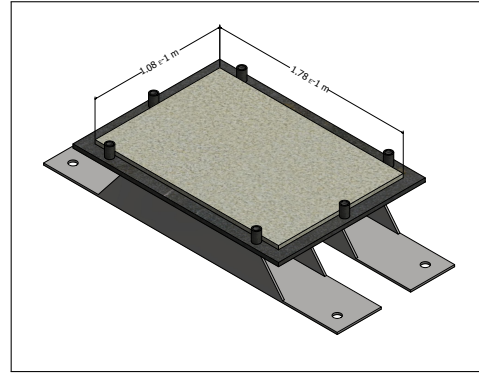
## 2.4 Testing Enclosure

The testing enclosure created a space where an open flame could burn safely while simultaneously reducing the effects of errant air flows on the flame. The enclosure was built on a steel bread board measuring  $7.62 \times 10^{-1} \text{ m} \times 7.62 \times 10^{-1} \text{ m} \times 6.35 \times 10^{-2} \text{ m}$ . The surface of the board had a grid of screw holes spaced on  $2.54 \times 10^{-2} \text{ m}$  squares that could accommodate  $1/4 - 20$  threading. Erected on the corners of the board were vertical metal supports measuring  $6.35 \times 10^{-1} \text{ m}$  high. The tops of the vertical supports were connected with horizontal supports, creating a rectangular enclosure measuring  $7.62 \times 10^{-1} \text{ m} \times 7.62 \times 10^{-1} \text{ m} \times 6.35 \times 10^{-1} \text{ m}$ . A fine steel mesh screen with  $1.00 \times 10^{-6} \text{ m}^2$  holes was then placed over the faces of the enclosure, with only an opening for the tube left in the coverage. A schematic of the enclosure is shown in Fig. (2.7), and pictures taken of the enclosure during routine cleaning are shown in Fig.'s (2.8a) and (2.8b).

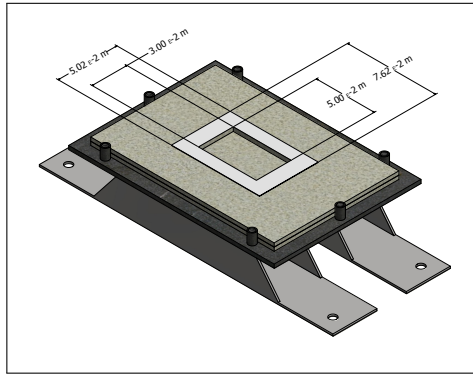
The burner was placed within the enclosure so that the flame's base would be on the center-line axis of the tube. As shown in Fig. (2.7), the top of the flame holder was coplanar with the transverse plane of the tube, and the holder was positioned so that the flame was  $9 \times 10^{-2} \text{ m}$  away from the tube opening. A picture of the burner in testing position is shown in Fig. (2.9a). The excess space in the testing enclosure behind the burner was used to house the DAQ, some of which is shown during calibration in Fig. (2.9b).



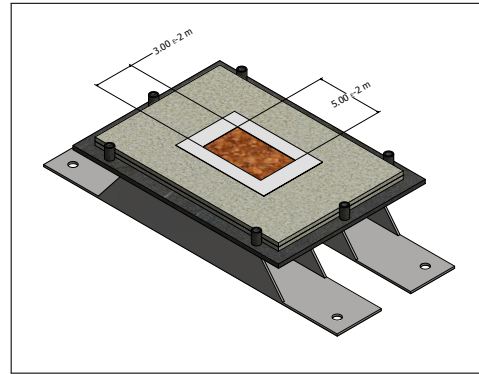
(a) All components from the previous test were removed, and the burner was allowed to cool to room temperature.



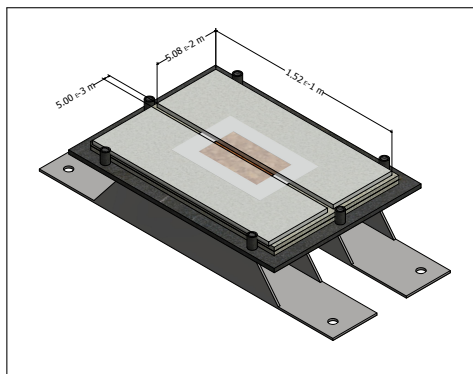
(b) A piece of backing insulation was placed on the base plate.



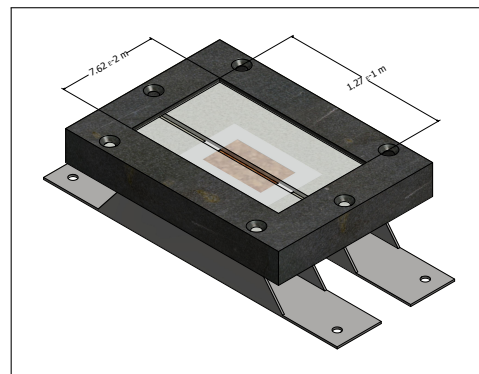
(c) A second piece of insulation containing a foil lined center cut-out was placed on top of the first.



(d) The wick was placed in the foil lined cutout, and 3.5 mL of fuel was poured along its center-line axis.

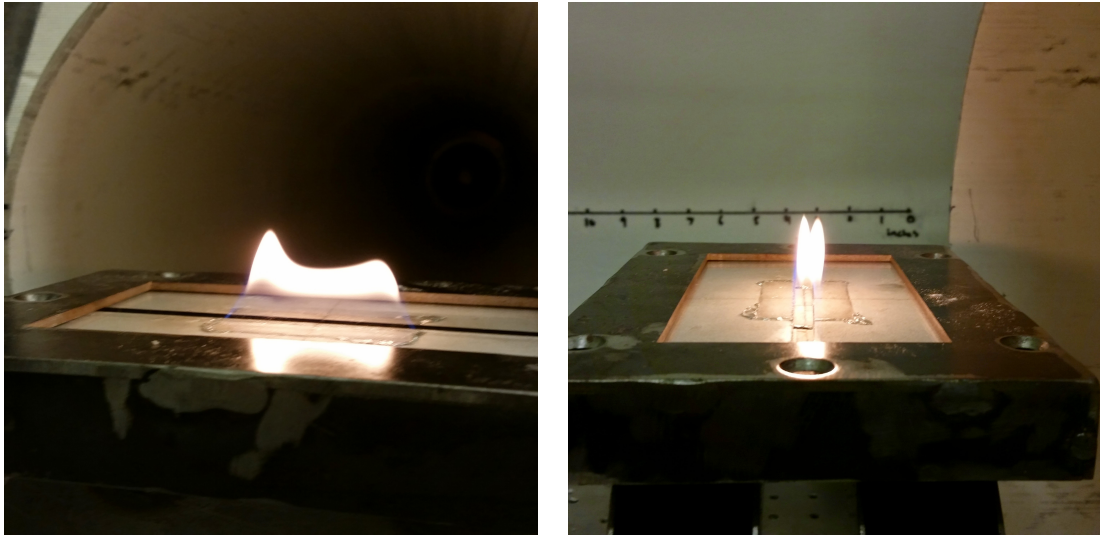


(e) Two pieces of  $3.18 \times 10^{-3}$  m thick borosilicate glass were placed over the wick, leaving a  $5 \times 10^{-3}$  m gap for fuel to escape.



(f) Finally, the lid was placed over the glass panels and secured to the base plate with screws (not shown).

Figure 2.5: Wick preparation and burner assembly sequence



(a) View of the flame sheet in the coronal plane (b) View of the flame sheet in the sagittal plane

Figure 2.6: Views of the flame sheet in the coronal and sagittal planes.

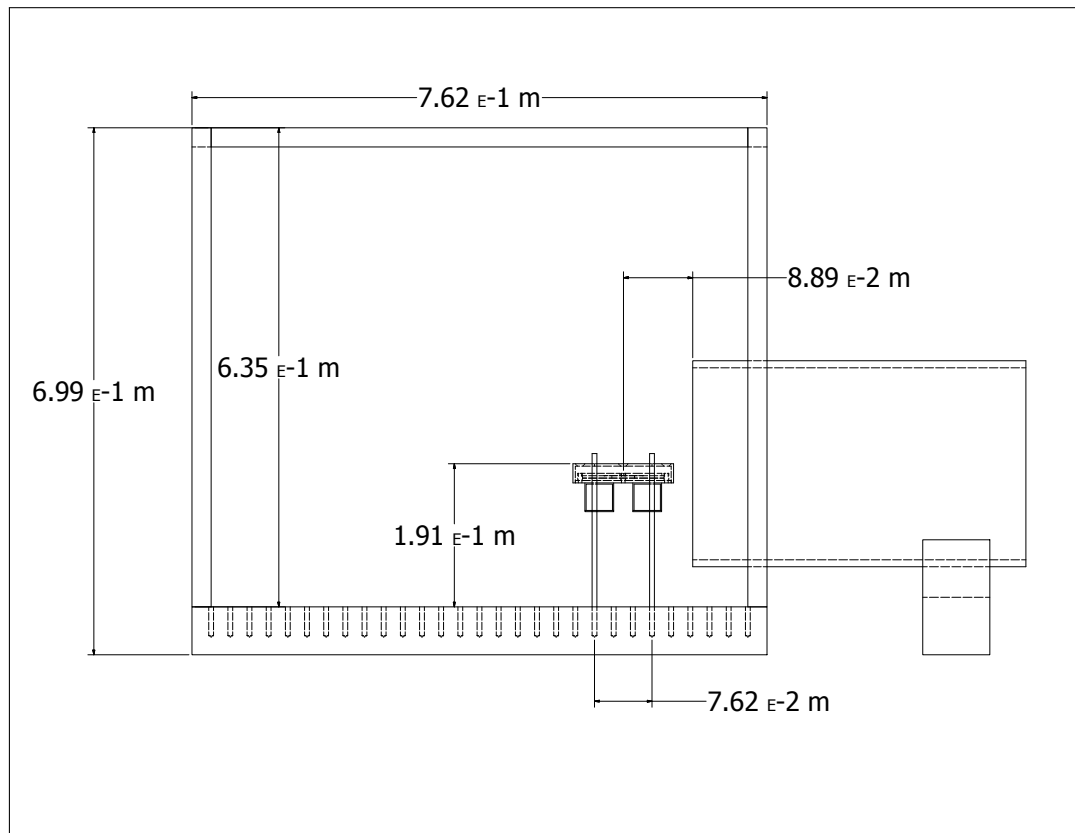
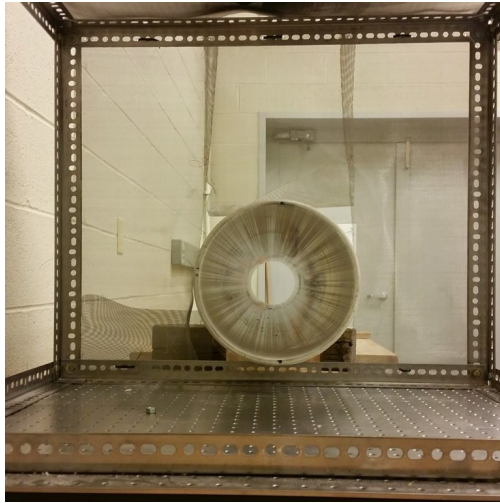
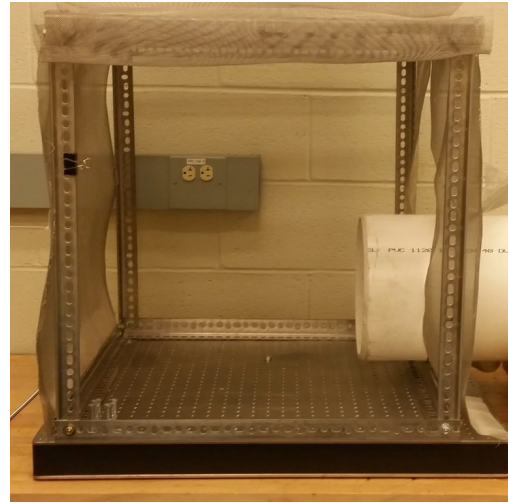


Figure 2.7: Plan of Testing Enclosure



(a) View of testing enclosure in the coronal plane

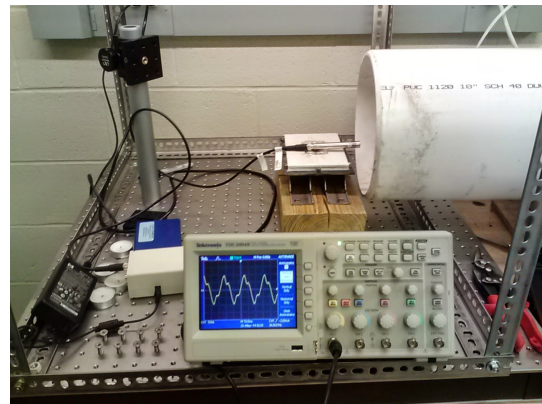


(b) View of testing enclosure in the sagittal plane

Figure 2.8: Views of testing enclosure



(a) Flame holder in position



(b) DAQ during calibration

Figure 2.9: Views of the flame holder and DAQ equipment in the testing enclosure

# Chapter 3

## Data Acquisition

### 3.1 Overview

Data acquisition was limited to methods that did not interact directly with the flame. Of particular interest were the acoustic conditions the flame experienced at the point of extinction. These conditions included the acoustic pressure and the speed of air movement around the flame. Other metrics of interest included the flame's burning rate and its movement during an acoustic cycle. The equipment used to obtain this data is described in the following sections.

## **3.2 Acoustic Pressure**

Measurements of acoustic pressure were made using a  $1.27 \times 10^{-2}$  m diameter integrated constant current power (ICCP) microphone, manufactured by the BSWA Technology Co., Model # MPA 231. The gauge was connected by BNC cable to a signal conditioner, which was then connected to a Tektronix Digital Oscilloscope, Model # TDS 2004B. Using the oscilloscope, an *rms* voltage from the pressure gauge was obtained, which was then converted into an *rms* pressure reading. The conversion from voltage to pressure is described in Sec. (3.2.1). Product data sheets for the pressure gauge, signal conditioner, and oscilloscope are included in Appendix (B.5), (B.6), and (B.8) respectively.

### **3.2.1 Microphone Calibration**

Accompanying the pressure gauge was the BSWA Calibrator, Model # CA111, and its data sheet is included in Appendix (B.7). A calibration of the pressure gauge was performed prior to every testing session, and each testing session generally lasted 4 to 6 hours. The calibration unit produced a 1000 Hz tone at 94 dB and 114 dB. Decibel reading are calculated from acoustic pressure as:

$$\text{dB} = 20 \log \left( \frac{P_{rms}}{P_{ref}} \right) \quad (3.1)$$

where  $P_{rms}$  is the rms pressure of a complete acoustic cycle, and the reference pressure ( $P_{ref}$ ) is commonly taken as  $20 \mu\text{ Pa}$  [37]. Rearranging Eq. (3.1) yields:

$$P_{rms} = P_{ref} \cdot 10^{\text{dB}/20} \quad (3.2)$$

Using Eq. (3.2), it was found that 94 dB corresponds to  $1 \text{ Pa}_{rms}$ , and 114 dB corresponded to  $10 \text{ Pa}_{rms}$ . To convert from a voltage reading to a pressure reading, a calibration constant ( $k$ ) was desired such that:

$$P_{rms} = kV_{rms} \quad (3.3)$$

Using the form presented in Eq. (3.3), a specific value of  $k$  for each calibration pressure was calculated as:

$$1 \text{ Pa}_{rms} = k_1 V_{1,rms} \quad (3.4)$$

$$10 \text{ Pa}_{rms} = k_2 V_{2,rms} \quad (3.5)$$

An average calibration constant was then calculated as:

$$\bar{k} = \frac{1}{2} \left( \frac{1 \text{ Pa}_{rms}}{V_{1,rms}} + \frac{10 \text{ Pa}_{rms}}{V_{2,rms}} \right) \quad (3.6)$$

Using the results for  $\bar{k}$  from Eq. (3.6), an *rms* pressure was calculated from the oscilloscope voltage using Eq. (3.3). The average value ( $\mu$ ) and standard deviation ( $\sigma$ ) of all calibration constants found during testing were:

$$\mu_{\bar{k}} = 0.0218 \frac{\text{Pa}}{\text{mV}}, \quad \sigma_{\bar{k}} = 0.0004 \frac{\text{Pa}}{\text{mV}}$$

### **3.3 Anemometry**

Anemometry readings were made using an Extec Hot Wire Anemometer, Model # 407123. The measurements were made in units of ft/min, which provided the highest resolution, and then converted to m/s. The product data sheet for the anemometer is included in Appendix (B.9).

### **3.4 High Speed Video**

A Phantom high speed camera, Model # V461, was used to capture high speed videography. Videos were shot at either 400 or 1000 frames per second (fps) and at a resolution of  $640 \times 480$ . The product data sheet for the camera is included in Appendix (B.10).

### 3.5 Mass Readings

Time-resolved mass readings were made using a Mettler Toledo Precision Balance, Model # MS4002S. A RS232 - USB cable was used to connect the balance to a computer, and a MATLAB script was written which read the data and stored it in a text file. In order to use the balance, the burner's support rods, shown in Fig. (2.7), were removed. A separate stand was fabricated which provided the burner with stability while on the balance; a picture of the stand is shown in Fig. (3.1). When the balance was in use, it was situated in the enclosure so that the burner still occupied the same position described in Sec. (2.4). The product data sheet for the balance is included in Appendix (B.11).

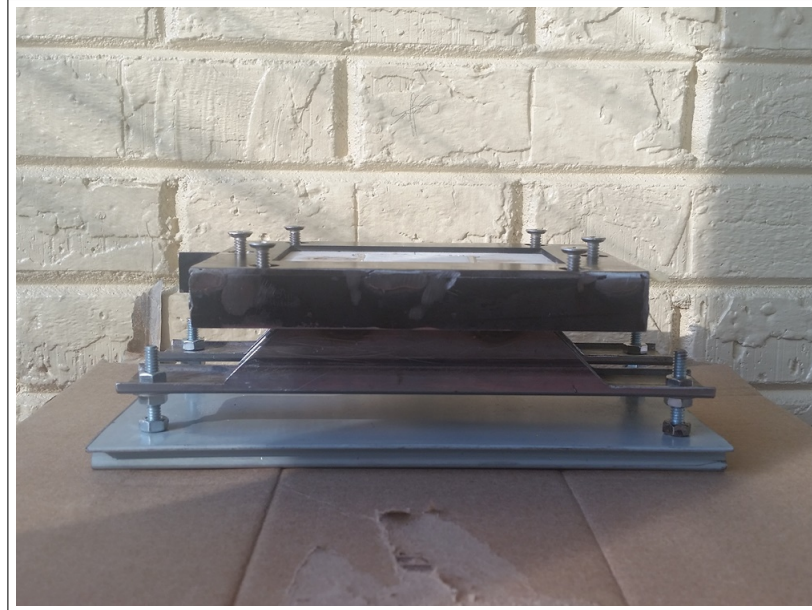


Figure 3.1: Burner Balance Stand

# Chapter 4

## System Characterization

### 4.1 Overview

A detailed study of the testing apparatus was conducted prior to experimentation with a flame. The specific objectives of the study were to understand the system's harmonics, the acoustic pressures generated, and nature of the acoustically induced air movements.

### 4.2 System Harmonics

The first study conducted was meant to determine if the system showed resonance at frequencies consistent with theory. The study began by calculating the resonant frequencies for the 1<sup>st</sup>, 2<sup>nd</sup>, and 3<sup>rd</sup> harmonic modes of the tube. While the

tube's length was 3.05 m, it was treated as being 2.44 m since the speaker was mounted 0.61 m from the entrance. Pressure measurements were then taken at regular intervals down the length of the tube at the calculated resonant frequencies, and at frequencies within  $\pm 10$  Hz of where resonance was expected. Using the profiles generated, the approximate true frequencies of resonance were identified and compared with those of theory. The calculated frequencies, measured frequencies, and comparison of the results are presented in Sec.'s (4.2.1), (4.2.1), and (4.2.3) respectively.

#### **4.2.1 Predicted Resonant Frequencies**

The speed of sound ( $c_s$ ) is related to the wavelength ( $\lambda$ ) and frequency ( $\omega$ ) by the relation:

$$c_s = \lambda\omega \quad (4.1)$$

For a closed-open tube system, the length of resonance ( $L_{R_n}$ ) for the  $n^{\text{th}}$  harmonic is related to  $\lambda$  by the correlation:

$$L_{R_n} = \frac{(2n - 1)\lambda}{4} \quad (4.2)$$

where  $L_{R_n}$  is equal to the the tube's actual length ( $L_o$ ) plus a correction factor ( $e$ ) [37]. The frequency of resonance can then be related to the tube's length by:

$$L_o + e = \frac{(2n - 1)\lambda}{4} \quad (4.3)$$

From experimentation, it is known that  $e = 0.3D$ , where  $D$  is the tube diameter [37]. Substituting Eq. (4.1) into Eq. (4.3) and rearranging, the frequencies of resonance for the  $n^{\text{th}}$  harmonic can be calculated as:

$$\omega_{R_n} = \frac{(2n - 1)c_s}{4(L_o + 0.3D)} \quad (4.4)$$

Since the speaker was mounted 0.61 m inside the 3.05 m long tube, the system was treated as being 2.44 m long. Using  $c_s = 343$  m/s,  $L_o = 2.44$  m and  $D = 0.254$  m in Eq. (4.4), the frequencies for the 1<sup>st</sup>, 2<sup>nd</sup>, and 3<sup>rd</sup> harmonics were calculated and are presented in Tab. (4.1).

Table 4.1: Calculated resonant frequencies of the tube for the 1<sup>st</sup>, 2<sup>nd</sup>, and 3<sup>rd</sup> harmonics.

Mode $n$	Calculated $\omega_{R_n}$ (Hz)
1	34.1
2	102.3
3	170.5

## 4.2.2 Observed Resonant Frequencies

To determine the approximate frequencies where resonance truly occurred, a series of frequencies was tested for each mode within a window centered on  $\omega_{R_n}$ . The size of the window was  $\pm 10$  Hz and divided into 2.5 Hz increments. For each frequency

tested, center-line pressure measurements were made at regular intervals down the length of the tube. Profiles were then generated from these measurements by using a spline fit in Matlab. For each frequency tested, measurements were made at speaker powers of 25 W and 100 W. Representative profiles from the 1<sup>st</sup>, 2<sup>nd</sup>, and 3<sup>rd</sup> harmonics are shown in Fig.'s (4.1), (4.2), and (4.3) respectively.

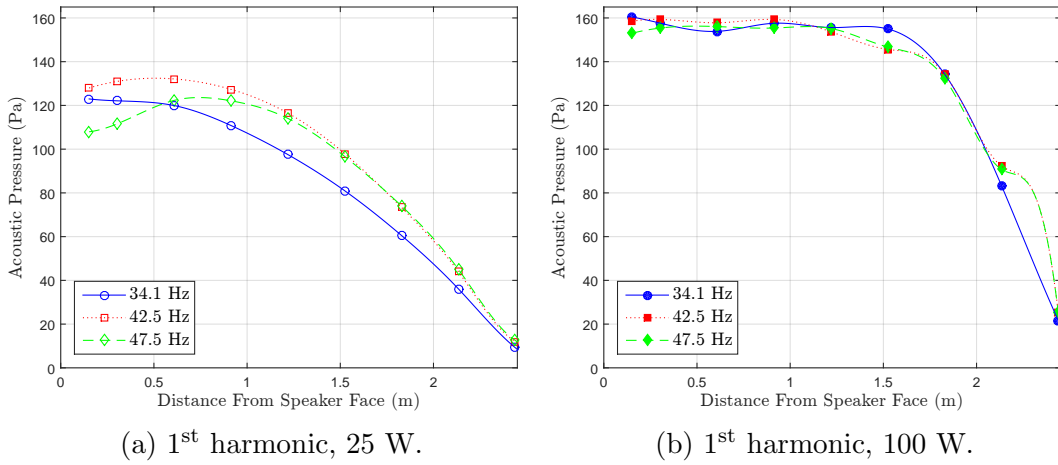


Figure 4.1: Representative pressure profiles from the 1<sup>st</sup> harmonic on the interior of the tube. The profiles in Fig. (4.1a) were produced at a speaker power of 25 W, and the profiles in Fig. (4.1b) at 100 W.

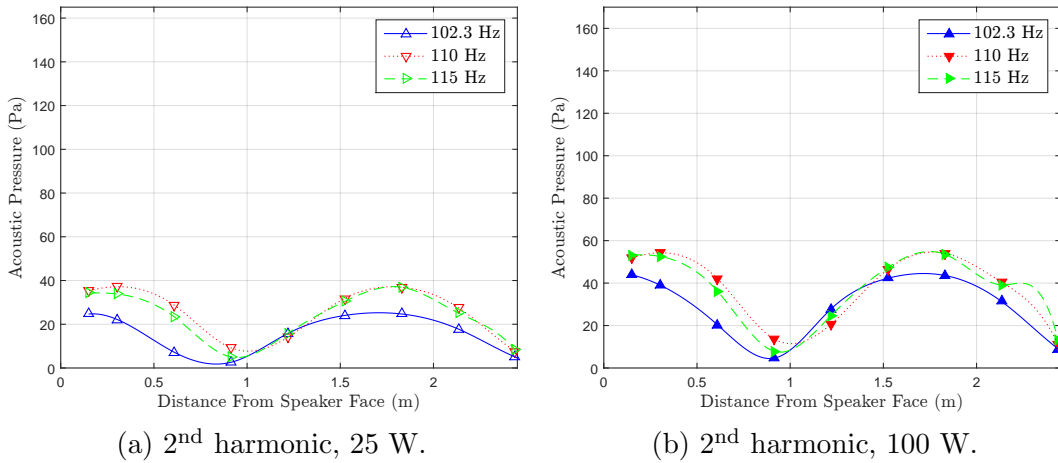


Figure 4.2: Representative pressure profiles from the 2<sup>nd</sup> harmonic on the interior of the tube. The profiles in Fig. (4.2a) were produced at a speaker power of 25 W, and the profiles in Fig. (4.2b) at 100 W.

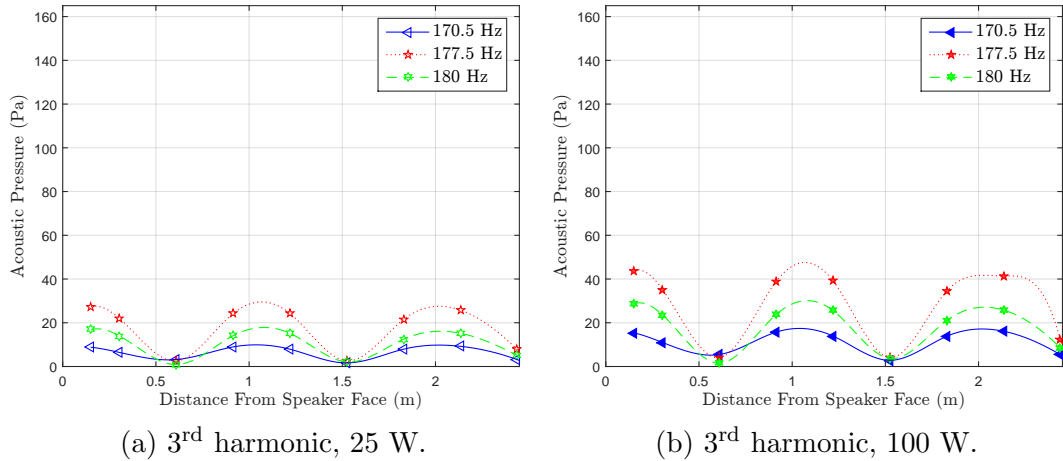


Figure 4.3: Representative pressure profiles from the 3<sup>rd</sup> harmonic on the interior of the tube. The profiles in Fig. (4.3a) were produced at a speaker power of 25 W, and the profiles in Fig. (4.3b) at 100 W.

The approximate frequencies of true resonance were identified by visually inspecting the family of profiles for each harmonic, and then identifying the profile that had peak amplitudes. Results for the 2<sup>nd</sup> and 3<sup>rd</sup> harmonic were confirmed by noting that peak amplitudes occurred at the same frequency for both 25 W and 100 W. Intense vibrations of the testing apparatus occurred though during the 1<sup>st</sup> harmonic tests at 100 W. As seen in Fig. (4.1b), these vibrations made accurate pressure measurements difficult and obscured the results. The approximate resonant frequency for the first harmonic was, therefore, estimated from the 25 W profile alone. The predicted and observed resonant frequencies for the first three modes are presented in Tab. (4.2).

Table 4.2: Predicted and observed resonant frequencies of the tube for the 1<sup>st</sup>, 2<sup>nd</sup>, and 3<sup>rd</sup> harmonics.

Mode $n$	Predicted $\omega_{R_n}$ (Hz)	Observed $\omega_{R_n}$ (Hz)
1	34.1	42.5
2	102.3	97.5
3	170.5	177.5

### 4.2.3 Comparison of Predicted and Observed Resonance

Rearranging Eq. (4.4), the length of a tube that resonates on the  $n^{\text{th}}$  harmonic for a given frequency can be calculated as:

$$L_o = \frac{(2n - 1)c_s}{4\omega} - 0.3D \quad (4.5)$$

Using the values from Tab. (4.2) in Eq. (4.5), the observed frequencies of resonance for the 1<sup>st</sup>, 2<sup>nd</sup>, and 3<sup>rd</sup> harmonics were found to correspond with tube lengths of 1.94 m, 2.56 m, and 2.33 m respectively. On average then, the tube behaved acoustically as having a length of 2.28 m. When compared to the actual effective length of 2.44 m, it can be seen that the two are in relatively close agreement. It was, therefore, concluded that the tube was behaving acoustically in a manner consistent with theory.

## 4.3 Pressure Scaling

The next study of the system was designed to characterize the acoustic pressures outside the tube in the region that the flame would inhabit. For every frequency tested during the procedure described in Sec. (4.2), pressure measurements were also taken at varying distances from the tube's end along the projected center-line axis of the tube. Representative profiles from the 1<sup>st</sup>, 2<sup>nd</sup>, and 3<sup>rd</sup> harmonics are shown in Fig.'s (4.4), (4.5) and (4.6) respectively.

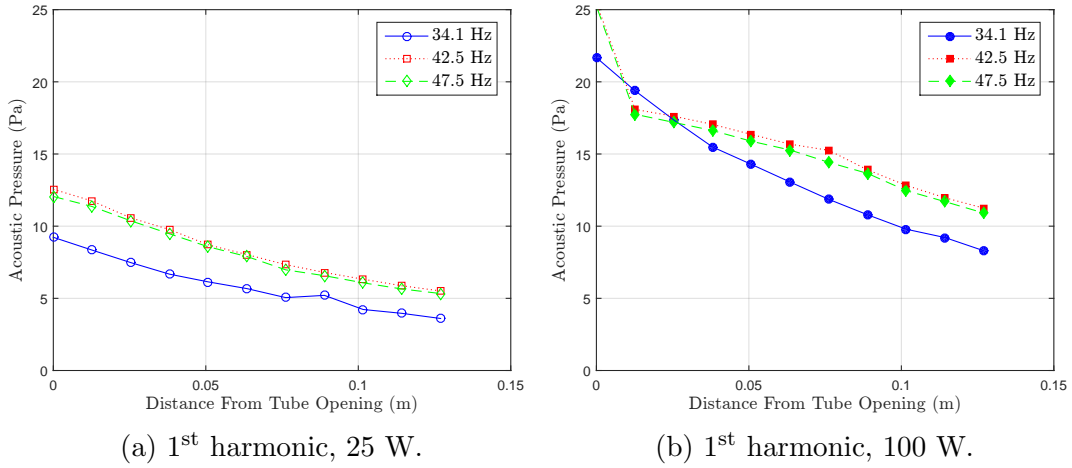


Figure 4.4: Representative pressure profiles from the 1<sup>st</sup> harmonic on the exterior of the tube. The profiles in Fig. (4.4a) were produced at a speaker power of 25 W, and the profiles in Fig. (4.4b) at 100 W.

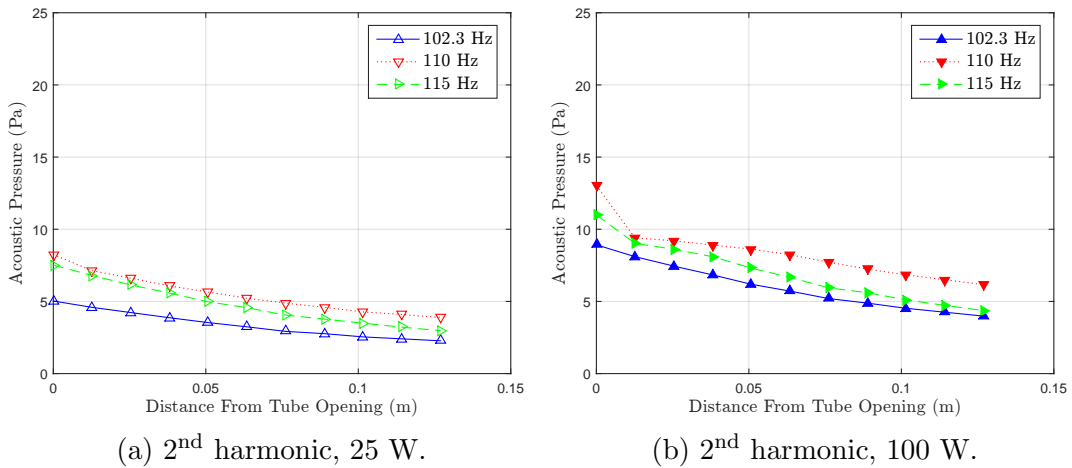


Figure 4.5: Representative pressure profiles from the 2<sup>nd</sup> harmonic on the exterior of the tube. The profiles in Fig. (4.2a) were produced at a speaker power of 25 W, and the profiles in Fig. (4.2b) at 100 W.

The pressure measurements from each profile were then scaled by the pressure at the tube opening. It was found that for each frequency tested, the scaled pressures at 25 W and 100 W showed pointwise convergence. In other words, for each frequency there was a proportional decay in the acoustic pressure as the distance increased from the tube opening. When examined in aggregate, the proportional decay profiles for all frequencies tested showed an overall linear trend.

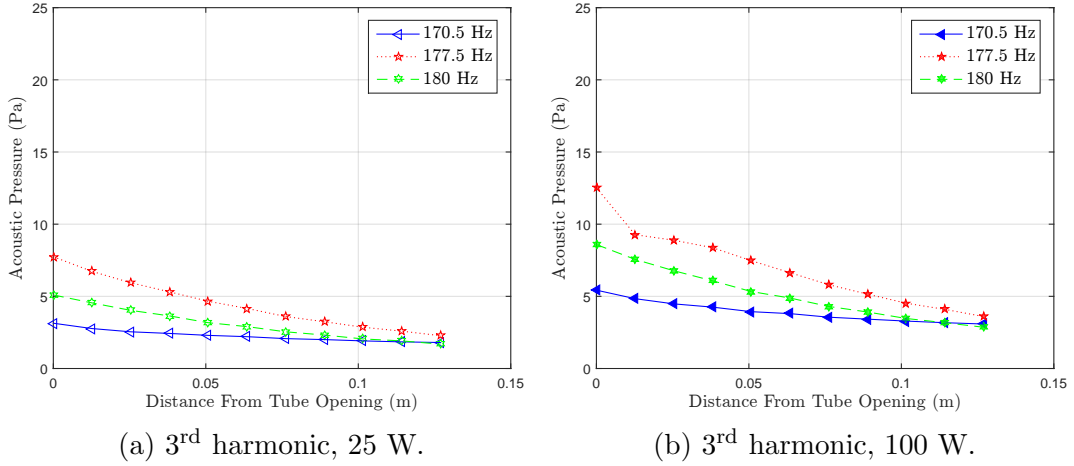


Figure 4.6: Representative pressure profiles from the 3<sup>rd</sup> harmonic on the exterior of the tube. The profiles in Fig. (4.6a) were produced at a speaker power of 25 W, and the profiles in Fig. (4.6b) at 100 W.

Representative samples of the scaled pressure profiles, along with the aggregate line of fit, and coefficient of determination are shown in Fig. (4.7). Using these results, the center-line acoustic pressure at distance  $x$  from the tube opening could be estimated from the acoustic pressure at the tube opening ( $P_o$ ) by the relation:

$$P(x) = P_o (-3.96x + 0.92) \quad (4.6)$$

where the units of  $x$  are m, and the units of it's coefficient are  $m^{-1}$ .

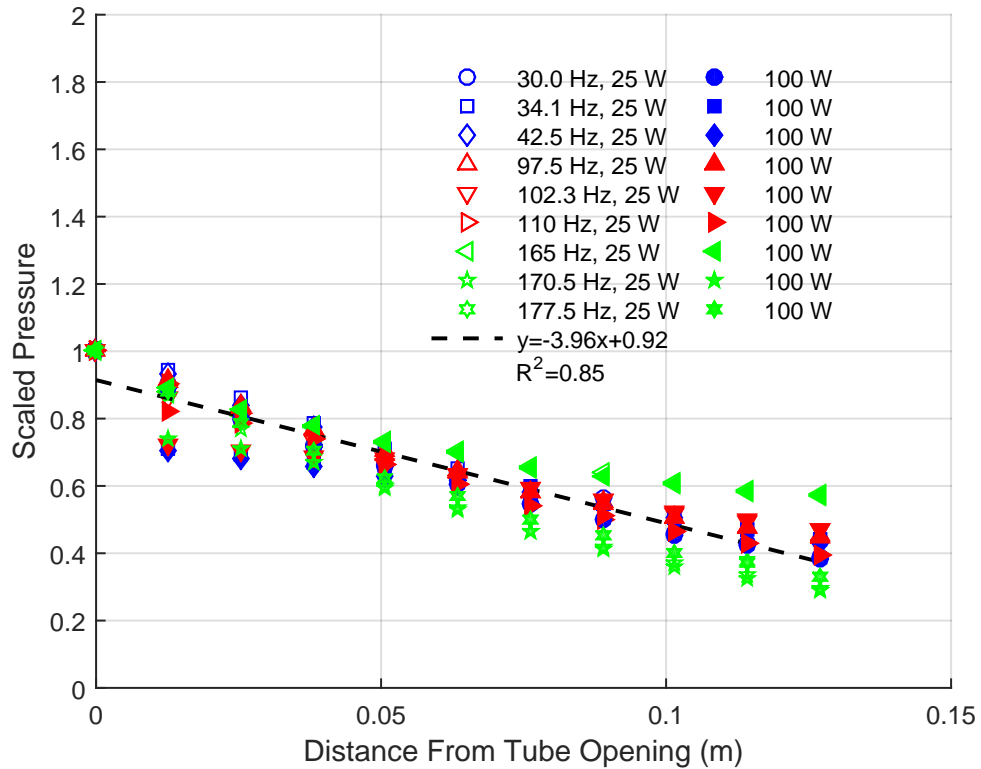


Figure 4.7: Representative samples of scaled exterior acoustic pressures and the aggregate line of fit for all scaled pressures. Each exterior pressure profile measured was scaled by the pressure at the tube opening ( $P_o$ ) for that particular frequency and speaker power. All scaled profiles showed pointwise convergence for each frequency tested. When examined in aggregate, the decay profiles showed an overall linear trend, and the line of fit was calculated from the aggregate data set.

## **4.4 Acoustic Pressure Profiles**

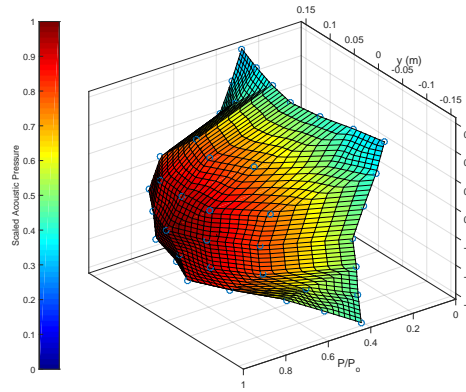
The next study was designed to determine how the burner's presence would affect the sound waves emanating from the tube. To investigate this, a series of acoustic pressure profiles were made with and without the burner in place. The results were then compared to quantify the aggregate effect of the burner's presence.

### **4.4.1 Profiles Without Burner**

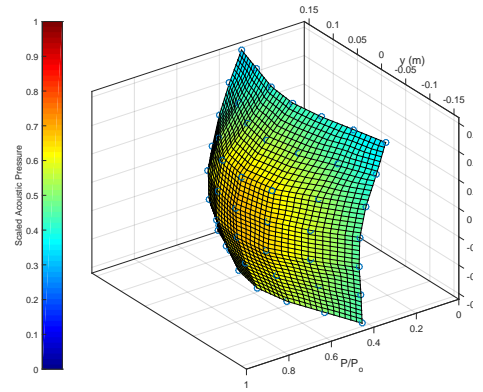
The profiles without the burner were made by measuring the acoustic pressure in the plane of the tube opening at varying distance from the opening. The acoustics used for testing were generated at 40 Hz and 25 W of power to the speaker. The pressure measurements were taken on a 0.05 m grid and at distances from 0 m to 0.15 m in 0.05 m intervals. The pressures in all profiles were then normalized by the center-line pressure at the tube opening. Finally, Matlab was used to interpolate the pressures at interstitial points, creating normalized pressure profiles. The individual profiles are shown in Fig. (4.8), and a schematic of the profiles in relation to the tube is shown in Fig. (4.9).

### **4.4.2 Profiles with Burner**

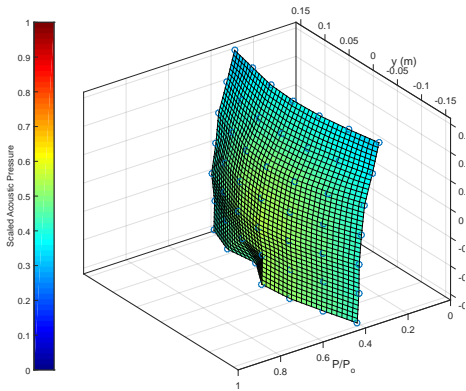
The pressure profiles with the burner in place were generated using the same basic methodology described in Sec. (4.4.1). The presences of the burner, however, made



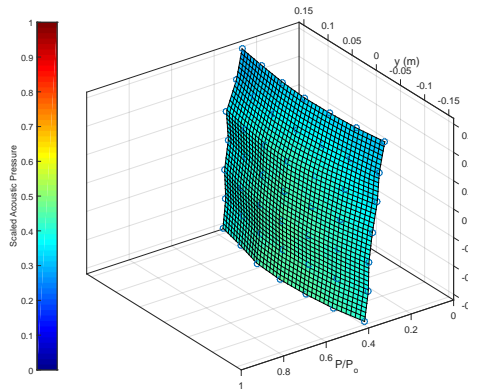
(a)  $x = 0$  m



(b)  $x = 0.05$  m



(c)  $x = 0.10$  m



(d)  $x = 0.15$  m

Figure 4.8: Normalized pressure profiles at varying distances from the tube opening without the burner in place. Pressure measurements were taken at points on a 0.05 m grid, which is indicated by the circles. The pressures were then normalized by the center-line pressure at  $x = 0$ , and a surface was interpolated from the data points. For convenience, the origin of the coordinate system used was placed at the center of the tube opening.

it impossible to obtain measurements at all the points previously evaluated. In addition, the only region of pertinent interest was where the flame would reside. Therefore, profiles were only generated at  $x = 0.05$  m and  $x = 0.10$  m, and in the region above the burner. For reference, a third profile was also generated at the

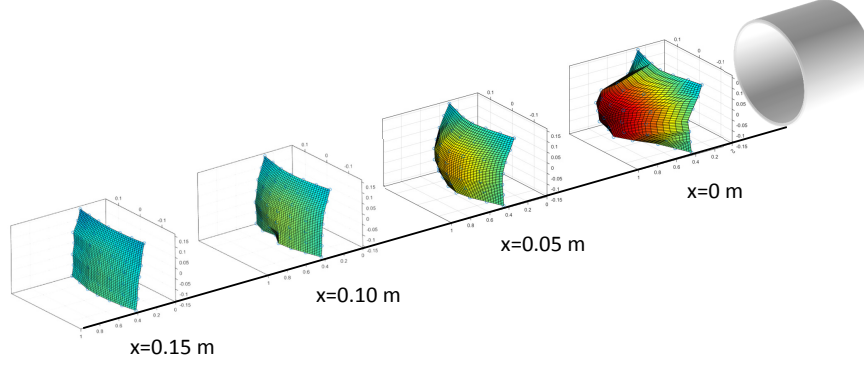


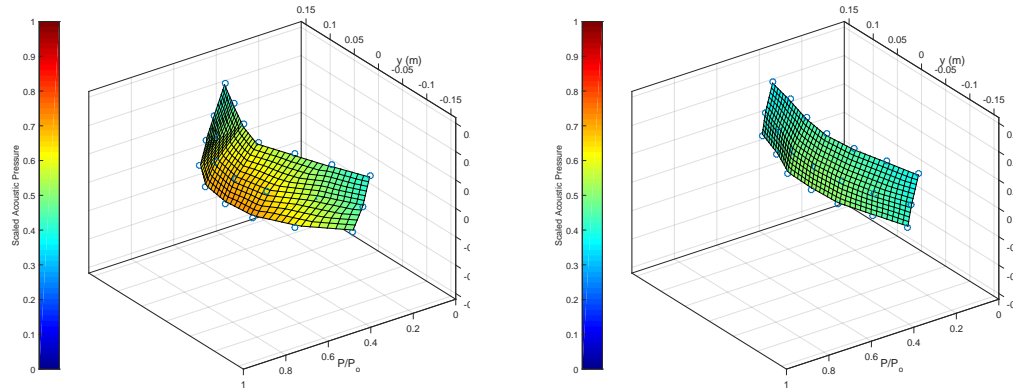
Figure 4.9: Schematic of the normalized pressure profiles presented in Fig. (4.8) in relation to the tube.

actual flame position of  $x = 0.09$  m. The profiles with the burner at  $x = 0.05$  m and  $x = 0.10$  m are shown in Fig.'s (4.10a) and (4.10b) respectively; the pressure profile at the flame position is shown in Fig. (4.10c).

### 4.4.3 Comparison of Profiles

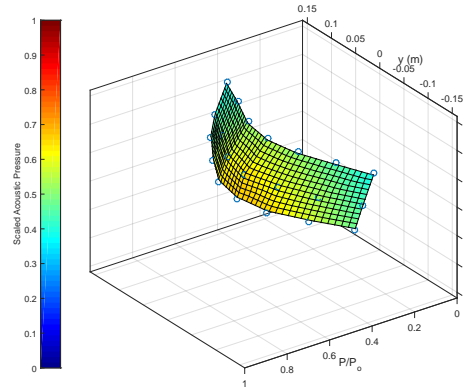
A visual comparison of the pressure profile segments presented in Fig.'s (4.10a) and (4.10b) to the full profiles presented in Fig.'s (4.8b) and (4.8c) indicated that the presence of the burner had a small, but noticeable effect. In order to quantify this effect, a direct comparison between comparable data points was made. For each distance from the tube opening, an average ratio of the scaled pressures with the burner ( $\hat{P}_H$ ) to without the burner ( $\hat{P}_O$ ) was calculated as:

$$\mu_{\hat{P}_H/\hat{P}_O} = \frac{1}{n_i n_j} \sum_{j=1}^{n_j} \sum_{i=1}^{n_i} \frac{P_{H_{ij}}}{P_{O_{ij}}} \quad (4.7)$$



(a)  $x = 0.05$  m

(b)  $x = 0.10$  m



(c) Flame Position  $x = 0.09$  m

Figure 4.10: Normalized pressure profiles at varying distances from the tube opening with the burner in place. Pressure measurements were taken at points on a 0.05 m grid, which is indicated by the circles. The pressures were then normalized by the center-line pressure in Fig. (4.8a), and a surface was interpolated from the data points. For convenience, the origin of the coordinate system used was placed at the center of the tube opening.

From these averages an aggregate ratio was calculated, the results of which are presented in Tab. (4.3). It was found that the acoustic pressures with the burner in place were  $1.22\times$  greater than those without the burner in place. This increase was most likely due to the acoustic waves reflecting off the burner's surface.

Table 4.3: Ratio of normalized acoustic pressures measured with the burner in place to corresponding pressures without the burner.

Stat	$x = 0.05$ m	$x = 0.10$ m	Aggregate
$\mu_{\hat{P}_H/\hat{P}_O}$	1.20	1.25	1.22
$\sigma_{\hat{P}_H/\hat{P}_O}$	0.07	0.06	0.07
$\sigma/\mu$	0.06	0.05	0.06

## 4.5 Acoustically Induced Flows

The initiation of acoustics induced air flows within the testing enclosure. When fog was introduced into the enclosure, it also showed that there was a net flow to this air movement moving away from the tube opening. To quantify the magnitude of the air movement, measurements of flows were made using the the hot-wire anemometer. As seen in Fig. (4.11), the magnitude of these flows showed sensitivity to both acoustic frequency and acoustic pressure. Since these flows were being induced by an oscillatory mechanism, it was not entirely clear whether the anemometer was measuring the speed of the net flow moving away from the tube opening, or an *rms* air speed of the oscillatory air movement. To elucidate the meaning of these measurements, a Particle Image Velocimetry (PIV) study of the flow was preformed.

### 4.5.1 PIV Analysis of Acoustic Flow

Visualization of the flow was achieved through the use of a fog machine, which produced a cloud of atomized ethylene glycol droplets. The nozzle of the fog

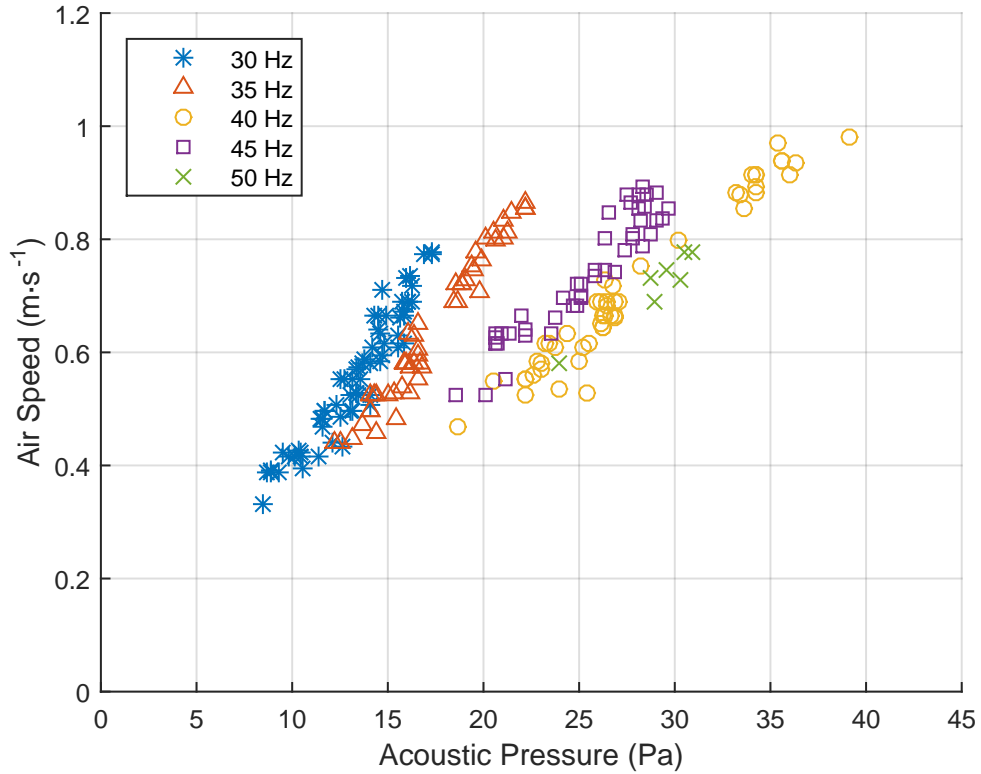


Figure 4.11: Anemometer measurements of the acoustically induced air flows, with burner in place, at differing acoustic pressures and frequencies. Measurements were taken at  $x = 0.09$  m from the tube opening, at approximately 0.02 m above the burner's surface.

machine was placed in the open end of the tube and fog was produced until it filled the tube. The open end of the tube was then sealed with a cylindrical foam plug for several minutes, giving time for the fog inside the tube to stagnate and excess fog to dissipate. Just prior to testing, the plug was removed and the speaker was activated. The acoustic excitations caused the fog in the tube to migrate into the enclosure, where videography of the process was obtained.

Illumination for the videography was created through the use of a back-lighting technique, which enhanced the visibility of the fog and yielded a sharper image. The back-lighting was created by mounting a T-5 fluorescent tube lamp, encased

in a plastic diffuser, to the outside of the testing enclosure. The lamp was situated so that the camera's view of it was obscured by the burner. This had the effect of creating the desired illumination without overexposing the image.

The video was recorded using the Phantom high speed camera which was situated 2.9 meters away from the burner. The camera used a 50 mm dual aperture lens, with the outer aperture open all the way and the inner aperture set to F-2. The focal point of the image was the burner's center, and the depth of field was approximately  $\pm 0.05$  m. The focal region of the image was, therefore, a 0.10 m wide region above the burner, centered on the longitudinal axis of the burner. The video itself was recorded at 400 frames per second, with auto exposure at a resolution of  $640 \times 480$  pixels.

Testing was done at 40 Hz and at acoustic pressures of 15 Pa, 37 Pa, and 54 Pa, as measured at the tube opening. Each test was allowed to evolve until there was an accumulation of fog around the enclosure that effectively obscured it from the camera; this process generally took about two minutes. Measurements of air speed and acoustic pressure were then taken at regular intervals from 0 to  $1.5 \times 10^{-2}$  m from the tube opening and at a height of  $2 \times 10^{-2}$  m above the plane of the burner.

The PIV analysis was performed on representative clips from the videos recorded using the PIVLab application in Matlab. The clips consisted of 32 sequential frames, which were loaded into PIVLab using A-B B-C sequencing. The Region of Interest (ROI) measured  $256 \times 112$  pixels, and is indicated by the rectangular

boundaries seen in the frames of Fig. (4.12). The distance scale for the frame was calibrated by the width of the burner, which measured 0.13 m. The time between each frame was 2.5 ms, which was determined by the recording rate of 400 fps.

For each frame, PIVLab calculated a  $u$  and  $v$  velocity component on a 90 point mesh within the ROI. A representative sample of the PIV results from the 15 Pa trial is shown in Fig. (4.12). Graphs of the calculated  $u$  and  $v$  components from the 15 Pa trail, at various distances from the tube opening and  $2 \times 10^{-2}$  m above the holder are shown in Fig.'s (4.13a) and (4.13b) respectively. Values of  $u_{rms}$  and  $v_{rms}$  were then calculated for each spatial point over the temporal domain. Finally, the magnitude of the composite  $rms$  flow velocity was calculated as:

$$U_{rms} = \sqrt{u_{rms}^2 + v_{rms}^2} \quad (4.8)$$

Specific values of  $U_{rms}$  were obtained at the points in the PIV mesh that most closely corresponded to the physical locations of the anemometer measurements. When the PIV determined values of  $U_{rms}$  are plotted along side the anemometer measured air speeds, as shown in Fig. (4.14a), it was noted that two were in generally good agreement. When the values of  $U_{rms}$  were plotted against the corresponding anemometer measured air speeds, as shown in Fig. (4.14b), it was found that the line of best fit was linear, had a slope of approximately equal to one, a  $y$ -intercept approximately equal to Zero, and a coefficient of determination approximately equal to one. From this, it was concluded that the air speeds

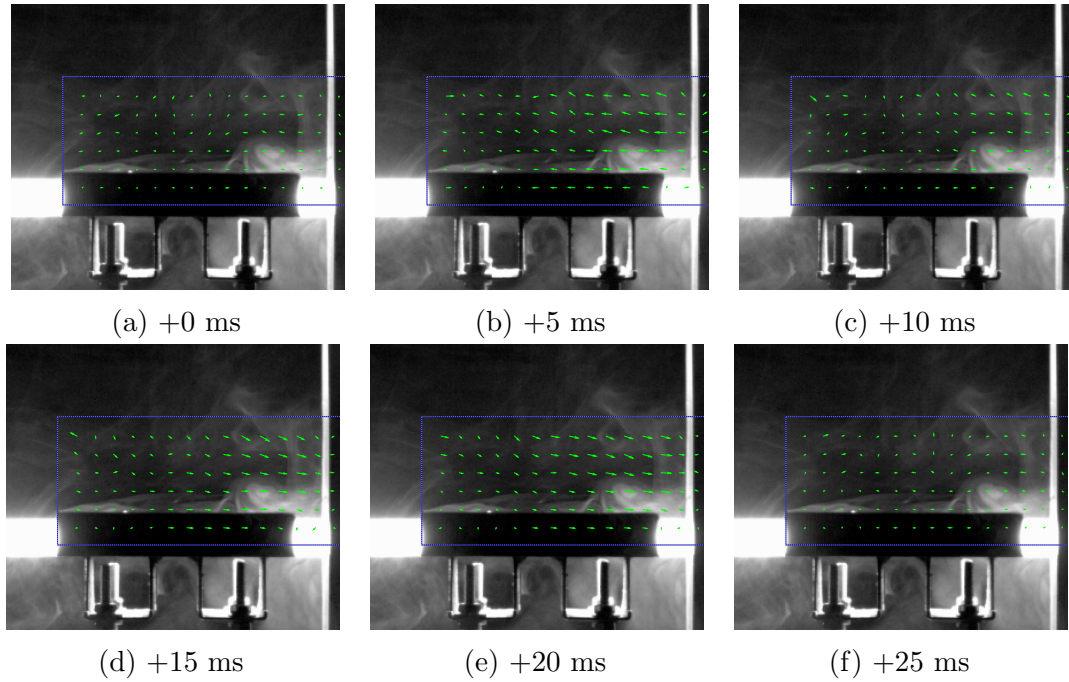


Figure 4.12: Sample PIV analysis at 40 Hz and 15 Pa acoustic pressure, as measured at the tube opening. The edge of the tube can be seen on the right edge of the frame. Each vector shown in the ROI is the composite of a calculated  $u$  and  $v$  component.

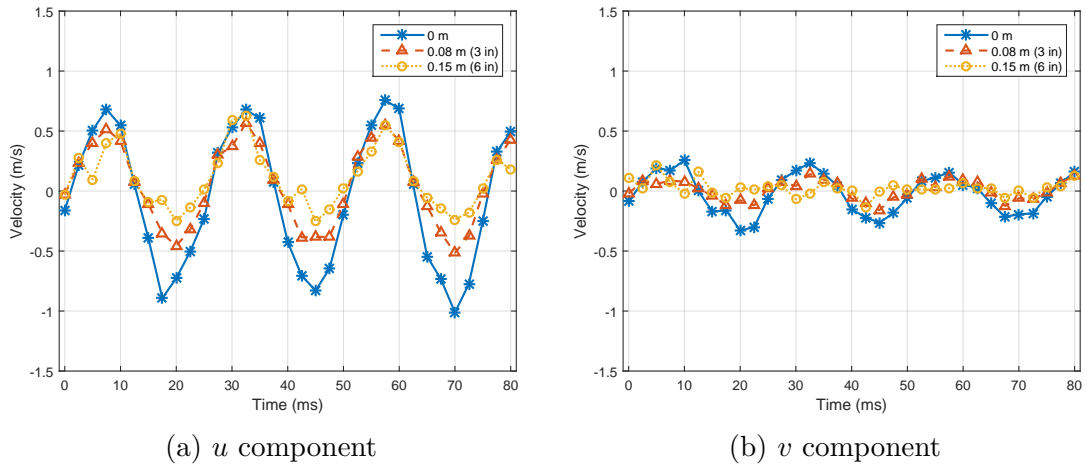
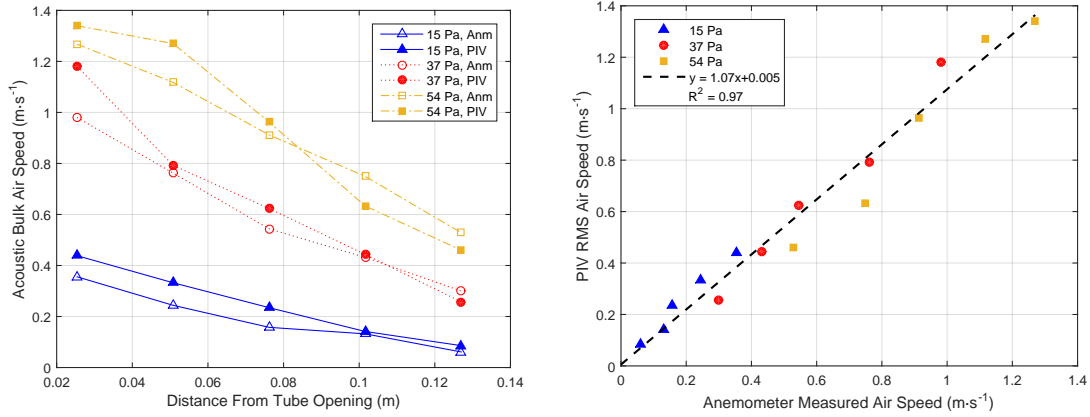


Figure 4.13: PIV calculated velocity components at 40 Hz and 17 Pa, as measured at the tube opening. The  $u$  components are shown in Fig. (4.13a), and the  $v$  components are shown in Fig. (4.13b). The values were taken from the PIV mesh points that most closely corresponded to the indicated distance, as measured from the opening of the tube, and at  $2 \times 10^{-2}$  m above the burner's surface.

measured by the anemometer were, in fact, the *rms* speeds of the oscillatory air movement.



(a) Comparison of  $U_{rms}$  and anemometer measurements

(b) Plot of  $U_{rms}$  vs. anemometer measurements

Figure 4.14: Comparison of PIV determined values of  $U_{rms}$  and the corresponding anemometer measurements. Fig. (4.14a) shows the two side-by-side, at various distances and acoustic pressures. Fig. (4.14b) shows the values of  $U_{rms}$  plotted against the corresponding anemometer measurements, and the line of best fit.

# Chapter 5

## Free Burn Characterization

### 5.1 Overview

A study of the line-flame without acoustic perturbations was conducted to serve as a point of reference for future tests. For each fuel used there were three burns conducted, during which time videography and mass readings were obtained simultaneously. From this data, values of mass loss rate (mlr or  $\dot{m}$ ), flame heights ( $L_f$ ), and flame width ( $W_f$ ) were calculated. Since all three quantities were parameterized by time, a direct comparison between the data points was made.

## 5.2 Mass Loss Rate

Values of  $\dot{m}$  were calculated from discrete mass readings taken at regular intervals during a burn. To obtain this data, the burner was placed on the balance without fuel and prepared for a test. The balance was then “Zeroed” and 3.5 mL of fuel was added. Data acquisition was then initiated, the fuel was ignited, and the flame was allowed to evolve without interference. During the evolution, mass readings were captured digitally once every second. The procedure was repeated three times for each fuel tested.

Using the data obtained, discrete values of  $\dot{m}$  for each burn were calculated as:

$$\dot{m}_i = \frac{m_i - m_{i+1}}{t_{i+1} - t_i} \quad (5.1)$$

where the ordering of the numerator and denominator were reversed to achieve a positive mlr. Values of  $\dot{m}$  were smoothed using a running average with a kernel of  $\pm 5$  s, which accounted for no more than 5% of the data points in any given set. The data points were averaged together and smoothed again using the same methodology. The entire process was repeated for each fuel species, and the results are shown in Fig. (5.1).

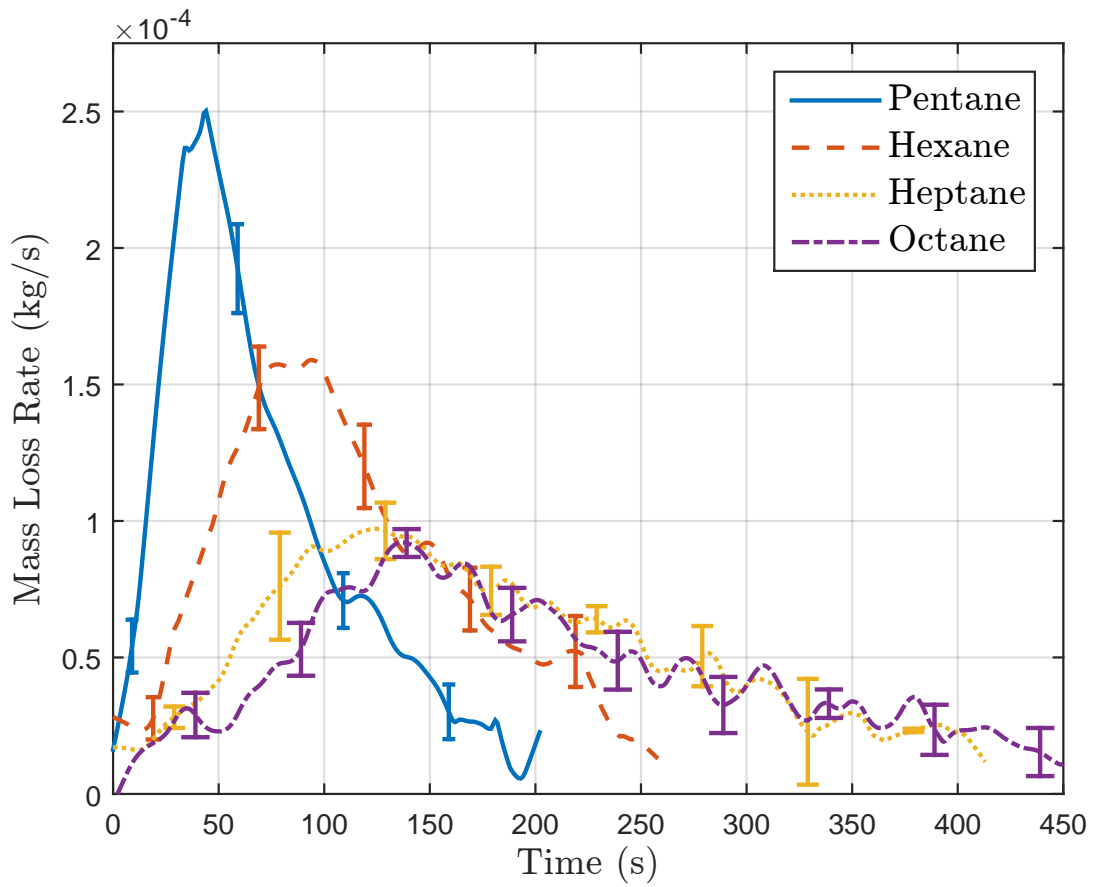


Figure 5.1: Free burn mlr profiles for each fuel tested. Each profile is the composite average of three individual profiles, and has been smoothed using a running average with a kernel of  $\pm 5$  s.

### **5.3 Flame Height**

Data for the flame height calculations was obtained simultaneously with the data for  $\dot{m}$ . For each burn, videography was obtained using a JVC Handycam situated 2.44 m (8 ft) from the flame. The metering for the videography was determined with a pre-test burn using pentane. During the most luminous portion of the flame's evolution, the camera's automatic metering set the aperture to F-5.6 with an exposure time of 1/400 s. The metering mode for the camera was then set to manual and these values were used for all tests. This was done so that pixel intensities were all scaled the same, allowing for a direct comparison of pixels between frames. The videos were then edited using Windows Live Movie Maker, where the image was converted into a gray-scale, and extraneous footage from before and after the burn was removed. A sample sequence of still images from a hexane burn is shown in Fig. (5.2).

As seen in Fig. (5.3), the flame's shape showed considerable variation over short time intervals, and a flame height could not be reliably estimated by visual inspection alone. To overcome this, the flame's height had to be estimated for each frame and smoothed over the temporal domain to find an average flame height profile.

To achieve this, the video was loaded into Matlab, and the indices of the pixels that formed the ROI shown in Fig. (5.3) were identified. The pixel intensities of every frame were evaluated, and those contained within the ROI were stored using the data structure shown in Tab. (5.1). A matrix, defined by Eq. (5.2), was

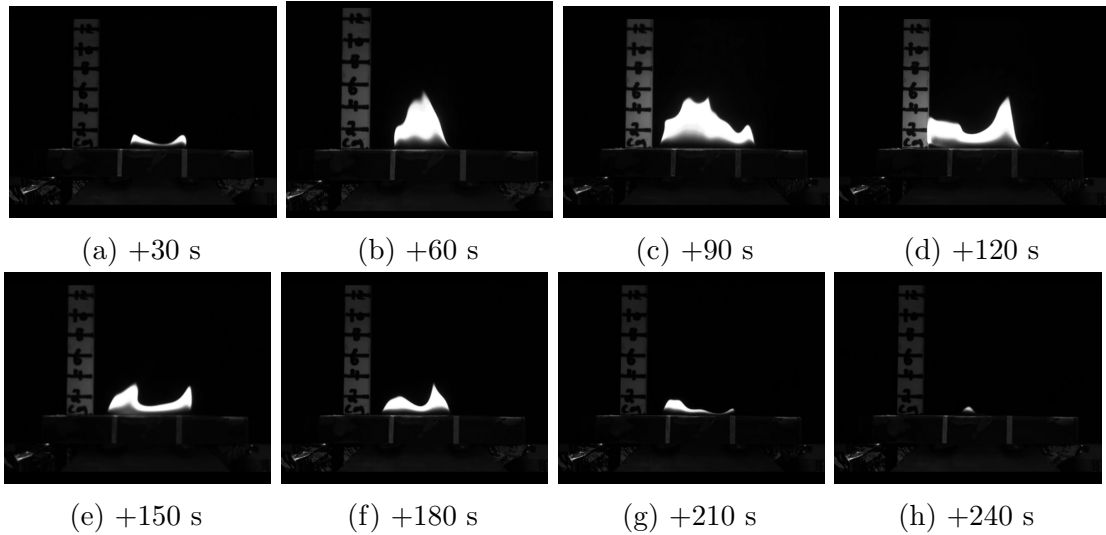


Figure 5.2: Sample sequence of still images from footage of a hexane free burn. The camera was situated 2.44 m away, and the video was shot at 30 fps with an aperture of F-5.6 and an exposure time of 1/400 s.

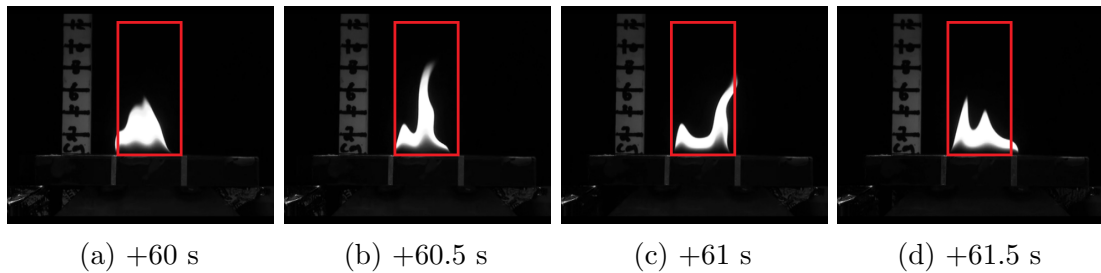


Figure 5.3: Sample sequence of still images from footage of a hexane free burn. The flame shape showed considerable variability over short time intervals. The ROI is indicated by the red rectangles.

then created whose columns were the average pixel intensities across the ROI in the horizontal direction for each frame. The width of the ROI had a noticeable effect on the values of these averages. If the width was increased, the value of the averages was seen to decrease. This is consistent with the fact that by increasing the width, more pixels with lower intensities were included. The ROI was therefore limited to just the region above the wick.

Table 5.1: Data structure for flame height calculations. The pixel intensities within the ROI are indexed spatially and temporally.

Frame 1				Frame 2				...	Frame $k$			
$I_{111}$	$I_{121}$	...	$I_{1j1}$	$I_{112}$	$I_{122}$	...	$I_{1j2}$	$I_{11k}$	$I_{12k}$	...	$I_{1jk}$	
$I_{211}$	$I_{221}$	...	$I_{2j1}$	$I_{212}$	$I_{222}$	...	$I_{2j2}$	$I_{21k}$	$I_{22k}$	...	$I_{2jk}$	
$\vdots$	$\vdots$	$\ddots$	$\vdots$	$\vdots$	$\vdots$	$\ddots$	$\vdots$	$\vdots$	$\vdots$	$\ddots$	$\vdots$	
$I_{i11}$	$I_{i21}$	...	$I_{ij1}$	$I_{i12}$	$I_{i22}$	...	$I_{ij2}$	$I_{i1k}$	$I_{i2k}$	...	$I_{ijk}$	

$$\bar{\mathbf{I}} = \frac{1}{N_j} \sum_{j=1}^{N_j} I_{ijk} = \begin{pmatrix} \bar{I}_{11} & \bar{I}_{12} & \cdots & \bar{I}_{1k} \\ \bar{I}_{21} & \bar{I}_{22} & \cdots & \bar{I}_{2k} \\ \vdots & \vdots & \ddots & \vdots \\ \bar{I}_{i1} & \bar{I}_{i2} & \cdots & \bar{I}_{ik} \end{pmatrix} \quad (5.2)$$

$$\bar{\mathbf{I}}^* = \frac{1}{2\Delta F} \sum_{k-\Delta F}^{k+\Delta F} \bar{I}_{ik} \quad (5.3)$$

The values of  $\bar{\mathbf{I}}$  were then smoothed over  $k$  using a running average with a kernel of  $\pm 150$  frames, which corresponded with  $\pm 5$  s of video footage. This created a second matrix,  $\bar{\mathbf{I}}^*$ , defined in Eq. (5.3). Each column of  $\bar{\mathbf{I}}^*$  is the temporally-smoothed luminous intensity profile of the flame at the time corresponding to the frame. A representative sample of smoothed profiles from a hexane burn is shown in Fig. (5.4).

To determine the flame height ( $L_f$ ), each column of  $\bar{\mathbf{I}}^*$  was first normalized by its maximum value to create a matrix  $\tilde{\mathbf{I}}^*$ , samples of which are shown in Fig. (5.5a). This was done since the maximum luminosity of the flame changed over time. A

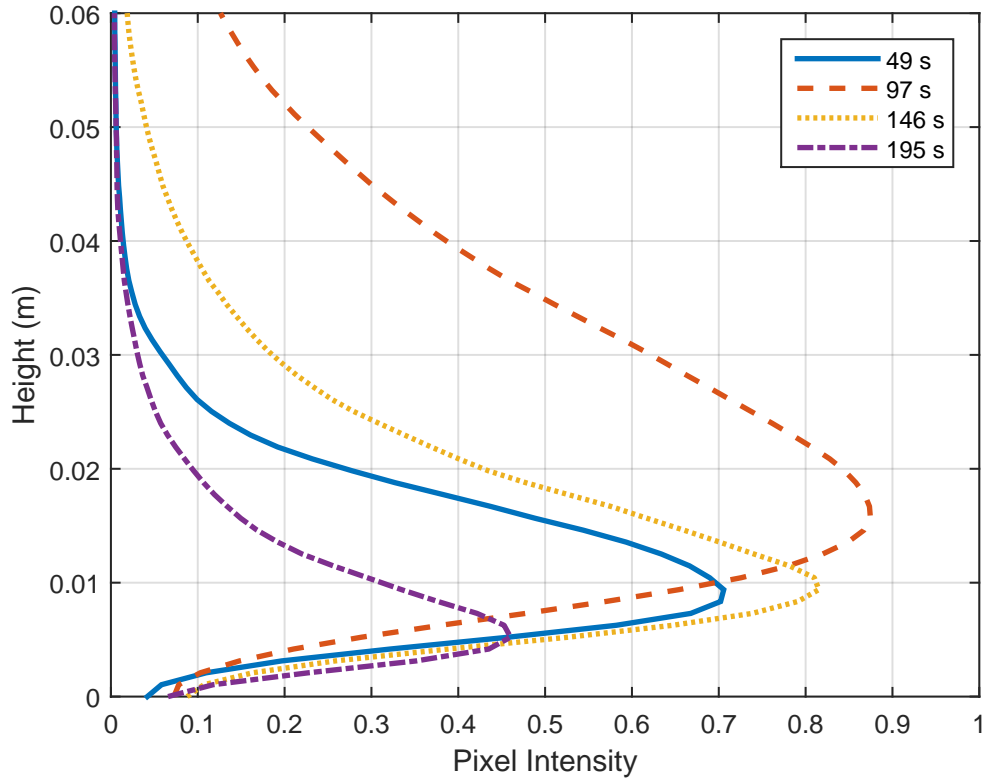
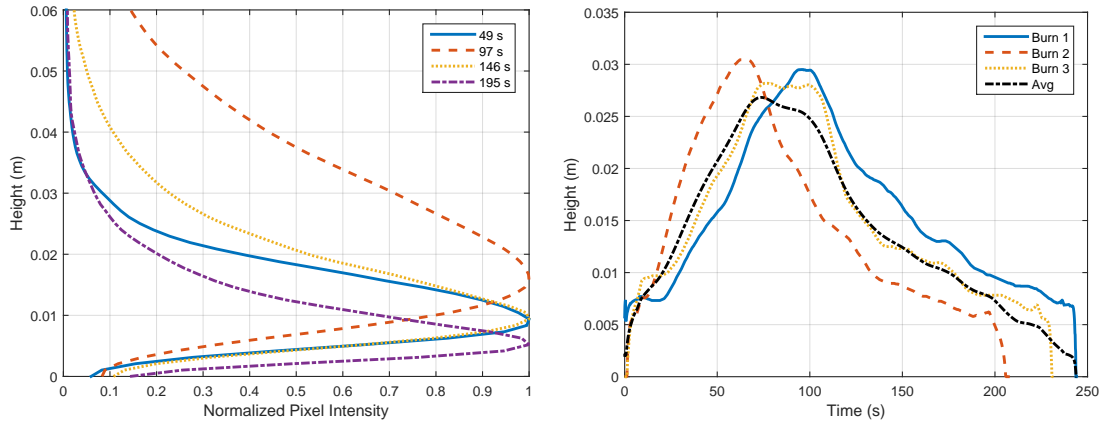


Figure 5.4: Hexane flame luminous intensity profiles. Each profile represents the luminous intensity of the flame over the ROI at the time indicated. The intensities at each height were smoothed over  $\pm 150$  frames.

cutoff intensity ( $I_o^*$ ) was then arbitrarily chosen, and a Matlab script was written which went down each column of  $\tilde{\mathbf{I}}^*$  to find the first data point where  $\tilde{I}_{ik}^* \geq I_o^*$ . From the indices of this point, a time and value of  $L_f$  were extracted. The results were then compared to the the video of the flame to check for consistency. To determine the best value of  $I_o^*$ , this process was repeated multiple times using varying values of  $I_o^*$  and sample video clips from each fuel. It was found that  $I_o^* = 0.70$  yielded predictions of  $L_f$  which were most consistent with the visual observations. Finally, using  $I_o^* = 0.70$ , the process was applied to each of the three videos for each fuel. As shown in Fig. (5.5b), the results were then averaged to

produce a composite flame height curves for each fuel. The composite flame height curves for all fuels tested is shown in Fig. (5.6).



(a) Normalized hexane flame intensity profiles.

(b) Individual and composite hexane flame height profiles.

Figure 5.5: Flame height determination method. The flame intensity profiles were normalized by the maximum intensity in each frame, as shown in Fig. (5.5a). A cutoff intensity of 0.7 was then used to determine  $L_f$  at the time associated with the frame. The individual and composite average results are shown in Fig. (5.5b).

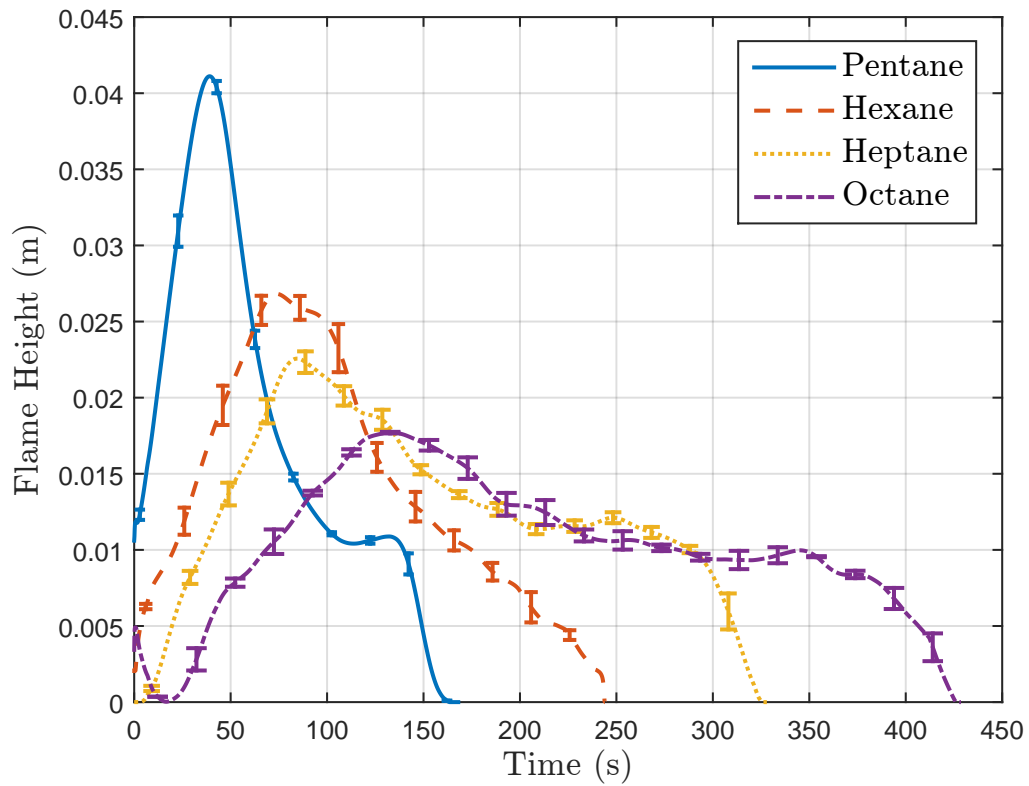
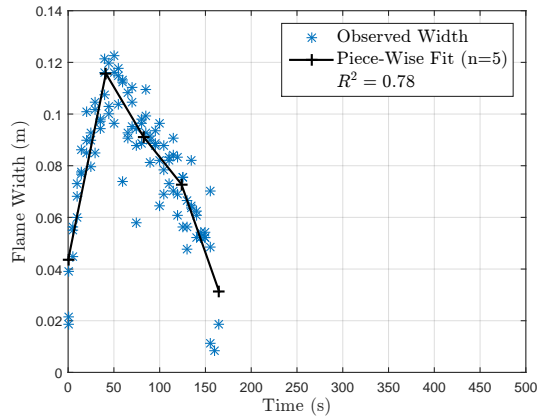


Figure 5.6: Profiles of  $L_f$  for the alkane fuels tested. Each profile is the composite of three individual profiles which have been averaged together and smoothed. The initial dip in the octane profile is due to the slow growth of the flame after the removal of the ignition lighter.

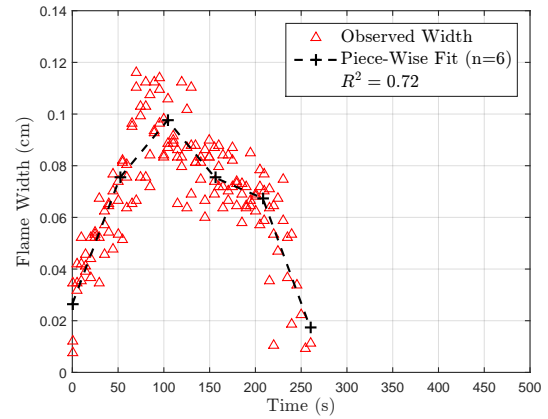
## 5.4 Flame Width

Due to reflections off the surface of the burner and visual obstructions in the image frame, the process used to determine  $L_f$  could not be used to determine  $W_f$ . Estimates of  $W_f$  were obtained instead from dimensional measurements of the video image itself. To do so, a paper ruler was made by photocopying a Staedtler brand metric ruler. The paper ruler was then taped to a computer screen cued to play the video of a burn. The ruler was placed so that it was parallel to the burner and just below where the flame emanated from the burner slot. The left and right edges of the flame were noted every five seconds, from which screen widths were determined. A scaling factor was found by taking the ratio of the burner's true length to the measured screen length. Using this ratio, the values of  $W_f$  could be estimated from the image measurements.

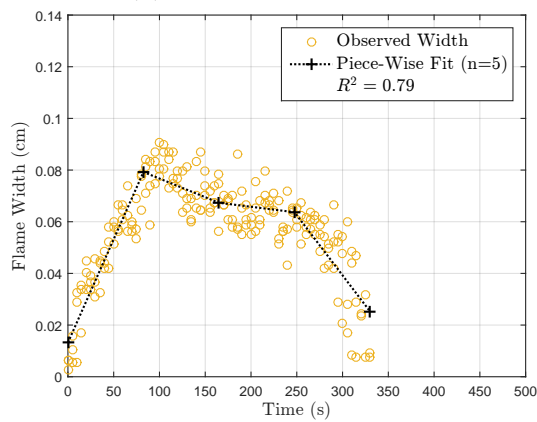
Since the sampling rate for  $W_f$  was significantly slower than that used for  $\dot{m}$  and  $L_f$ , there was an insufficient amount of data to reliably determine the uncertainty for each point. Therefore, instead of generating unique profiles for each burn, the data points from all three burns using a particular fuel were plotted *en masse*. The data points were then fitted with straight-line segments, from which the value of  $W_f$  could be estimated at any given time. The results, including the overall value of the coefficient of determination, are shown in Fig. (5.7).



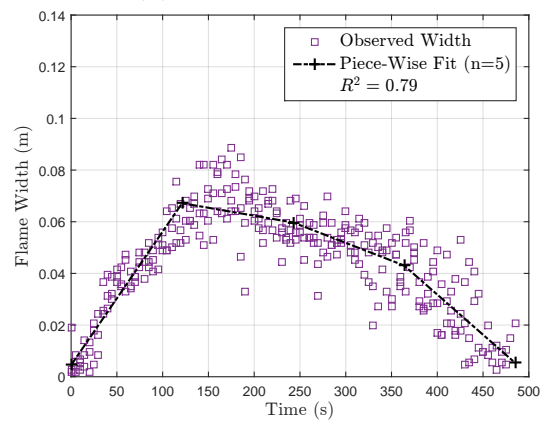
(a) Pentane flame width.



(b) Hexane flame width.



(c) Heptane flame width.



(d) Octane flame width.

Figure 5.7: Flame width determination. Visual observations of the flame's width were obtained every five seconds in each video. The results from all three videos for each fuel were then plotted *en masse* and fitted with straight line segments.

## 5.5 Flame Height Scaling

When juxtaposed next to each other, there is an obvious qualitative relationship between the profiles of  $\dot{m}$  and  $L_f$  for each fuel. As seen in Fig. (5.8), each profile has peaks and points of inflection at approximately the same time. However, since the burner used in this study was *sui generis*, existing flame height correlations were found to be inadequate predictors of the observed flame heights.

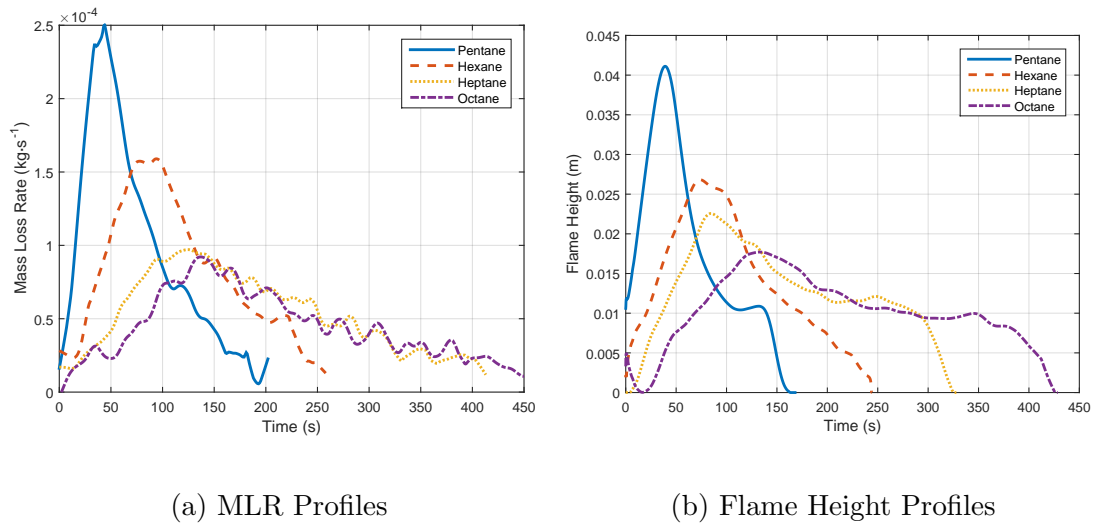


Figure 5.8: Side-by-side comparison of mlr and flame height profiles for fuels tested. The profiles show peaks and points of inflection at comparable times.

It was still desirable, though, to examine the link between the  $\dot{m}$  and  $L_f$  and  $W_f$ . Since these quantities were all parametrized by time, a direct comparison on a temporal basis could be made. To do so, an mlr per unit-width of flame ( $\dot{m}'$ ) was calculated as:

$$\dot{m}' = \dot{m}/W_f \quad (5.4)$$

A heat release rate per unit flame-width ( $\dot{Q}'$ ) was then calculated as:

$$\dot{Q}' = \Delta h_c \dot{m}' \quad (5.5)$$

where the heat of combustion per unit mass ( $\Delta h_c$ ) for each fuel is discussed in Sec. (7.3.1). Values of  $L_f$  were then plotted against  $\dot{Q}'$ , as shown in Fig. (5.9).

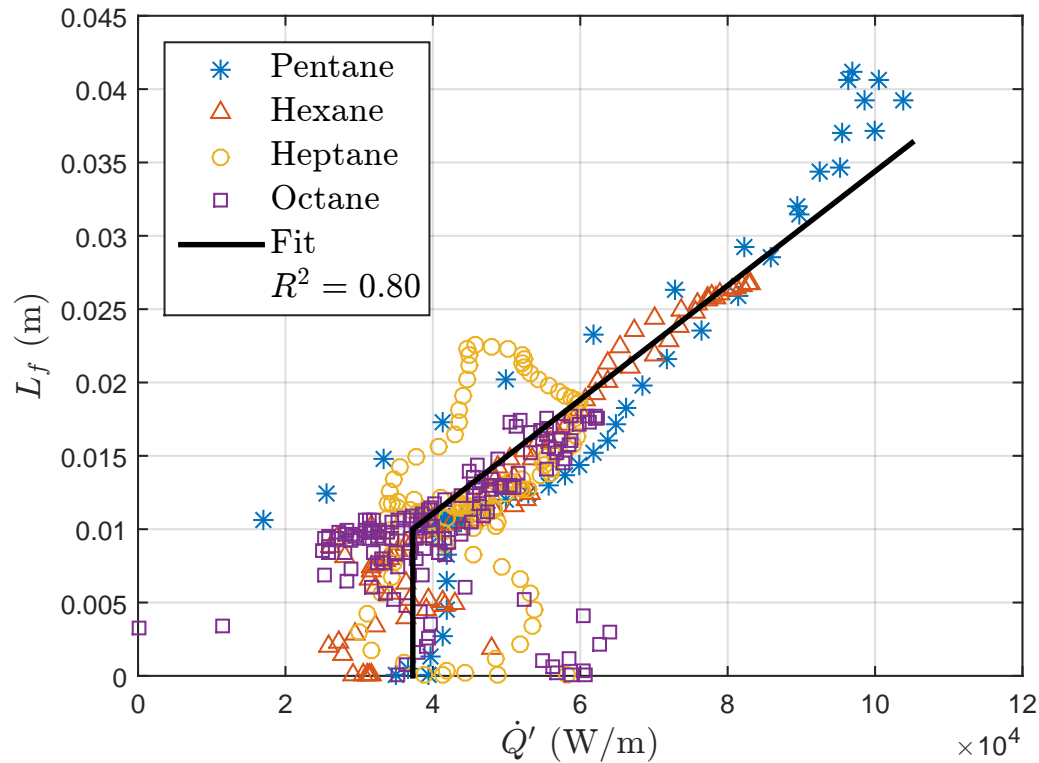


Figure 5.9: Flame height vs. heat release rate per unit flame width. Values of  $L_f$  below 0.01 m were centered about a constant value. Values of  $L_f$  above 0.01 m showed a linear relationship with  $\dot{Q}'$ .

Close examination of Fig. (5.9) showed that values of  $L_f < 0.01$  m were clustered about a constant value of  $\dot{Q}'$ , and this point appeared to constitute a minimum heat flux below which a flame could not exist. On average, this value was found to be  $3.73 \times 10^4$  W/m, with a standard deviation  $0.95 \times 10^4$  W/m. The fact that a

minimum value of  $\dot{Q}'$  exists is consistent with stagnant layer theory, which requires a minimum heat release rate to sustain a flame [17].

For values of  $L_f \geq 0.01$  m, there appeared to be a linear relationship between  $L_f$  and  $\dot{Q}'$ . The line of fit for this section was calculated to be:

$$L_f = \left(3.89 \times 10^{-7} \frac{\text{m}^2}{\text{W}}\right) \dot{Q}' - 4.5 \times 10^{-3} \text{ m} \quad (5.6)$$

This linearity is consistent with the Burke-Schumann analysis for laminar diffusion flame height [38].

# Chapter 6

## Burning Rate in an Acoustic Field

### 6.1 Overview

A study of the flame's burning rate while experiencing acoustic perturbations was conducted to further elucidate the effects of acoustics on the flames produced. Only hexane fuel was used for this study, since the study required a large number of tests and it was the only fuel for which there was an adequate supply. To conduct the tests, the vertical rods used to support the burner were removed and the Mettler Toledo balance was placed in front of the tube opening, as shown in Fig. (6.1). The burner was situated on the balance so that it still occupied the same position shown in Fig. (2.7). Samples were placed in the holder, ignited, and allowed to burn

freely for 10 seconds. The speaker was then activated and the flame was allowed to burn under acoustic excitation until it self-extinguished. After self-extinguishment, measurements of the acoustic pressure and *rms* air speed were taken at the flame position approximately 0.02 m above the flame holder.

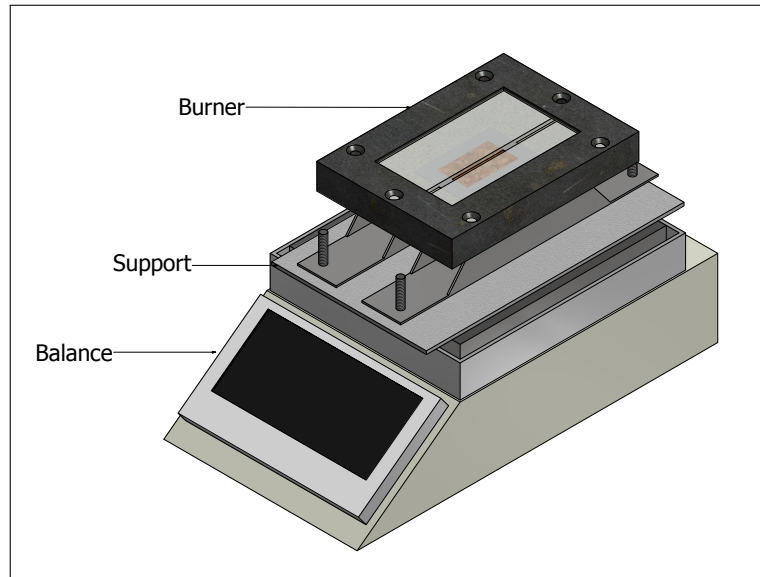


Figure 6.1: Burner placed on balance for mlr experiments. The burner was situated so that it occupied the same position indicated in Fig. (2.7).

Tests were conducted at 30, 35, 40, and 45 Hz. For each frequency used, a series of tests were done at increasing acoustic pressure. The pressures tested for each frequency were limited to those below which acoustic extinction occurred, a phenomenon described in Chap. (7). After the acoustic experiments, the speaker was removed and replaced with a fan. This facilitated tests using forced flows and served as a basis for comparison. At each acoustic pressure and fan speed tested, three trials were performed, and a composite profile was generated using the same methodology described in Sec. (5.2). Since the fuel used for these experiments

came from a different stock than that used for the free-burn characterizations described in Chap. (5), additional free-burn tests were performed. On average, 3.5 mL of the stock used for these experiments burned for 11 s less than that used in the previous experiments.

## 6.2 MLR Profiles

Representative mlr profiles for each frequency tested are presented in Fig. (6.2). For each profile, the *rms* acoustic pressure and *rms* air speed measured at the flame position are shown in the legend. Each graph also contains the composite free-burn profile, which is indicated by the black dashed line.

With the exception of the profiles at 45 Hz, the acoustics had an appreciable effect on the growth phase of the flame. At low pressures and air speeds, the growth phase of the flame was inhibited by the acoustics. As the pressure and air speed increased though, the growth phase was enhanced. This can be seen by noting that as the acoustic pressure and air speed increased, the peak values of  $\dot{m}$  increased and the time to achieve peak  $\dot{m}$  decreased. After peak  $\dot{m}$  was achieved though, all profiles tended to converge towards the free-burn profile. This indicated that the decay phase of the flame was insensitive to the acoustic perturbations.

Representative profiles of  $\dot{m}$  using a fan driven-flow are presented in Fig. (6.3). The fan had a minimum operating power of 1.5 W, meaning the slowest flows

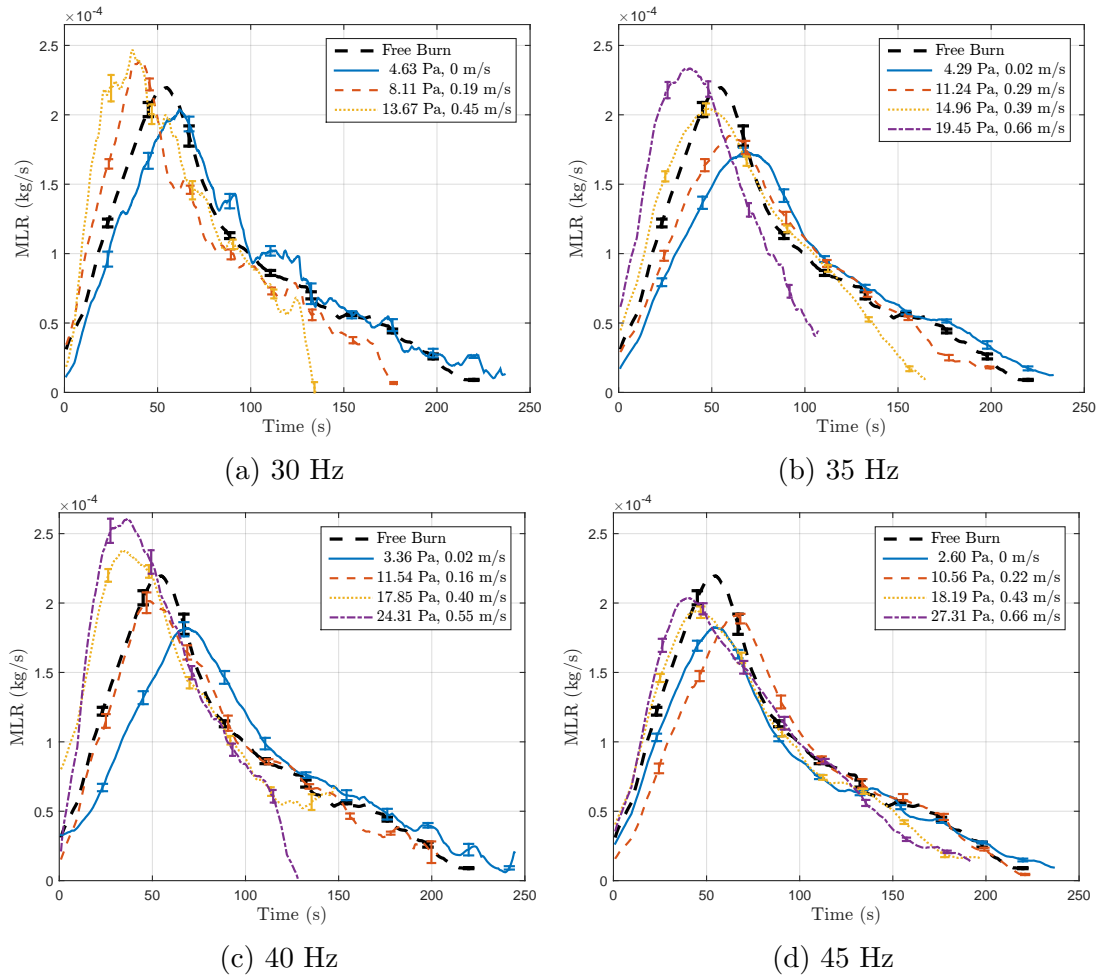


Figure 6.2: Hexane mLR profiles at varying frequencies and acoustic pressures. Each profile is the composite of three individual tests. The acoustics tended to inhibit flame growth at low pressures and air speeds, and enhanced flame growth as the pressure and air speed increased. All profiles though converged towards the free-burn profile after peak  $\dot{m}$  was achieved.

that could be tested were 0.24 m/s. The fastest flows that could be tested were limited by the speed at which extinction would occur, which was found to be 0.74 m/s. This was significantly less than the fan-driven extinction flow for a hexane flame discussed in Chap. (7), which was found to be 1.58 m/s. The discrepancy is attributed to the presence of the mass balance in the flow path, which was not present in extinction experiments and which significantly affected air flows.

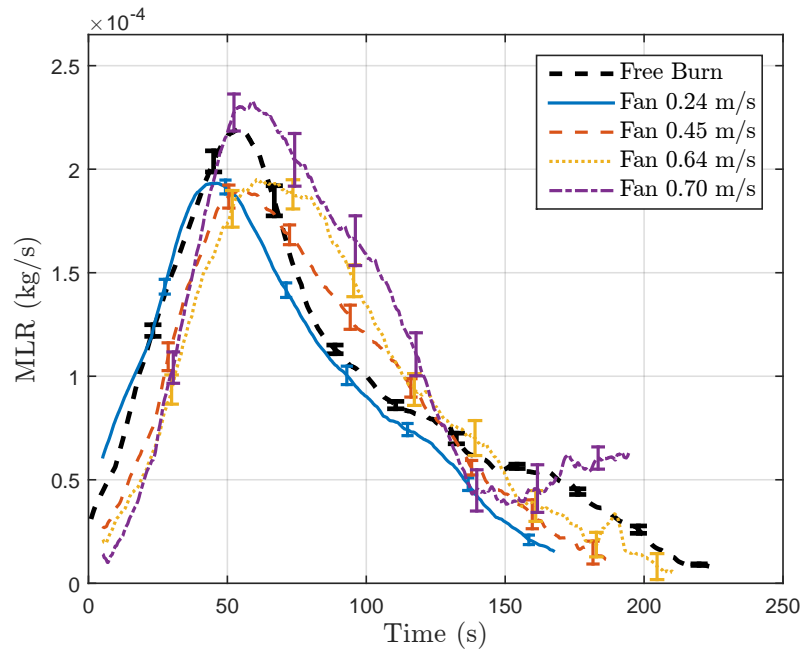


Figure 6.3: Hexane mLR profiles at varying fan driven flows. Each profile is the composite of three individual tests. As the fan driven flows increased the growth phase of the flame was inhibited. All profiles though converged towards the free-burn profile after peak  $\dot{m}$  was achieved.

Although the trends were not nearly as dramatic in the fan-driven profiles as they were in the acoustic profiles, certain patterns were discernible. As previously noted, increasing the acoustic air speed enhanced the growth phase of the flame. In contrast though, increasing the fan-driven air speed inhibited the flames' growth. This can be seen in Fig. (6.3) by noting the rightward shift of the profiles as the flow speed increases. As with the acoustic profiles though, once peak  $\dot{m}$  was achieved, the profiles converged towards the free-burn profile.

## **6.3 MLR Profile Comparisons**

To further understand the effects of the acoustics on burning rate, comparisons of  $\dot{m}$  were made by examining profiles under comparable conditions. First, profiles at different frequencies but comparable acoustic pressures were examined. Then, profiles at different frequencies but comparable air speeds were examined. Included in this examination were profiles made with a fan-driven flow whose magnitude was comparable. Finally, average mlr's were calculated and then compared on the basis of acoustic pressure and *rms* air speed.

### **6.3.1 Comparable Acoustic Pressures**

Graphs of mlr profiles at comparable acoustic pressures are presented in Fig. (6.4); the error bars have been omitted for clarity. At constant acoustic pressure, no link could be found between frequency and peak  $\dot{m}$ , or frequency and time to achieve peak  $\dot{m}$ . More obvious, though, were the effects of increasing acoustic pressure. As the acoustic pressure increased, both the rate of flame growth and magnitude of peak  $\dot{m}$  increased. Since the magnitude of the *rms* air speed increased with acoustic pressure, this observation is consistent with the trends noted in Sec. (6.2).

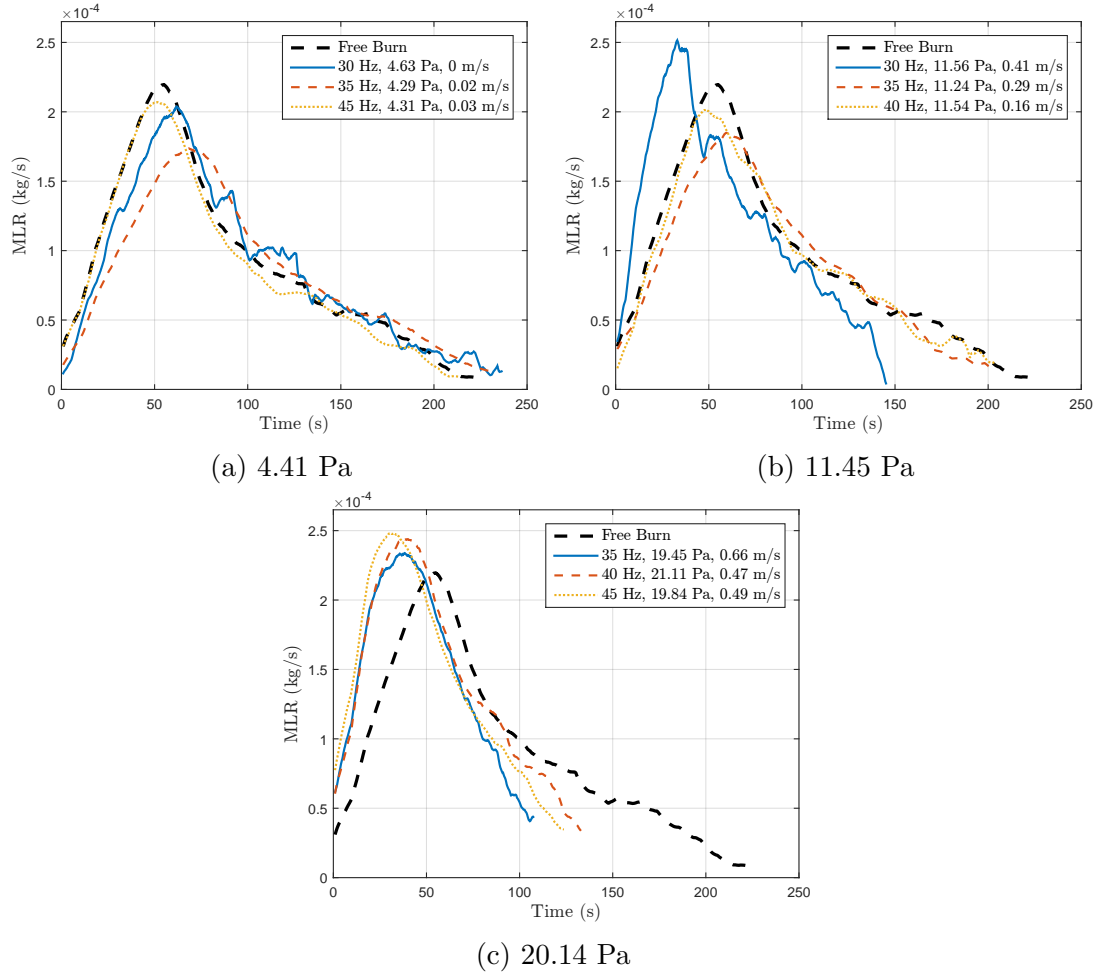


Figure 6.4: Mlr profiles at varying frequencies and comparable acoustic pressures. The pressures noted in the subtitles are the average acoustic pressures of the profiles presented.

### 6.3.2 Comparable Air Speeds

Graphs of mlr profiles at comparable *rms* air speeds are presented in Fig. (6.5).

Included in these graphs are profiles with a fan-driven flow at roughly the same magnitude. Among the acoustically-perturbed flames, no discernible pattern could be identified with respect to changes in frequency at a constant air speed. All acoustically perturbed flames, though, did exhibit faster growth and peak values of  $\dot{m}$  than the corresponding fan profile. Perhaps most probative is the consistency

of the acoustically-perturbed profiles. With the exception of the 35 Hz profile in Fig. (6.5b), all acoustic profiles were nearly identical at comparable *rms* air speeds. This suggests that for the acoustic profiles, rates of growth were most strongly influenced by the magnitude of oscillatory air movement. The acoustic pressure and frequency only influenced *mlr* insofar as they contributed to the *rms* air speed.

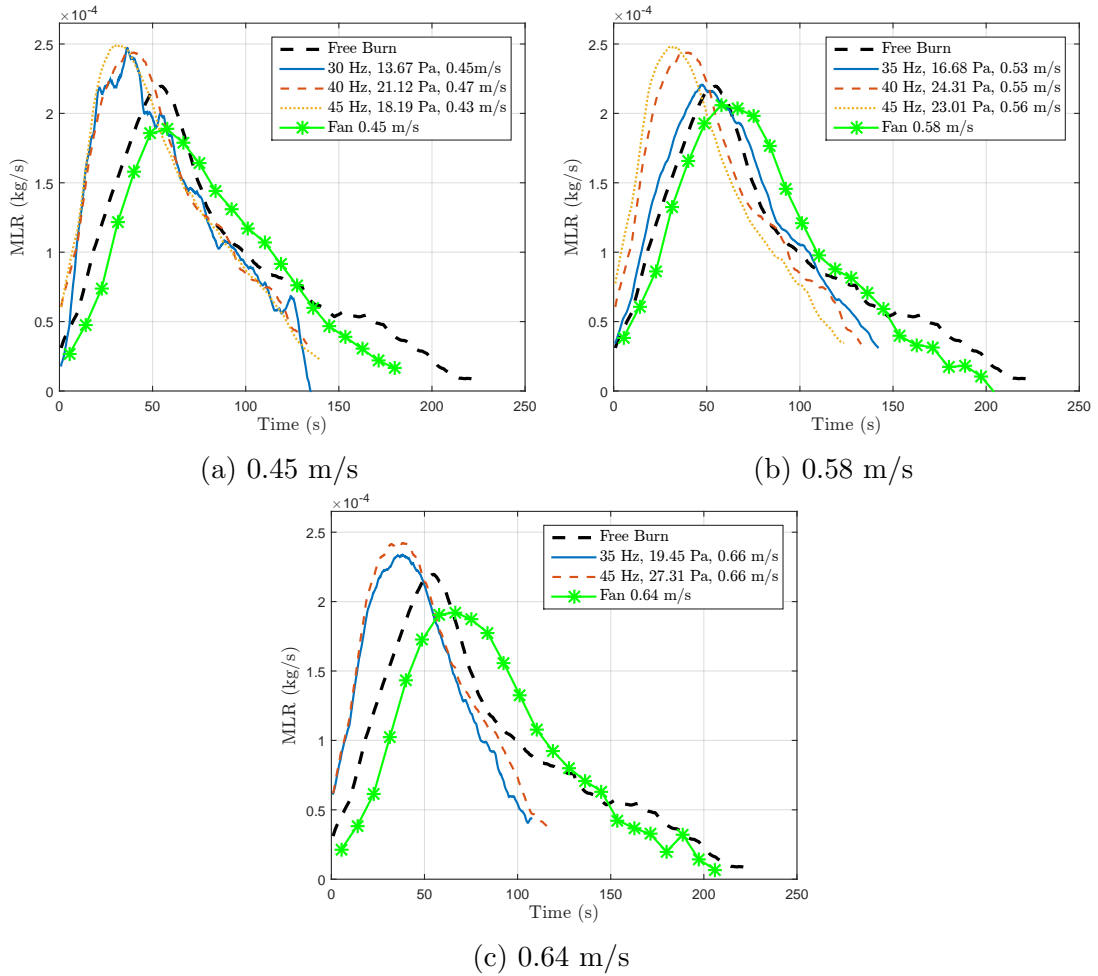


Figure 6.5: Profiles of  $\dot{m}$  at varying frequencies and comparable air speeds. The air speeds noted in the subtitles are the average acoustic air speeds of the profiles presented. The *mlr* profile from a fan driven flow at a comparable speed is also presented.

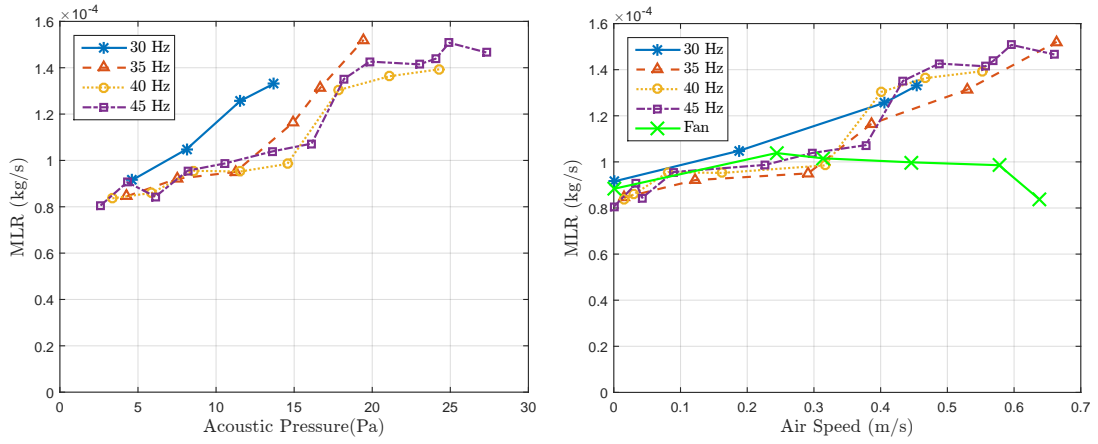
### 6.3.3 Average Mass Loss Rates

Values of average mlr ( $\tilde{m}$ ) were calculated by taking the ratio of total fuel lost to total burning time. These values were compared on the basis of acoustic pressure ( $P$ ) and *rms* air speed ( $U_A$ ); the results are presented in Fig.'s (6.6a) and (6.6b) respectively. Included in Fig. (6.6b) are values of  $\tilde{m}$  for the flames perturbed by the fan-driven flows.

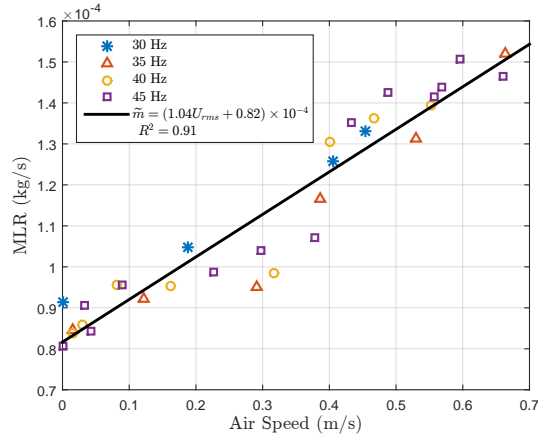
Examining Fig's (6.6a) and (6.6b), it can be seen that there is an obvious positive correlation between  $\tilde{m}$  with both  $P$  and  $U_A$ . Interestingly though, values of  $\tilde{m}$  for the fan-driven experiments were roughly constant, with an average of  $0.86 \times 10^{-4}$  kg/s. To determine which parameter  $\tilde{m}$  was more closely associated with in the acoustic experiments, two statistical tests were performed. The first test calculated the coefficient of correlation ( $r$ ) between the aggregate data set of  $\tilde{m}$  and the argued parameters of  $P$  and  $U_A$ . The second test was to fit linear curves to the aggregate data set of  $\tilde{m}$  and then compare the coefficients of determination for the same argued parameters.

For  $\tilde{m}$  vs.  $P$ , it was found that  $r = 0.92$  and  $R^2 = 0.83$ . For  $\tilde{m}$  vs.  $U_A$  though, it was found that  $r = 0.96$  and  $R^2 = 0.91$ ; the line of fit for this data is shown in Fig. (6.6c). The results of these two tests indicate that  $\tilde{m}$  was more strongly influenced by  $U_A$  than by  $P$ . They also bolster the supposition made in Sec. (6.3.2), that acoustic pressure only influenced the burning rate insofar as it contributed to the oscillatory movement of air.

Although not perfectly analogous, the link between the speed of oscillatory air movement and burning rate is consistent with the observations of other authors. In studies of flame spread in opposed flows, both Fernandez-Pello and De Ris *et al* showed that increased flow speed enhanced burning rate. This was due to the flames being forced closer to the fuel surface, which enhanced heat transfer into the fuel bed [39, 40]. It is reasonable to conclude that a similar phenomenon was occurring due to the oscillatory air movement over the fuel, and this conclusion is consistent with the visually observed behavior of the flame during testing. Using the same analogy, the linearity of the trend is also consistent with the work of Hu *et al*, who studied the burning rate of various sized gasoline pool fires in cross-flows. The linearity observed by Hu arose from the same mechanism described by Fernandez-Pello and De Ris, where the flame was forced closer to the fuel's surface with increasing air speed [41].



(a) Average mlr vs. acoustic pressure. (b) Average mlr vs. *rms* air speed.



(c) Average mlr vs. *rms* air speed with fitted curve.

Figure 6.6: Profiles for average mlr. Fig. (6.6a) shows  $\tilde{m}$  plotted against  $P$ , while Fig. (6.6b) shows  $\tilde{m}$  plotted against the  $U_A$ . Included in Fig. (6.6b), are the values of  $\tilde{m}$  for the fan driven experiments plotted against the bulk air speed of the fan flow. Fig. (6.6c) shows the values of  $\tilde{m}$  for the acoustic experiments with the line of fit.

# Chapter 7

## Acoustic Extinction

### 7.1 Experimental Summary

Flames produced using the fuels n-pentane, n-hexane, n-heptane, n-octane, and JP-8 aviation fuel were subjected to acoustic perturbations at varying frequencies and acoustic pressures to determine extinction criteria. For comparison, fan-driven flows were also created in the testing enclosure and conditions were measured.

#### 7.1.1 Acoustic Extinction Results

The conditions required to cause an acoustic extinction of a particular fuel at a particular frequency ( $\omega$ ) were determined by finding the lowest speaker power that could cause three consecutive extinction events within 10 seconds of speaker

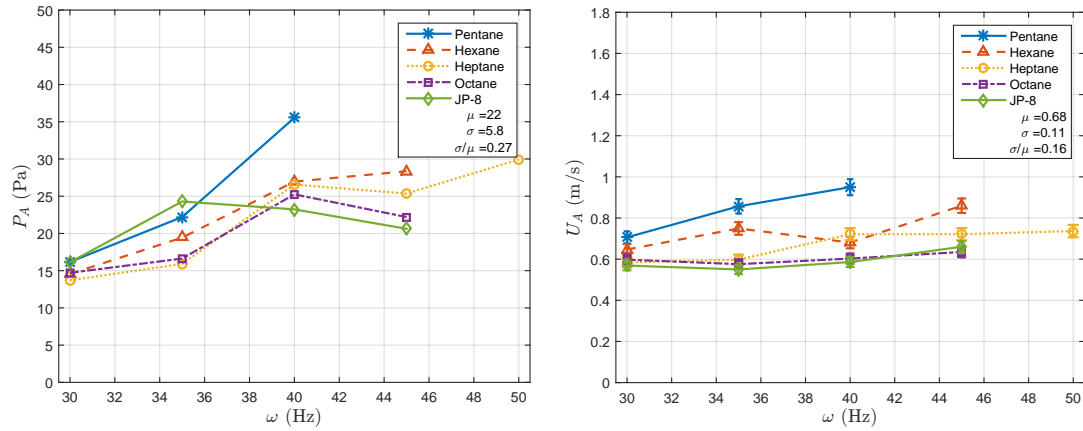
activation. For each test, the flame was allowed to burn unperturbed until it reached a height of approximately 0.02 m. The speaker was then activated to determine if acoustically driven extinction could be achieved. Immediately after the flame was extinguished, the acoustic pressure ( $P_A$ ) and *rms* acoustic air speed ( $U_A$ ) were measured. At extinction, the reported acoustic pressure ( $P_{A_{ext}}$ ) and *rms* air speed of the acoustically induced flow ( $U_{A_{ext}}$ ) were calculated as the average of the three individual trials. The results, including uncertainties, are summarized in Tab. (7.1); the uncertainties are discussed in Appendix (A.1).

Table 7.1: Acoustic Flame Extinction Test Results

Fuel	$\omega$ (Hz)	$P_{A_{ext}}$ (Pa)	$U_{A_{ext}}$ ( $\text{m} \cdot \text{s}^{-1}$ )
Pentane	30	$16.2 \pm 0.1$	$0.71 \pm 0.02$
	35	$22.2 \pm 0.2$	$0.86 \pm 0.03$
	40	$35.5 \pm 0.2$	$0.95 \pm 0.03$
Hexane	30	$14.6 \pm 0.1$	$0.65 \pm 0.02$
	35	$19.5 \pm 0.1$	$0.75 \pm 0.02$
	40	$27.0 \pm 0.2$	$0.68 \pm 0.02$
	45	$28.4 \pm 0.2$	$0.86 \pm 0.03$
Heptane	30	$13.7 \pm 0.1$	$0.58 \pm 0.02$
	35	$15.9 \pm 0.1$	$0.60 \pm 0.02$
	40	$26.6 \pm 0.2$	$0.72 \pm 0.02$
	45	$25.5 \pm 0.2$	$0.72 \pm 0.02$
	50	$29.9 \pm 0.2$	$0.74 \pm 0.02$
Octane	30	$14.7 \pm 0.1$	$0.60 \pm 0.02$
	35	$16.6 \pm 0.1$	$0.58 \pm 0.02$
	40	$25.3 \pm 0.2$	$0.60 \pm 0.02$
	45	$22.2 \pm 0.2$	$0.64 \pm 0.02$
JP-8	30	$16.1 \pm 0.1$	$0.57 \pm 0.02$
	35	$24.3 \pm 0.1$	$0.55 \pm 0.02$
	40	$23.2 \pm 0.2$	$0.59 \pm 0.02$
	45	$20.6 \pm 0.1$	$0.66 \pm 0.03$

Graphs of the data from Tab. (7.1) are shown in Fig.'s (7.1a) and (7.1b). The uncertainties in  $P_{A_{ext}}$  were not included in Fig. (7.1a) since they were smaller than

the data markers used. For each graph, the values of  $\mu$ ,  $\sigma$ , and the Coefficient of Variation ( $CV=\sigma/\mu$ ), are shown in the legend.

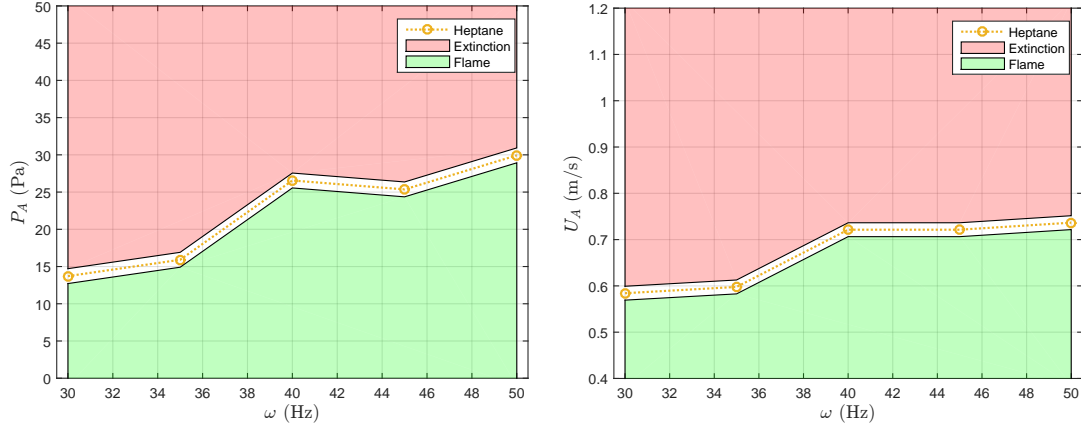


(a) Average acoustic pressure ( $P_A$ ) measured at extinction for differing fuels at differing frequencies

(b) Average acoustic *rms* air speed ( $U_A$ ) measured at extinction for differing fuels at differing frequencies

Figure 7.1: Average acoustic extinction conditions for fuels tested. Each data point is the average of the measured conditions at the lowest speaker power which could cause three consecutive extinctions. The uncertainties in  $P_A$  were omitted from Fig. (7.1a) since they were smaller than the data markers used.

The curve for each fuel in Fig.'s (7.1a) and (7.1b) can be thought of as a boundary delineating conditions where the flame can and cannot exist. As illustrated with the heptane data in Fig.'s (7.2a) and (7.2b), at conditions below the boundary the flame can continue to burn. At conditions above the boundary though, flame extinction occurs.



(a) Heptane extinction boundary defined by  $P_A$

(b) Heptane extinction boundary defined by  $U_A$

Figure 7.2: Heptane extinction boundaries defined by  $P_A$  and  $U_A$ . At acoustic pressures below the curve in Fig. (7.2a) the flame continues to burn; at pressures above the curve, flame extinction occurs. Likewise, the flame continues to burn at acoustic flows below the curve in Fig. (7.2b); at flows above the curve, flame extinction occurs.

### 7.1.2 Fan-Driven Extinction Results

The conditions required to cause a fan-driven extinction of a particular fuel were determined by finding the lowest fan power that could cause three consecutive extinction events within 10 seconds of fan activation. The reported fan-driven bulk air speeds at extinction ( $U_{F_{ext}}$ ) were calculated as the average of the three individual trials. The results, including uncertainties, are summarized in Tab. (7.2); the uncertainties are discussed in Appendix (A.1).

A graph of the data from Tab. (7.2), including the uncertainties, is shown in Fig. (7.3). The data points have been plotted against the molar mass for each fuel so that the error bars are visible.

Table 7.2: Fan-Driven Flame Extinction Test Results

Fuel	$U_F$ ( $\text{m} \cdot \text{s}^{-1}$ )
Pentane	$1.55 \pm 0.03$
Hexane	$1.58 \pm 0.03$
Heptane	$1.89 \pm 0.04$
Octane	$1.96 \pm 0.04$
JP-8	$2.03 \pm 0.08$

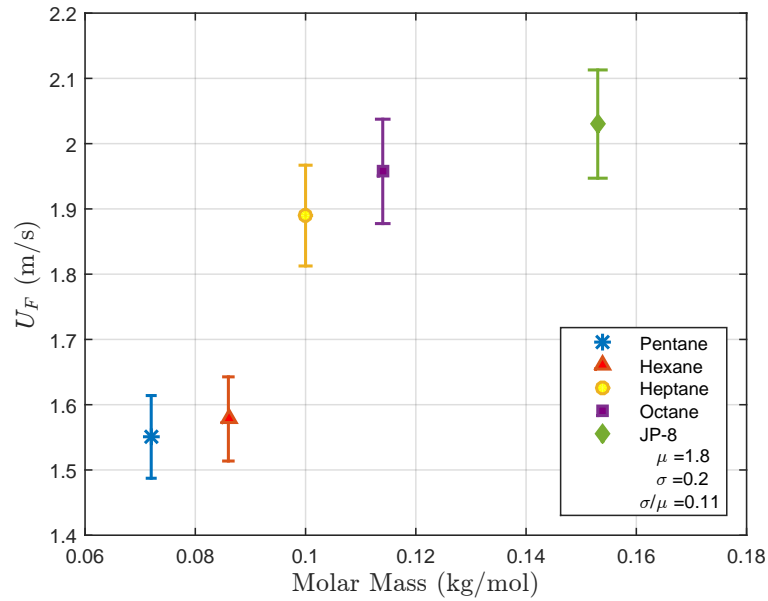


Figure 7.3: Average fan driven bulk air speeds ( $U_F$ ) measured for extinction of differing fuels. Each data point is the average of the measured conditions at the lowest speaker power which could cause three consecutive extinctions.

## 7.2 Proposed Acoustic Extinction Theory

### 7.2.1 Comparison of Results

When the values of  $U_{F_{ext}}$  are considered with the those of  $U_{A_{ext}}$ , two observations become apparent:

1. The average value of  $U_{F_{ext}}$  ( $\bar{U}_{F_{ext}} = 1.8$  m/s) is approximately  $2.5\times$  the average value of  $U_{A_{ext}}$  ( $\bar{U}_{A_{ext}} = 0.7$  m/s).
2. The general “ordering” of the fuels between the two scenarios is reversed. For the fan-driven extinctions, values of  $U_{F_{ext}}$  were seen to increase with the fuel’s molar mass, while for the acoustic extinctions, values of  $U_{A_{ext}}$  were seen to decrease. This is clearly shown in Fig. (7.4), which compares values of  $U_{F_{ext}}$  for the different fuels to those of  $U_{A_{ext}}$  at 35 Hz. The data here is plotted against the heat of combustion per unit mole ( $\Delta H_c$ ) for each fuel, which scales with the fuel’s molar mass [42]. This is done to facilitate a comparison of extinction strain rates, which is discussed in Sec. (7.2.2).

## 7.2.2 Discussion of Results

Using a “Damköhler” analysis, it has been shown that flame stretch can be a primary cause of flame extinction [18]. Flame stretch itself is caused by hydrodynamic strain in the flow of the oxidizer and fuel, and by localized changes in flame speed due to variations in temperature and species concentrations [43]. Except for cases where the turbulent length scales of the flow are smaller than the flame thickness, it is the hydrodynamic effects that have the strongest influence on flame stretch in laminar flames [5].

Examining the fan-flow visualization in Fig. (7.5), it can be seen that a boundary layer formed over the burner shortly after the fan was activated. The fan-driven

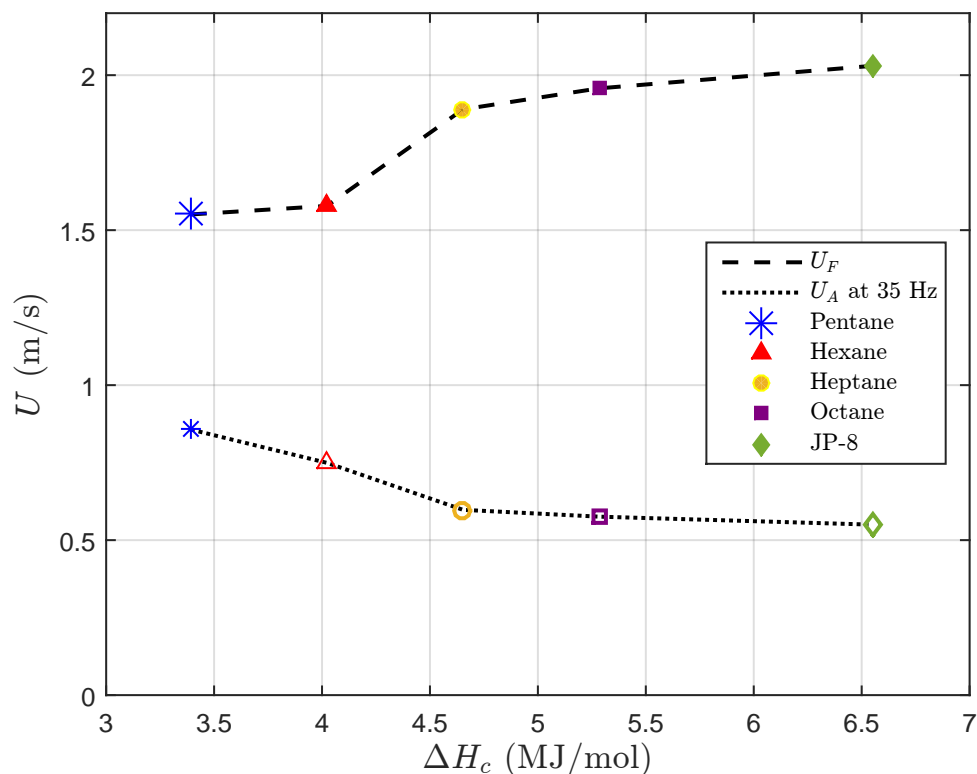


Figure 7.4: Comparison of acoustically induced and fan driven air flows at extinction. The values of  $U_{A_{ext}}$  at 35 Hz and  $U_{F_{ext}}$  are plotted against  $\Delta H_c$  for all fuels tested. Values of  $U_{F_{ext}}$  are seen to increase with  $\Delta H_c$  while values of  $U_{A_{ext}}$  are seen to decrease.

extinction experiments in this study are, therefore, similar to flames in a forced flow over a stagnant fuel film, which were studied by Emmons. In his analysis, Emmons showed that the flame existed in the boundary layer of the flow, and that it separated the region of cooler air from the fuel bed. As the free-stream velocity of the flow increased, the strain rate of the flow increased, the boundary layer thickness decreased, and the flame was forced closer to the fuel. Extinction occurred when the free-stream velocity and corresponding strain rate became so great that chemical kinetics could not compete with the mixing rate of the reactants, and the value of  $Da$  dropped below a critical value. However, so long as combustion

chemistry was occurring, the flame existed within the boundary layer of the flow [44, 45].

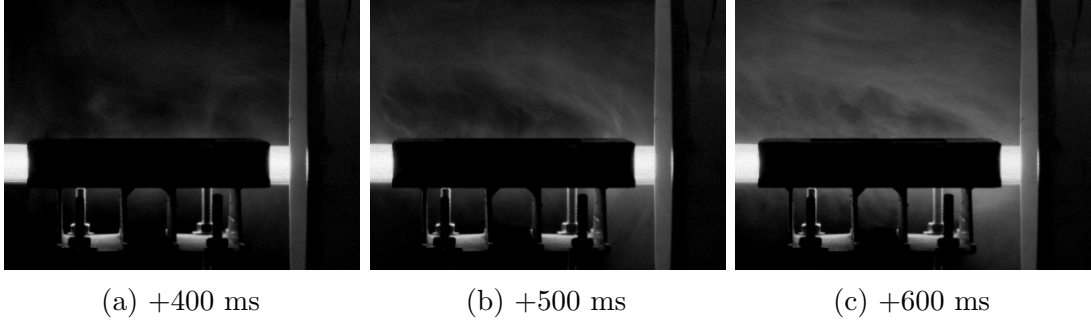


Figure 7.5: Visualization of the fan-driven flow over the burner with  $U_F = 1.6$  m/s. The times noted are from when the fan was activated. A boundary layer can clearly be seen forming over the burner as the flow develops.

Won *et al.* showed that the extinction strain rate ( $a_E$ ) for diffusion flames fueled by large hydrocarbons scales as:

$$a_E \propto [\mathcal{D}_F Y_{F,-\infty} \Delta H_c] [Kinetic Term] \quad (7.1)$$

where  $\mathcal{D}_F$  is the diffusivity of the fuel into air, and  $Y_{F,-\infty}$  is the fuel-mass fraction on the fuel side of the reaction zone [9]. For the combustion of an alkane though, the number of moles of the heavier species in the mixture (e.g.  $\text{CO}_2$  and  $\text{N}_2$ ) all scale approximately with the number of carbon atoms in the fuel. In addition, the fuel's molar mass also scales roughly with the number of carbon atoms. It can be expected, therefore, that  $Y_F$  was roughly constant for all the fuels tested. In addition, values of  $\mathcal{D}_F$  and the kinetic term should all be approximately the same when compared among the fuels. It can be concluded then that as values of  $\Delta H_c$

for the fuels tested increased, the speed of the flow required to cause extinction should also have increased.

Examining the fan data points in Fig. (7.4), it is seen that  $U_{F_{ext}}$  does increase with  $\Delta H_c$ , as expected. In contrast, values of  $U_{A_{ext}}$  are seen to decrease with  $\Delta H_c$ . When this observation is coupled with the fact that  $\bar{U}_{A_{ext}}$  is significantly less than  $\bar{U}_{F_{ext}}$ , it suggests that flame stretch was not the cause of extinction in the acoustic experiments, and that an alternate mechanism needs to be found.

### 7.2.3 Heuristic Framework

Reexamining the plots of  $P_{A_{ext}}$  in Fig. (7.1a) and  $U_{A_{ext}}$  in Fig. (7.1b), there is a positive correlation between  $\omega$  with  $P_{A_{ext}}$  and  $U_{A_{ext}}$ . The amount of scatter though in  $P_{A_{ext}}$  (CV=0.29) is nearly twice the amount seen  $U_{A_{ext}}$  (CV=0.15). This would suggest that the acoustic extinctions were more closely linked to  $U_A$  than  $P_A$ . Since it is assumed that flame stretch was not the cause of extinction, it might be reasonable to conclude that convective cooling of the wick was a cause.

To understand how this process might work, a simplified model of the flame is utilized: fuel enters the flame region, reacts with the oxidizer, releases heat, a portion of that energy is fed back into the fuel source, which drives more fuel into the flame region. In this model, the propensity of the fuel to maintain this cycle is best described by the Spalding B Number, and a large disruption to this cycle would cause flame extinction.

Examining the image sequence presented in Fig. (7.6), it can be seen that as the acoustic wave propagates over the burner, it temporarily displaces the flame from the region above the wick. In contrast to the fan-driven flows, a boundary layer never has time to fully form in the acoustic scenario. This means that the flame is not confined to the region directly above the fuel, and that the fuel bed can be exposed directly to cool air. It can be assumed that during the flame's displacement period, not only is the amount of heat feedback to the wick inhibited, but that the exposed wick also experiences convective cooling from the acoustic flow. From stagnant layer theory it is known that as the heat flux from the flame into the fuel bed decreases, so too will the fuel's mass loss rate ( $\dot{m}''$ ) [17]. Furthermore, according to the fire point theory described by Rashbash, there is a critical mass flux ( $\dot{m}''_{cr}$ ) for any given fuel below which total flame extinction will occur [46, 47]. It would be reasonable to conclude then that convective cooling of the fuel bed during the flame's displacement was creating conditions where  $\dot{m}'' < \dot{m}''_{cr}$ . Assuming this is true, a local Nusselt number ( $Nu_\xi$ ) could be used to characterize the magnitude of this cooling.

#### **7.2.4 Proposed Extinction Criterion**

In the model proposed, the B Number characterizes the fuel's ability to maintain the flame-fuel cycle, and the Nusselt Number characterizes the amount of disruption to this cycle. A ratio of these two non-dimensional numbers might then constitute a criterion by which acoustic extinctions can be predicted. For consistency with

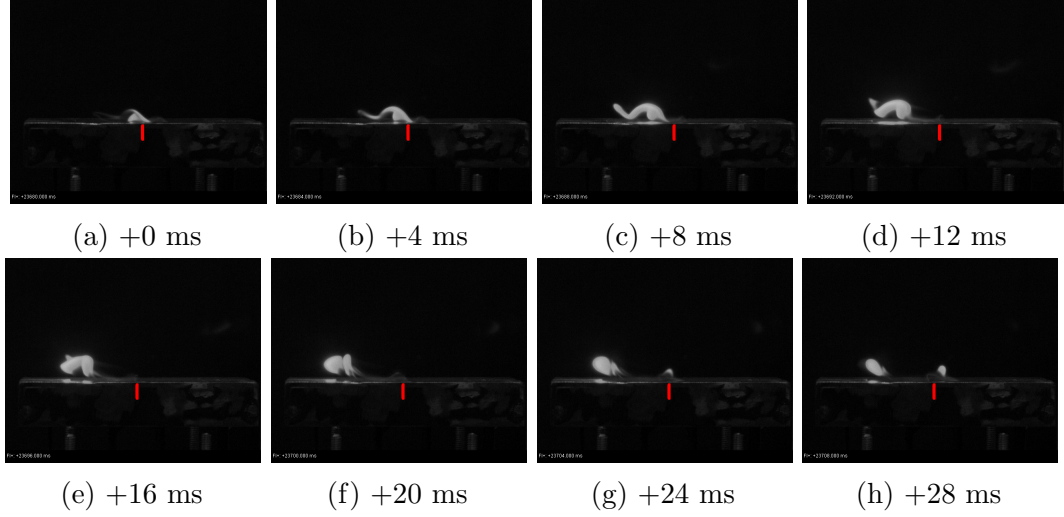


Figure 7.6: Hexane Flame at 35 Hz, just prior to extinction. The sequence shows the flame through one acoustic period ( $T = 0.0286$  s). The flame begins over the fuel region, which is indicated by the red marker, and is displaced as the acoustic wave propagates over the flame holder. From Frames (7.6d) to (7.6f), the flame is completely displaced from the fuel region. In Frame (7.6g) a flame reemerges over the fuel bed, and in Frame (7.6h) the process starts over.

the boundary maps shown in Fig. (7.2), it would be useful to structure this ratio so that larger values correspond with flame extinction, while smaller values correspond with continued burning. It is, therefore, proposed that the ratio of  $Nu_\xi$  to  $B$  at the point acoustic extinction was achieved is a constant, and that it that forms a boundary delineating conditions where the flame can and cannot exist. This ratio shall be called  $\Theta_A$ , as shown in Eq. (7.2).

$$\Theta_A = \frac{Nu_\xi}{B} \tag{7.2}$$

Expressions for the terms in Eq. (7.2) shall be developed in the following sections.

## 7.3 B - Mass Transfer Number

In a study of ethanol and heptane pool fires of various areas with varying crosswinds, Hu *et al* found that the ratio of radiation absorbed by the fuel to the heat needed for vaporization ( $\chi_a$ ) decreased as the fuel area decreased and the crosswind increased [48]. For their smallest heptane pool fire, which had an area of 10 cm<sup>2</sup>, they found  $\chi_a = 0.26$  with no crosswind and  $\chi_a = 0.10$  with a cross flow of 0.7 m/s. In the experiments for this study the burner area was 2.5 cm<sup>2</sup> and  $\bar{U}_A = 0.68$  m/s. Although the setup and testing conditions for this study were not perfectly analogous to Hu's, it can be assumed — based on their results and general trends seen in their data — that the flames in this study were driven primarily by convective heat transfer. With this assumption, Quintiere gives the B number as [17]:

$$B = \frac{Y_{O_2,\infty}(\Delta h_c/r) - c_{p,air}(T_b - T_\infty)}{L} \quad (7.3)$$

where it is assumed that  $Y_{O_2,\infty} = 0.233$  and  $T_\infty = 298$  K.

### 7.3.1 Fuel Specific Parameters

For the alkanes tested and certain gases of interest, data on the following parameters was obtained from NIST Chemistry Web-Book [49], and the values are reproduced in Tab. (7.3):

- Molar Mass ( $M$ )
- Liquid Specific Heat at 300 K ( $c_{p,liq}$ )
- Liquid Heat of Formation ( $\Delta h_{f,liq}^\circ$ )
- Gaseous Heat of Formation ( $\Delta h_{f,g}^\circ$ )
- Heat of Vaporization ( $h_v$ )
- Boiling Temperature at 1 atm ( $T_b$ )

Since JP-8 is distilled from crude oil it is not a “pure” substance, and its properties are not as well defined. The values needed were, therefore, amalgamated from a multitude of sources and are listed below. The results, where appropriate, are also presented in Tab.’s (7.3) and (7.5).

- The molecular formula of JP-8 was approximated as  $C_{11}H_{21}$  [50, 51], from which the molar mass was estimated to be  $M = 1.53 \times 10^{-1}$  kg/mol.
- NIST gives the vapor rising temperature of JP-8 to be 182.8°C, and this is considered to be the initial boiling temperature [52]. The boiling temperature was therefore estimated as  $T_b = 456$  K.
- The specific heat of liquid JP-8 can be approximated from its temperature as [52]:

$$c_p(T) = (2.193 \pm 0.0055) + (3.996 \pm 0.0011) \times 10^{-3}(T - 363.15) \quad (7.4)$$

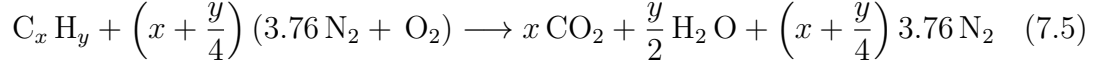
Using Eq. 7.4, the specific heat of JP-8 was evaluated at  $\frac{1}{2}(T_b + T_\infty) = 378$  K, and found to be  $c_{p,liq} = 2252$  J/(kg·K).

- Using data from the Defense Technical Information Center [53], the heat of vaporization for JP-8 at  $T = 456$  K was estimated to be  $h_v = (2.85 \pm 0.25) \times 10^5$  J/kg.

Table 7.3: Selected Properties of Fuels and Gases

Species	$M$ $\times 10^{-2}$ kg·mol <sup>-1</sup>	$c_{p,liq}$ J·(kg·K) <sup>-1</sup>	$\Delta h_{f,liq}^\circ$ at 298 K $\times 10^6$ J·kg <sup>-1</sup>	$\Delta h_{f,g}^\circ$ $\times 10^6$ J·kg <sup>-1</sup>	$h_v$ $\times 10^5$ J·kg <sup>-1</sup>	$T_b$ K
Pentane	7.215	2317	2.405 ± 0.008	2.035 ± 0.008	3.673 ± 0.083	309.2 ± 0.2
Hexane	8.612	2269	2.306 ± 0.008	1.940 ± 0.009	3.597 ± 0.116	341.9 ± 0.3
Heptane	10.02	2242	2.239 ± 0.008	1.874 ± 0.008	3.593 ± 0.299	371.5 ± 0.3
Octane	11.42	2230	2.191 ± 0.016	1.824 ± 0.006	3.589 ± 0.350	398.7 ± 0.5
JP-8	15.33	2252	N/A	N/A	2.85 ± 0.25	456
CO <sub>2</sub>	4.401	N/A	N/A	8.941 ± 0.003	N/A	N/A
H <sub>2</sub> O	1.802	N/A	N/A	13.42 ± 0.002	N/A	N/A
O <sub>2</sub>	3.200	N/A	N/A	0	N/A	N/A

Using the data presented in Tab. (7.3), and assuming complete combustion in air at stoichiometric conditions, as shown in Eq. (7.5), the mass ratio of oxygen to fuel ( $r$ ), latent heat of vaporization ( $L$ ), and heat of combustion per unit mass ( $\Delta h_c$ ) were calculated as follows, and the results are summarized in Tab. (7.5):



$$r = \frac{\left(x + \frac{y}{4}\right) M_{O_2}}{M_{C_x H_y}} \quad (7.6)$$

$$L = h_v + c_{p,liq}(T_b - T_\infty) \quad (7.7)$$

$$\Delta h_c = x \Delta h_{f,CO_2}^\circ \frac{M_{CO_2}}{M_{C_x H_y}} + \frac{y}{2} \Delta h_{f,H_2O}^\circ \frac{M_{H_2O}}{M_{C_x H_y}} - \Delta h_{f,C_x H_y}^\circ \quad (7.8)$$

It was assumed that  $T_\infty = 298$  K in Eq. (7.7) and that water remained in a gaseous state in Eq. (7.8). For JP-8, the value of  $\Delta h_c$  is given by multiple sources as  $\Delta h_c = 42.8 \times 10^6$  J/kg [51, 53–55] The uncertainties in  $\Delta h_c$  ( $S_{\Delta h_c}$ ) are discussed in Sec. (A.2)

### 7.3.2 Air Properties

Air properties were interpolated from data presented by Turns in *An Introduction to Combustion* [19]. For each fuel tested, the heat capacity of air was evaluated at  $\frac{1}{2}(T_b + T_\infty)$ , while the kinematic viscosity ( $\nu$ ) and Prandtl (Pr) number of air were evaluated at  $T_b$ . The results are presented in Tab. (7.4).

Table 7.4: Selected Properties of Air for Different Fuels

Fuel	$T_b$ K	$c_{p, air}$ $J \cdot (kg \cdot K)^{-1}$	$\nu$ $\times 10^{-5}$ $m^2 \cdot s^{-1}$	Pr
Pentane	309.2	1007	1.68	0.706
Hexane	341.9	1008	2.01	0.701
Heptane	371.5	1008	2.33	0.696
Octane	398.7	1009	2.63	0.690
JP-8	456	1012	3.16	0.686

### 7.3.3 B Number Calculation

Using the data in Tab.'s (7.3), and (7.4) and the formulas in Eq.'s (7.6) through (7.8), the values of the B-Mass Transfer Number were calculated and the results are summarized in Tab. (7.5). The calculated values of B agreed reasonably well with values presented in other sources [17, 53, 56].

Table 7.5: Calculated Fuel Properties

Fuel	$r$	$L \times 10^5$ $J \cdot kg^{-1}$	$\Delta h_c \times 10^6$ $J \cdot kg^{-1}$	B
Pentane	3.55	3.933	$45.35 \pm 0.01$	7.54
Hexane	3.53	4.593	$45.10 \pm 0.01$	6.39
Heptane	3.51	5.241	$44.92 \pm 0.01$	5.54
Octane	3.50	5.835	$44.79 \pm 0.01$	4.93
JP-8	3.40	6.21	$42.80 \pm 0.18$	4.49

## 7.4 Nusselt Number Correlation

### 7.4.1 Reynolds Number

Nusselt number correlations are based on the assumption that convective heat transfer in a boundary layer scales with momentum transfer [57, 58]. Therefore, a Reynolds Number (Re) had to be found, which in turn required a characteristic length ( $\ell$ ) to be defined. Since it was established that  $U_A$  was an *rms* flow velocity in Sec. (4.5.1),  $\ell$  was defined as the *rms* displacement distance of a particle in an acoustic cycle, and calculated as:

$$\ell = \frac{U_A}{\omega} \tag{7.9}$$

Using Eq. (7.9), the Reynolds number was then calculated as:

$$\text{Re}_A = \frac{U_A \ell}{\nu} = \frac{U_A^2}{\nu \omega} \tag{7.10}$$

### 7.4.2 Mathematical Formulation

Nusselt number correlations are not well studied for oscillating flows [59]. It was still necessary to characterize the ratio of convective to conductive heat transfer at the wick's surface, and it was assumed that a functional correlation existed which

linked a local Nusselt number at the flame position ( $Nu_\xi$ ) with the Reynolds and Prandtl numbers:

$$Nu_\xi = f(\text{Re}, \text{Pr}) \quad (7.11)$$

Using the analogy of a non-oscillating flow over a flat plate, it was assumed Eq. (7.11) took the form [57, 58]:

$$Nu_\xi = c \text{Re}^\gamma \text{Pr}^\delta \quad (7.12)$$

where  $c$ ,  $\gamma$ , and  $\delta$  are determined empirically.

### 7.4.3 Modified Nusselt Number

The values of the Prandtl numbers to be used in Eq. (7.12) were taken from Tab. (7.4) and were practically constant for all tests ( $\overline{\text{Pr}} = 0.70$ ,  $\sigma_{\text{Pr}} = 0.7 \times 10^{-2}$ ).

Since  $c$  is also a constant, Eq. (7.12) was rewritten as:

$$Nu_\xi = C \text{Re}_A^\gamma \quad (7.13)$$

where  $C = c \text{Pr}^\delta$ . If  $Nu'$  is defined as  $Nu' = Nu_\xi / C$ , then Eq. (7.13) can be further simplified as:

$$\text{Nu}' = \text{Re}_A^\gamma \tag{7.14}$$

Finally, substituting Eq. (7.14) into Eq. (7.2) yields:

$$\Theta'_A = \frac{\text{Re}_A^\gamma}{\text{B}} \tag{7.15}$$

#### **7.4.4 Exponent of Best Fit**

The value of  $\gamma$  in Eq. (7.15) was chosen to optimize the results of  $\Theta'_A$ . To find this value, a MATLAB script was written that calculated the values of  $\Theta'_A$  and the corresponding CV's of the data for  $-3 \leq \gamma \leq 3$ . The value of  $\gamma$  where the CV was minimized would then indicate the exponent in Eq. (7.15) that produced the least amount of scatter in values of  $\Theta'_A$ . The results from this script are shown in Fig. (7.7), and the minimum occurred at  $\gamma = 1/3$ . It should be noted though that most Nusselt Number correlations for forced convection over a plate scale by  $\text{Re}^{1/2}$  [57, 58].

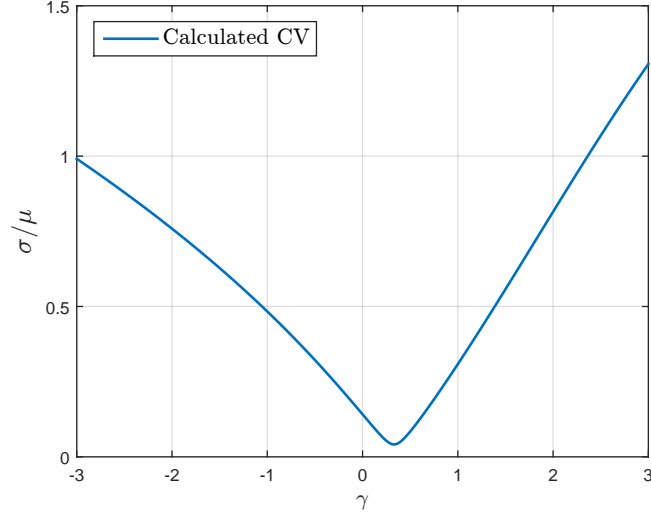


Figure 7.7: Coefficients of Variation for  $\Theta'_A$  with varying values of  $x$ . The minimum occurs at  $\gamma = 1/3$ , where  $CV_{\Theta'_A} = 0.043$ .

## 7.5 Calculated Values of $\Theta'$

### 7.5.1 Acoustic Results

Using the results from Sec. (7.4.4), Eq. (7.15) becomes:

$$\Theta'_A = \frac{\text{Re}_A^{1/3}}{B} = \frac{U_A^{2/3}}{(\nu\omega)^{1/3}B} \quad (7.16)$$

Applying the model described by Eq. (7.16) to the acoustic extinction data set yields highly consistent results with  $\overline{\Theta}'_{A_{ext}} = 1.4$ ,  $\sigma_{\Theta'_A} = 0.059$ , and  $CV_{\Theta'_A} = 0.043$ .

The results, including uncertainties, are shown in Fig. (7.8); the uncertainties are discussed in Appendix (A.2.2). When the scatter in  $\Theta'_A$  is compared to that of  $U_{A_{ext}}$  ( $CV_{U_A} = 0.15$ ) and  $P_A$  ( $CV_{P_A} = 0.29$ ), it becomes clear that  $\Theta'_{A_{ext}}$  is a much

more consistent descriptor of conditions at extinction than either  $U_{A_{ext}}$  or  $P_{A_{ext}}$ . Furthermore, since  $\Theta'_{A_{ext}}$  was calculated from conditions created by the lowest speaker power that could consistently cause extinction, it is proposed that  $\bar{\Theta}'_{A_{ext}}$  constitutes a critical value, below which the flame continues to burn and above which total flame extinction occurs.

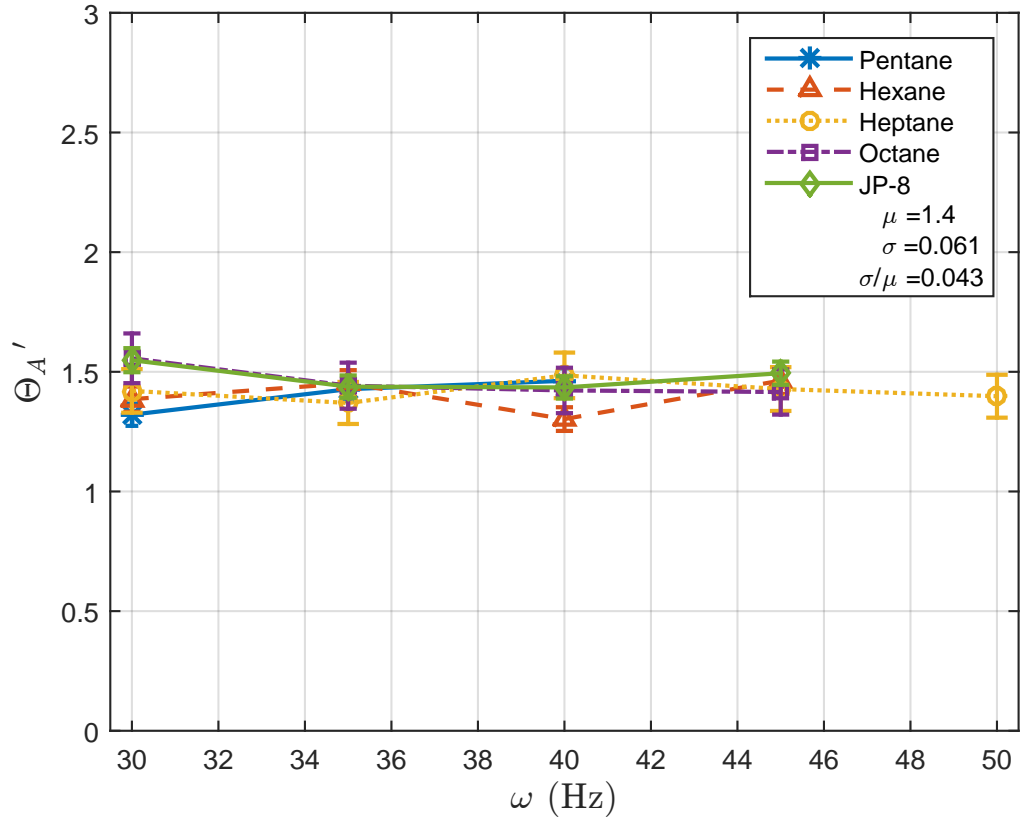


Figure 7.8: Calculated values for  $\Theta'_{A_{ext}}$ , based on conditions at the lowest speaker power that could consistently cause total flame extinction. The model shows significantly less scatter than either  $U_{A_{ext}}$  or  $P_{A_{ext}}$ .

### 7.5.2 Hypo and Hyper Critical Values

To test whether  $\bar{\Theta}'_{A_{ext}}$  constitutes a critical value for predicting extinction, values of  $\Theta'$  had to be calculated for conditions above and below the minimum speaker power

required to cause flame extinction. Within the total data set, there existed several instances where sufficient data was collected (i.e., 3 or more trials) at speaker powers other than the minimum power required to cause extinction. From these data points, values of  $\Theta'_A$  could be calculated using Eq. (7.16). The extinction results from these trials, along with the calculated values of  $\Theta'_A$  and the uncertainties are presented in Tab. (7.6).

Table 7.6: Analysis of Hypo and Hyper Critical Extinction Conditions

Fuel	$\omega$ (Hz)	$U_A$ (m·s <sup>-1</sup> )	Extinction	$\Theta'_A$	$S_{\Theta'_A}$
Pentane	30	0.61	No	1.20	0.04
Hexane	30	0.52	No	1.20	0.06
Hexane	35	0.69	No	1.38	0.05
Heptane	30	0.48	No	1.25	0.09
Heptane	35	0.53	No	1.26	0.08
Heptane	45	0.69	No	1.38	0.09
Octane	30	0.50	No	1.38	0.09
Pentane	30	0.77	Yes	1.41	0.05
Heptane	45	0.86	Yes	1.60	0.10
Heptane	50	0.78	Yes	1.45	0.09
JP-8	40	0.64	Yes	1.51	0.05

According to the theory presented,  $\bar{\Theta}'_{A_{ext}}$  constitutes a critical value below which the flame can continue to burn and above which flame extinction occurs. When the values of  $\Theta'_A$  from Tab. (7.6) are plotted, as shown in Fig. (7.9), it is seen that  $\bar{\Theta}'_{A_{ext}}$  does in fact form a boundary between flammability and extinction. For those trials where extinction did not occur and which are indicated by green markers, values of  $\Theta'_A$  were less than  $\bar{\Theta}'_{A_{ext}}$ . For those trials where extinction did occur above the minimum speaker power and which are indicated by red markers,  $\Theta'_A$

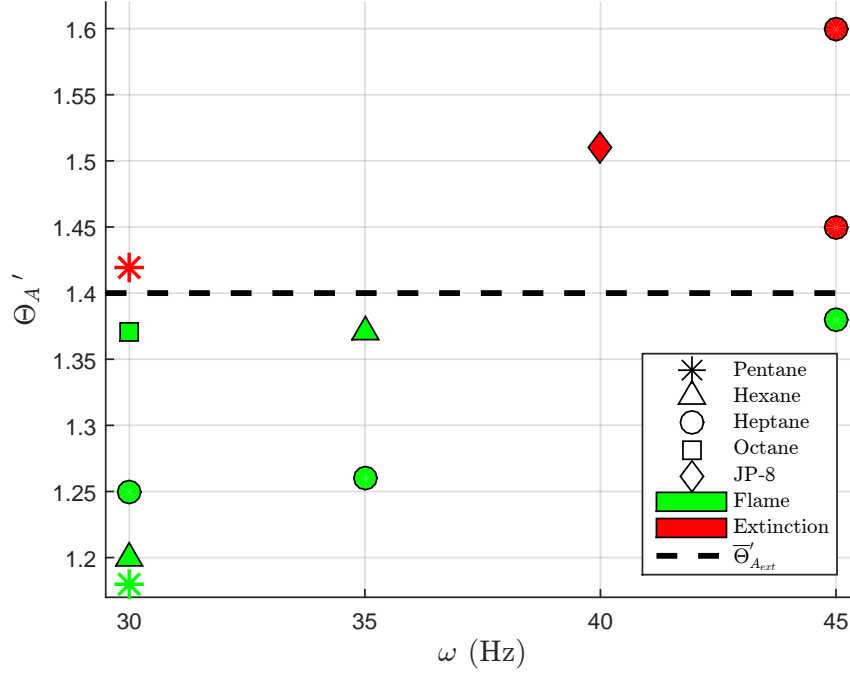


Figure 7.9: Calculated values of  $\Theta'_A$  for hypo and hyper critical data points. Trails where extinction was not achieved are indicated by green markers and trials where extinction was achieved are indicated by red markers. Values of  $\Theta'_A < \bar{\Theta}'_{A_{ext}}$  correspond uniquely with continued burning, while values of  $\Theta'_A > \bar{\Theta}'_{A_{ext}}$  correspond uniquely with extinction.

was greater than  $\bar{\Theta}'_{A_{ext}}$ . The errors bars in  $\Theta'_A$  have been omitted from Fig. (7.9) for clarity.

### 7.5.3 Fan Driven Results

To test if the model for  $\Theta'_A$  was unique to the acoustically-driven extinction events, the model was also applied to the fan-driven extinctions. In this analysis though,  $\ell$  was taken to be the distance from windward edge of the flame holder to the center of the fuel bed, which was 0.067 m. The Reynolds number was then calculated as:

$$\text{Re}_F = \frac{U_F \ell}{\nu} \quad (7.17)$$

The ratio of the modified Nusselt number to B number for the fan-driven flows ( $\Theta'_F$ ) was calculated as:

$$\Theta'_F = \frac{(U_F \ell / \nu)^{1/3}}{B} \quad (7.18)$$

The calculated values of  $\Theta'_F$  at extinction ( $\Theta'_{F_{ext}}$ ), including the uncertainties, are plotted in Fig. (7.10); the uncertainties are discussed in Appendix (A.2.3). In contrast to the acoustic results presented in Sec. (7.5.1), the values of  $\Theta'_{F_{ext}}$  showed slightly increased scatter ( $\text{CV}_{\Theta'_F} = 0.14$ ) when compared to that seen in  $U_{F_{ext}}$  ( $\text{CV}_{U_F} = 0.10$ ). This indicates that  $\Theta'_F$  is a less consistent descriptor of conditions at extinction, and that the proposed model does not explain the fan driven extinction results.

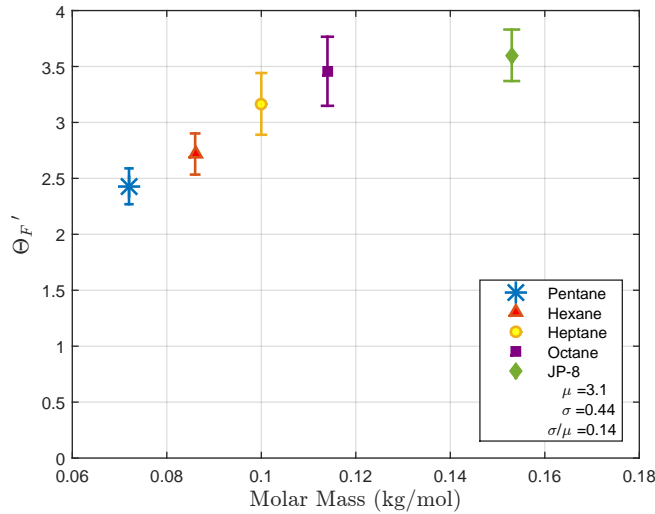


Figure 7.10: Calculated values of  $\Theta'_F$  for fan driven extinction events. The model shows slightly more scatter than  $U_F$ .

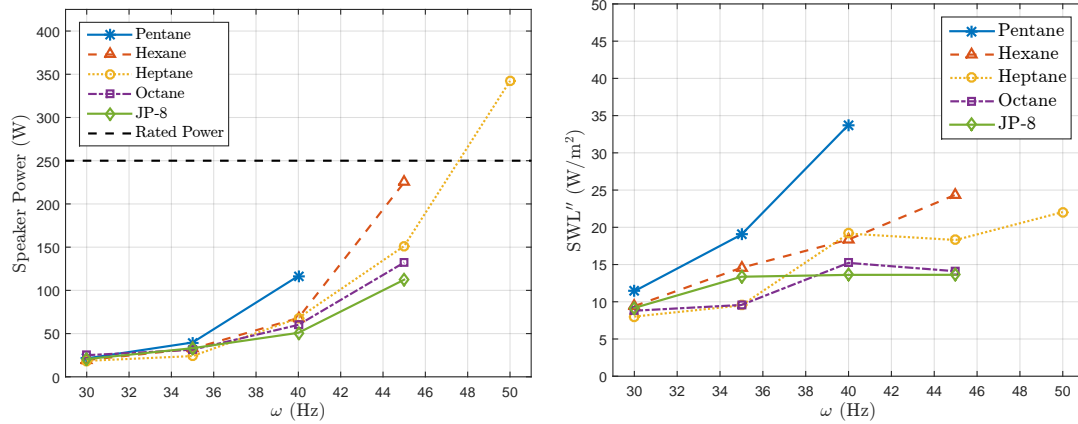
## 7.6 Limitations and Considerations

### 7.6.1 System Limitations

The performance characteristics of the speaker used for this study posed significant limitations on the range of frequencies and acoustic pressures that could be tested. The speaker had a rated power of 250 W, and as seen in Fig. (7.11a), this operating limit was quickly reached. In fact, the one test series shown in Fig. (7.11a) that occurred above 250 W caused irreversible damage to the speaker, which required it to be replaced. The actual acoustic power per unit area (SWL'') of the waves produced was calculated using Eq. (7.19) [37], and those results are presented in Fig. (7.11b).

$$\text{SWL}'' = P_A U_A \quad (7.19)$$

When the ratio of SWL'' to speaker power is taken, as shown in Fig. (7.12), it becomes apparent that as the frequency was increased, there was a “diminishing return” on the power of the acoustics generated. If the speaker had been rated for a higher power, acoustic extinction of the flames could likely have been achieved at higher frequencies. This supposition is consistent with the findings of Whiteside, who concluded that acoustic extinction could be achieved at any frequency, provided that a critical acoustic velocity could be achieved [4].



(a) Speaker power required to cause acoustic extinction. The black line indicates the rated power of the speaker.

(b) Sound Power Level per unit area (SWL'') of the acoustic waves produced at the minimum speaker power required to cause extinction.

Figure 7.11: Comparison of the power required by the speaker and power of the acoustic wave generated at extinction.

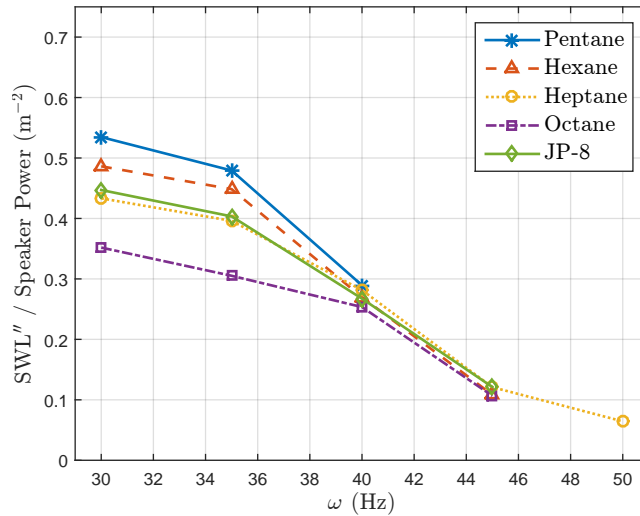


Figure 7.12: Ratio of SWL'' to speaker power. As the frequency was increased the ratio was seen to decrease

### 7.6.2 Considerations of Applicability

When compared to other flame suppression techniques, the concept of acoustic flame suppression has several unique advantages. Chief among these advantages

is that there is no flame suppressing agent which needs to be applied. For fire protection scenarios where there are sensitive mechanical and electrical systems, this feature is especially desirable. It would therefore be beneficial to consider whether this technique could be applied to fires larger than the ones used for the study. To do so, a heptane pool fire whose diameter ( $D$ ) is 1 m was considered, and the speaker size required to control this fire was be estimated.

According to the model developed, acoustic flame extinction requires the oscillatory movement of air to be sufficiently fast that convective cooling prevents enough fuel from being liberated to sustain the flame. Although heat transfer in a pool fire of this size is dominated by radiation [17, 19, 60], for the purposes of scaling it was assumed that convection was still the primary mode of heat transfer. Another key consideration to explore though is the observation of McKinney and Dunn-Rankin, who found that acoustic extinction of droplet flames required the flame to be displaced by at least the droplet's radius [23]. When the ratio of  $\ell$  to the burner width ( $w_b$ ) was taken for the extinction data in Tab. (7.1) – the results of which are shown in Fig. (7.13) – its average was found to be 3.66.

With these considerations in mind, an *a priori* analysis would indicate that for a pool fire,  $\ell/D \geq 1$ . Taking this ratio at it's minimum, it was assumed that  $\ell \approx D$ . Using Eq. (7.9), the acoustic velocity required for extinction was calculated as:

$$U_A = \omega D \tag{7.20}$$

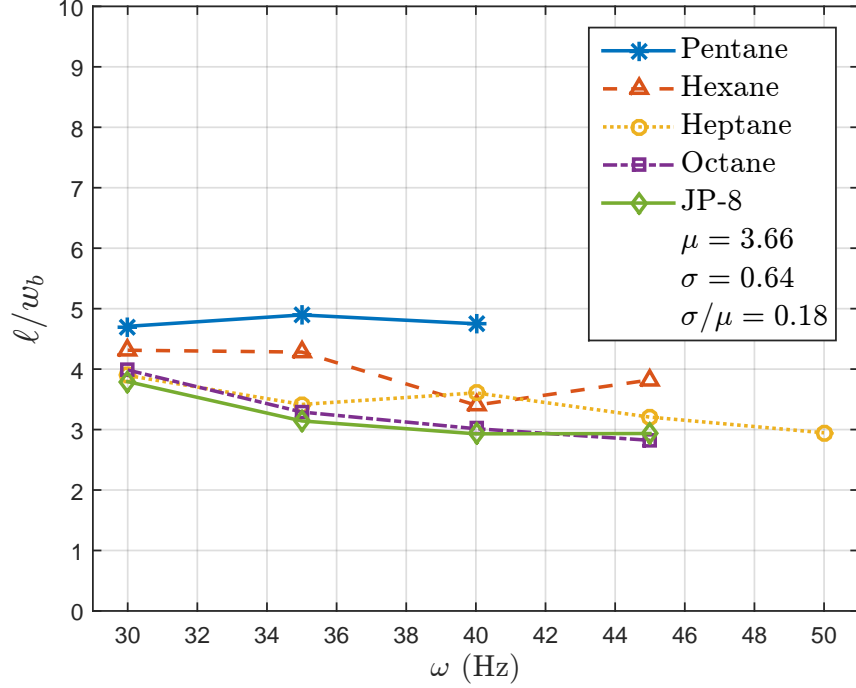


Figure 7.13: Ratio of *rms* displacement distance ( $\ell$ ) to the burner width ( $w_b$ ).

Reexamining Fig. (7.12), it can be seen that the lower the frequency, the more efficiently the speaker produced acoustics. Assuming this trend is true for any speaker, 30 Hz was used for the scaling since it is the lowest frequency known to cause acoustic extinction. Evaluating Eq. (7.20) with  $\omega = 30$  Hz and  $D = 1$  m, a value of  $U_A = 30$  m/s was calculated. When these values are then used in Eq. (7.16) along with the appropriate values for  $\nu$  and B, it was found that  $\Theta_{A_{pool}} = 19.6$ . Recalling the results from Sec.'s (7.5.1) and (7.5.2), and assuming that  $\bar{\Theta}'_{A_{ext}} = 1.4$  is a universal extinction constant, it was concluded that an *rms* air speed of 30 m/s at a frequency of 30 Hz could extinguish a heptane pool fire 1 m in diameter.

To estimate the size the speaker though an estimate of the acoustic pressure was required. Such an estimate was made by using the characteristic specific acoustic

impedance of air ( $Z_o$ ) at 298 K, which is given as  $410 \text{ Pa}\cdot\text{s}\cdot\text{m}^{-1}$  [37]. The acoustic pressure was then calculated as:

$$\begin{aligned} P_A &= U_A z_o \\ &= 1.23 \times 10^4 \text{ kPa} \end{aligned} \tag{7.21}$$

Using Eq. (3.1), it was found that  $1.23 \times 10^4 \text{ kPa} = 144 \text{ dB}$ . Commercially available sub-woofers generally produce acoustics no louder than 110 dB at 1 m [61]. It is possible, though, to produce low frequency acoustics at higher pressures. In 1996 ARL studied the use of “weaponized” acoustics at 20 Hz and 165 dB [62]. Given that the calculated acoustic pressure to control the pool fire is  $4 \times$  larger than a “weaponized” acoustic pressure generated with specialty equipment, the use of acoustics alone to suppress this fire would be highly impractical.

The fact that acoustics alone would not be suitable for controlling larger fires should not necessarily preclude development of the technology. Even if flame extinction can't be achieved with acoustics alone, acoustics can certainly be used to destabilize the flame and even force it to become detached. If the acoustics were coupled with a known suppressing agent (e.g., water mist, dry-chem,  $\text{CO}_2$ ), the combination of flame destabilization, increased mixing, and delivery of the agent directly to the fuel bed could prove to be an efficient means of fire suppression.

# Chapter 8

## Conclusions

A burner and testing apparatus were constructed to study the interaction of acoustic waves with a laminar flame produced with various liquid fuels. The fuels used in the study were the alkanes n-pentane through n-octane and JP-8. The burner was designed to produce a line-flame which approximated a flame sheet. To produce the line-flame, fuel-laden wicks were placed under panes of borosilicate glass, leaving only a  $5.0 \times 10^{-2} \text{ m} \times 5.0 \times 10^{-3} \text{ m}$  gap through which fuel could escape. The testing apparatus itself consisted of a 0.25 m diameter, 3.05 m long PVC tube with the burner placed at one end and a sub-woofer mounted inside the tube at the other end.

Acoustics were produced at frequencies of 30-50 Hz and at acoustic pressures of 5-50 Pa. Measurements of the pressures inside the tube showed that the system achieved resonance at frequencies consistent with theory. Measurements of the

pressures outside the tube showed a linearly proportional decay as distance from the tube opening increased. Also of interest were the air movements within the enclosure which were induced by the acoustics. Measurements of air movement were made with a hot-wire anemometer, and PIV analysis showed that the quantity being measured was the *rms* speed of the oscillatory air movement.

Prior to the acoustic testing with a flame, studies of the alkane flames' unperturbed burning rate, flame height, and flame width were conducted. To collect this data, the burner was placed on a mass balance, the fuels were ignited, and the flames were allowed to evolve while the process was simultaneously recorded via videography. Mass loss rates were then evaluated from the temporally indexed mass readings of the balance, and flame heights were evaluated from the temporally and spatially indexed pixel intensities of the videography. Estimates of the flame's width were made from direct measurements of the flame's width in the video image. Using each fuel's heat of combustion, a direct comparison was made between each flame's height and heat release rate per unit flame width. A linear relationship was observed between these quantities, which is consistent with the Burke-Schumann model.

To more thoroughly understand the effects of the acoustics on the flame, a study of flame's burning rate under acoustic excitation was performed. Samples of hexane were ignited and allowed to evolve until burnout under various combinations of acoustic frequency and pressure, during which mass readings were recorded. Since the acoustics induced air movements, which the flame was sensitive to, mlr profiles

using a fan at various air speeds were also generated for comparison. It was found that the acoustic and fan flows only affected the flame during the growth phase. Once peak mlr was achieved, all profiles converged towards the free burn profile. A comparison of mlr profiles at differing frequencies and comparable acoustic pressures revealed no obvious trends. A comparison of mlr profiles at differing frequencies and comparable *rms* air speeds were found to be very similar. In addition, there was a strong correlation between average mlr and *rms* air speed at all frequencies. These observations indicated that it was the effects of the oscillatory air movement which influenced the flame, and that frequency and acoustic pressure influenced the flame's burning rate only insofar as they influenced oscillatory movement of air. It is believed that the observed increase in burning rate was due to the flame being forced closer to the fuel surface, which enhanced heat transfer into the fuel bed.

Finally, a study of acoustically-driven extinction was carried out using the alkanes and JP-8. Samples were ignited and then subjected to acoustic perturbations at various frequencies and speaker powers until the minimum speaker power was found that could cause three consecutive flame extinctions. The acoustic pressure and *rms* air speeds were measured during each trial and, along with frequency, these measurements were used to characterize the acoustic conditions. The minimum fan driven flows required to cause extinction for each fuel was also evaluated. Analysis of the data showed that the fan-driven air speed required to cause acoustic extinction of each fuel increased with the fuel's heat of combustion per unit mole, and that this trend was consistent with extinction strain rate theory. Using acoustics though,

the *rms* air speed at extinction was seen to decrease, which indicated that flame stretch was not the cause of extinction using acoustics.

High speed video showed that during acoustic excitation, the flame would become detached, forced away from the fuel bed, and then returned and reattached until the next cycle. It was theorized that during this displacement phase the fuel bed experienced convective cooling, and that this eventually caused the fuel's *mlr* to fall below the critical amount needed to sustain the flame. This hypothesis was consistent with that developed by other authors to explain the acoustically driven extinction of droplet flames. To explore this hypothesis, the flame was conceptualized in a simple model between flame and fuel source. In this model, the Spalding B Number was used to characterize the interplay between the flame and fuel, and a Nusselt Number was used to characterize the convective cooling of the fuel bed. Mathematical expressions were then developed for each of the numbers and they were evaluated using values reported in the literature and conditions measured during experiment.

It was found that at the minimum speaker power required to cause extinction, the ratio of the Nusselt Number to B Number was a constant for all fuels at all frequencies tested. It was found that when this ratio was below the constant, the flame continued to burn. If the ratio was greater than or equal to the constant, then flame extinction occurred. It was therefore asserted that this constant constituted a boundary between regions of flammability and flame extinction.

# Appendix A

## Error Analysis

### A.1 Data Uncertainties

Since the data points for each extinction event were only calculated from three trials, there were an insufficient number of measurements to estimate the uncertainty directly. To overcome this, uncertainties were estimated from a larger data set, which included trials where either extinction was not achieved or extinction was achieved at speaker powers higher than the minimum required.

The analysis began with a selection of data subsets that contained three or more measurements of the system at homologous conditions (i.e., the same frequency and speaker power). A total of 17 subsets ( $N_S$ ) were used, with each subset containing

three to five trials ( $N_i$ ). Amongst all data subsets there were a total of 53 trials ( $N_T$ ), and the data was structured as shown in Tab. (A.1).

Table A.1: Uncertainty Analysis Data Structure

Data Subset	Trial	$P_A$	$U_A$
1	1	$P_{A11}$	$U_{A11}$
	2	$P_{A12}$	$U_{A12}$
	3	$P_{A13}$	$U_{A13}$
2	1	$P_{A21}$	$U_{A21}$
	2	$P_{A22}$	$U_{A22}$
	3	$P_{A23}$	$U_{A23}$
	4	$P_{A24}$	$U_{A24}$
$\vdots$	$\vdots$	$\vdots$	$\vdots$
$i$	$j$	$P_{A_{ij}}$	$U_{A_{ij}}$

For each data subset, an average was calculated using Eq. (A.1). Each data point within the subset was then normalized by the average of that subset using Eq. (A.2).

$$\bar{X}_i = \frac{1}{N_i} \sum_{j=1}^{N_i} X_{ij} \quad (\text{A.1})$$

$$\hat{X}_{ij} = \frac{X_{ij}}{\bar{X}_i} \quad (\text{A.2})$$

An average of all normalized data points was then calculated by Eq. (A.3), and a relative standard deviation of these normalized data points was calculated by Eq. (A.4).

$$\tilde{X} = \frac{1}{N_T} \sum_{i=1}^{N_S} \sum_{j=1}^{N_i} \hat{X}_{ij} \quad (\text{A.3})$$

$$\sigma_{\hat{X}} = \sqrt{\frac{1}{N_T} \sum_{i=1}^{N_S} \sum_{j=1}^{N_i} (\hat{X}_{ij} - \tilde{X})^2} \quad (\text{A.4})$$

The relative standard deviations of the acoustic pressure and *rms* air speed were found to be  $\sigma_{\hat{P}_A} = 0.006$  and  $\sigma_{\hat{U}_A} = 0.035$ . The standard deviation of an extinction data point from Tab. (7.1) was then estimated as:

$$\sigma_X = \sigma_{\hat{X}} X \quad (\text{A.5})$$

On average, the individual extinction values of  $P_A$  were 1.04 standard deviations from the their subset average, and the individual extinction values of  $U_A$  were 0.60 standard deviations from the their subset average. With estimates for the standard deviations of each extinction data point, the uncertainties in the data from Tab. (7.1) were calculated as:

$$S_{P_A} = 2\sigma_{P_A}/\sqrt{N} \quad (\text{A.6})$$

$$S_{U_A} = 2\sigma_{U_A}/\sqrt{N} \quad (\text{A.7})$$

where  $N = 3$ . For the fan driven flows, it was assumed that  $\sigma_{\hat{U}_F} = \sigma_{\hat{U}_A}$ , and the uncertainties in the fan extinction data points were also estimated by Eq. (A.7). In addition to the random uncertainties within the bulk air speed measurements there was also systemic uncertainties from the anemometer, which are discussed further in Sec. (A.2.1).

## A.2 Fuel Parameter Uncertainties

Uncertainties in the values of  $\Delta h_c$  were calculated through an error propagation of Eq. (7.8), as shown in Eq. (A.8).

$$\begin{aligned}
 S_{\Delta h_c} &= \sqrt{\sum \left( \frac{\partial h_c}{\partial \Delta H_{f,i}} S_i \right)^2} \\
 &= \sqrt{\left( x \frac{M_{\text{CO}_2}}{M_{\text{C}_x\text{H}_y}} S_{\Delta H_{f,\text{CO}_2}^\circ} \right)^2 + \left( \frac{y}{2} \frac{M_{\text{H}_2\text{O}}}{M_{\text{C}_x\text{H}_y}} S_{\Delta H_{f,\text{H}_2\text{O}}^\circ} \right)^2 + \left( -S_{\Delta H_{f,\text{C}_x\text{H}_y}^\circ} \right)^2} \quad (\text{A.8})
 \end{aligned}$$

### A.2.1 Model Uncertainties

Estimates of the uncertainties in  $\Theta'_A$  and  $\Theta'_F$  were made through a modified error propagation of Eq.'s (7.16) and (7.18), respectively.

### A.2.2 Uncertainties in Acoustic Analysis

In its fully expanded form for the acoustic analysis, Eq. (7.16) is:

$$\Theta'_A = \frac{U_A^{2/3} [h_{fg} + c_{p,liq}(T_b - T_\infty)]}{(\nu\omega)^{1/3} [Y_{O_2,\infty}(\Delta h_c/r) - c_{p,air}(T_b - T_\infty)]} \quad (\text{A.9})$$

It is assumed that the main sources of error in Eq. (A.9) came from uncertainties in  $U_A$ ,  $h_v$ , and  $\Delta h_c$ . The error in  $\Theta'_A$  was, therefore, estimated as:

$$S_{\Theta'_A} = \sqrt{\underbrace{\left(\frac{\partial\Theta'_A}{\partial U_A} S_{U_A}\right)^2}_{\text{Term A1}} + \underbrace{\left(\frac{\partial\Theta'_A}{\partial h_{fg}} S_{h_{fg}}\right)^2}_{\text{Term A2}} + \underbrace{\left(\frac{\partial\Theta'_A}{\partial \Delta h_c} S_{\Delta h_c}\right)^2}_{\text{Term A3}}} + \underbrace{\frac{\partial\Theta'}{\partial U_A} S_{U_A,\text{Sys}}}_{\text{Term A1}} \quad (\text{A.10})$$

The final element of Eq. (A.10) represents the systemic uncertainty in the anemometer, which was given by the manufacturer as  $\pm 3\%$ . Each partial derivative indicated in Eq. (A.10) is shown below:

$$\text{Term A1:} \quad \frac{\partial \Theta'_A}{\partial U_A} = \frac{2\text{Re}_A^{1/3}}{3U_A B} \quad (\text{A.11})$$

$$\text{Term A2:} \quad \frac{\partial \Theta'_A}{\partial h_{fg}} = \frac{\text{Re}_A^{1/3}}{BL} \quad (\text{A.12})$$

$$\text{Term A3:} \quad \frac{\partial \Theta'_A}{\partial \Delta h_c} = \frac{-Y_{\text{O}_2, \infty} \text{Re}_A^{1/3}}{rB^2L} \quad (\text{A.13})$$

### A.2.3 Uncertainties in Fan Driven Analysis

In its fully expanded form for the fan driven analysis, Eq. (7.16) is:

$$\Theta'_F = \frac{(U_F \ell / \nu)^{1/3} [h_{fg} + c_{p, \text{liq}}(T_b - T_\infty)]}{[Y_{\text{O}_2, \infty}(\Delta h_c / r) - c_{p, \text{air}}(T_b - T_\infty)]} \quad (\text{A.14})$$

It is assumed that the main sources of error in Eq. (A.14) came from uncertainties in  $U_F$ ,  $h_v$ ,  $\Delta h_c$ , and  $\ell$ . The error in  $\Theta'_F$  was then estimated as:

$$S_{\Theta'_F} = \sqrt{\left( \underbrace{\frac{\partial \Theta'_F}{\partial U_F} S_{U_F}}_{\text{Term F1}} \right)^2 + \left( \underbrace{\frac{\partial \Theta'_F}{\partial h_{fg}} S_{h_{fg}}}_{\text{Term F2}} \right)^2 + \left( \underbrace{\frac{\partial \Theta'_F}{\partial \Delta h_c} S_{\Delta h_c}}_{\text{Term F3}} \right)^2 + \left( \underbrace{\frac{\partial \Theta'_F}{\partial \ell} S_\ell}_{\text{Term F4}} \right)^2} + \underbrace{\frac{\partial \Theta'_F}{\partial U_F} S_{U_F, \text{Sys}}}_{\text{Term F1}} \quad (\text{A.15})$$

$$\text{Term F1:} \quad \frac{\partial \Theta'_F}{\partial U_F} = \frac{\text{Re}_F^{1/3}}{3U_FB} \quad (\text{A.16})$$

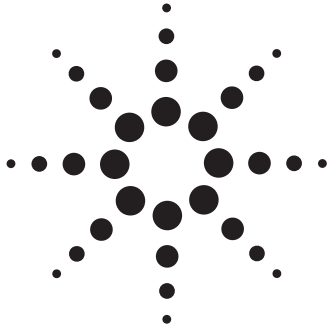
$$\text{Term F2:} \quad \frac{\partial \Theta'_F}{\partial h_{fg}} = \frac{\text{Re}_F^{1/3}}{BL} \quad (\text{A.17})$$

$$\text{Term F3:} \quad \frac{\partial \Theta'_F}{\partial \Delta h_c} = \frac{-Y_{\text{O}_2, \infty} \text{Re}_F^{1/3}}{rB^2L} \quad (\text{A.18})$$

$$\text{Term F4:} \quad \frac{\partial \Theta'_F}{\partial \ell} = \frac{\text{Re}_F^{1/3}}{3B\ell} \quad (\text{A.19})$$

# Appendix B

## Product Data Sheets



## Agilent 33220A 20 MHz Function/Arbitrary Waveform Generator

Data Sheet

- Fully compliant to LXI Class C specification
- 20 MHz Sine and Square waveforms
- Pulse, Ramp, Triangle, Noise, and DC waveforms
- 14-bit, 50 MSa/s, 64 k-point arbitrary waveforms
- AM, FM, PM, FSK, and PWM modulation types
- Linear & logarithmic sweeps and burst operation
- 10 mV<sub>pp</sub> to 10 V<sub>pp</sub> amplitude range
- Graph mode for visual verification of signal settings
- Connect via USB, GPIB and LAN



### Uncompromising performance for functions and waveforms

The Agilent Technologies 33220A function/arbitrary waveform generator uses direct digital synthesis (DDS) techniques to create a stable, accurate output signal for clean, low distortion sine waves. It also gives you square waves with fast rise and fall times up to 20 MHz and linear ramp waves up to 200 kHz.

### Pulse generation

The 33220A can generate variable-edge-time pulses up to 5 MHz. With variable period, pulse width, and amplitude the 33220A is ideally suited to a wide variety of applications requiring a flexible pulse signal.

### Custom waveform generation

Use the 33220A to generate complex custom waveforms. With 14-bit resolution, and a sampling rate of 50 MSa/s, the 33220A gives you the flexibility to create the waveforms you need. It also lets you store up to four waveforms in nonvolatile memory.

The Agilent IntuiLink arbitrary waveform software allows you to easily create, edit, and download complex waveforms using the waveform editor. Or you can capture a waveform using IntuiLink for Oscilloscope and send it to the 33220A for output. To find out more about IntuiLink, visit [www.agilent.com/find/intuilink](http://www.agilent.com/find/intuilink).



Agilent Technologies

Measurement Characteristics

**Easy-to-use functionality**

Front-panel operation of the 33220A is straight-forward and user friendly. You can access all major functions with a single key or two. The knob or numeric keypad can be used to adjust frequency, amplitude, offset, and other parameters. You can even enter voltage values directly in  $V_{pp}$ ,  $V_{rms}$ , dBm, or as high and low levels. Timing parameters can be entered in Hertz (Hz) or seconds.

Internal AM, FM, PM, FSK, and PWM modulation make it easy to modulate waveforms without the need for a separate modulation source. Linear and logarithmic sweeps are also built in, with sweep rates selectable from 1 ms to 500 s. Burst mode operation allows for a user-selected number of cycles per period of time. GPIB, LAN, and USB interfaces are all standard, plus you get full programmability using SCPI commands.

**External frequency reference (Option 001)**

The 33220A external frequency reference lets you synchronize to an external 10 MHz clock, to another 33220A, or to an Agilent 33250A. Phase adjustments can be made from the front panel or via a computer interface, allowing precise phase calibration and adjustment.

**Waveforms**

Standard	Sine, Square, Ramp, Triangle, Pulse, Noise, DC
Built-in arbitrary	Exponential rise, Exponential fall, Negative ramp, Sin(x)/x, Cardiac

**Waveforms Characteristics**

<b>Sine</b>		
Frequency Range	1 $\mu$ Hz to 20 MHz	
Amplitude Flatness <sup>[1], [2]</sup> (relative to 1 kHz)		
	< 100 kHz	0.1 dB
	100 kHz to 5 MHz	0.15 dB
	5 MHz to 20 MHz	0.3 dB
Harmonic distortion <sup>[2], [3]</sup>		
	< 1 $V_{pp}$	$\geq$ 1 $V_{pp}$
DC to 20 kHz	-70 dBc	-70 dBc
20 kHz to 100 kHz	-65 dBc	-60 dBc
100 kHz to 1 MHz	-50 dBc	-45 dBc
1 MHz to 20 MHz	-40 dBc	-35 dBc
Total harmonic distortion <sup>[2], [3]</sup>		
DC to 20 kHz	0.04%	
Spurious (non-harmonic) <sup>[2], [4]</sup>		
DC to 1 MHz	-70 dBc	
1 MHz to 20 MHz	-70 dBc + 6 dB/octave	
Phase noise (10 kHz offset)	-115 dBc / Hz, typical	
<b>Square</b>		
Frequency range	1 $\mu$ Hz to 20 MHz	
Rise/Fall time	< 13 ns	
Overshoot	< 2%	
Variable duty cycle	20% to 80% (to 10 MHz) 40% to 60% (to 20 MHz)	
Asymmetry (@ 50% duty)	1% of period + 5 ns	
Jitter (RMS)	1 ns + 100 ppm of period	
<b>Ramp, Triangle</b>		
Frequency range	1 $\mu$ Hz to 200 kHz	
Linearity	< 0.1% of peak output	
Variable Symmetry	0.0% to 100.0%	
<b>Pulse</b>		
Frequency range	500 $\mu$ Hz to 5 MHz	
Pulse width (period $\leq$ 10s)	20 ns minimum, 10 ns resolution	
Variable edge time	< 13 ns to 100 ns	
Overshoot	< 2%	
Jitter (RMS)	300 ps + 0.1 ppm of period	

**Noise**

Bandwidth	9 MHz typical
<b>Arbitrary</b>	
Frequency range	1 $\mu$ Hz to 6 MHz
Waveform length	2 to 64 k points
Amplitude resolution	14 bits (including sign)
Sample rate	50 MSa/s
Min. Rise/Fall Time	35 ns typical
Linearity	< 0.1% of peak output
Settling Time	< 250 ns to 0.5% of final value
Jitter (RMS)	6 ns + 30 ppm
Non-volatile memory	four waveforms

**Common Characteristics**

<b>Frequency</b>	
Accuracy <sup>[5]</sup>	$\pm$ (10 ppm + 3 pHz) in 90 days $\pm$ (20 ppm + 3 pHz) in 1 year
Resolution	1 $\mu$ Hz
<b>Amplitude</b>	
Range	10 mV <sub>pp</sub> to 10 V <sub>pp</sub> into 50 $\Omega$ 20 mV <sub>pp</sub> to 20 V <sub>pp</sub> into open circuit
Accuracy <sup>[1], [2]</sup> (at 1 kHz)	$\pm$ 1% of setting $\pm$ 1 mV <sub>pp</sub>
Units	$V_{pp}$ , $V_{rms}$ , dBm
Resolution	4 digits
<b>DC Offset</b>	
Range (peak AC + DC)	$\pm$ 5 V into 50 $\Omega$ $\pm$ 10 V into open circuit
Accuracy <sup>[1], [2]</sup>	$\pm$ 2% of offset setting $\pm$ 0.5% of amplitude $\pm$ 2 mV
Resolution	4 digits
<b>Main Output</b>	
Impedance	50 $\Omega$ typical
Isolation	42 Vpk maximum to earth
Protection	Short-circuit protected, overload automatically disables main output
<b>External Frequency Reference (Option 001)</b>	
<b>Rear Panel Input</b>	
Lock Range	10 MHz $\pm$ 500 Hz
Level	100 mV <sub>pp</sub> to 5 V <sub>pp</sub>
Impedance	1 k $\Omega$ typical, AC coupled
Lock Time	< 2 seconds
<b>Rear Panel Output</b>	
Frequency	10 MHz
Level	632 mV <sub>pp</sub> (0 dBm), typical
Impedance	50 $\Omega$ typical, AC coupled

## Appendix B: Product Data Sheets

### Measurement Characteristics (Continued)

#### Phase Offset

Range	+ 360° to - 360°
Resolution	0.001°
Accuracy	20 ns

#### Modulation

##### AM

Carrier waveforms	Sine, Square, Ramp, Arb
Source	Internal/External
Internal modulation	Sine, Square, Ramp, Triangle, Noise, Arb (2 MHz to 20 kHz)
Depth	0.0% to 120.0%

##### FM

Carrier waveforms	Sine, Square, Ramp, Arb
Source	Internal/External
Internal modulation	Sine, Square, Ramp, Triangle, Noise, Arb (2 MHz to 20 kHz)
Deviation	DC to 10 MHz

##### PM

Carrier waveforms	Sine, Square, Ramp, Arb
Source	Internal/External
Internal modulation	Sine, Square, Ramp, Triangle, Noise, Arb (2 MHz to 20 kHz)
Deviation	0.0 to 360.0 degrees

##### PWM

Carrier waveform	Pulse
Source	Internal/External
Internal modulation	Sine, Square, Ramp, Triangle, Noise, Arb (2 MHz to 20 kHz)
Deviation	0% to 100% of pulse width

##### FSK

Carrier waveforms	Sine, Square, Ramp, Arb
Source	Internal/External
Internal modulation	50% duty cycle square (2 MHz to 100 kHz)

#### External Modulation Input<sup>(6)</sup> (for AM, FM, PM, PWM)

Voltage range	± 5 V full scale
Input impedance	5 kΩ typical
Bandwidth	DC to 20 kHz

#### Sweep

Waveforms	Sine, Square, Ramp, Arb
Type	Linear or Logarithmic
Direction	Up or Down
Sweep time	1 ms to 500 s
Trigger	Single, External, or Internal
Marker	falling edge of sync signal (programmable frequency)

#### Burst<sup>(7)</sup>

Waveforms	Sine, Square, Ramp, Triangle, Pulse, Noise, Arb
Type	Counted (1 to 50,000 cycles), Infinite, Gated
Start/Stop Phase	-360° to +360°
Internal Period	1 μs to 500 s
Gate Source	External trigger
Trigger source	Single, External or Internal

#### Trigger Characteristics

Trigger input	
Input level	TTL compatible
Slope	Rising or Falling, selectable
Pulse width	> 100 ns
Input impedance	>10 kΩ, DC coupled
Latency	< 500 ns
Jitter (rms)	6 ns (3.5 ns for pulse)
Trigger output	
Level	TTL compatible into ≥ 1 kΩ
Pulse width	> 400 ns
Output Impedance	50 Ω, typical
Maximum rate	1 MHz
Fanout	≤ 4 Agilent 33220As

#### Programming Times (typical)

Configuration times	USB	LAN	GPIB
Function Change	111 ms	111 ms	111 ms
Frequency Change	1.5 ms	2.7 ms	1.2 ms
Amplitude Change	30 ms	30 ms	30 ms
Select User Arb	124 ms	124 ms	123 ms
Arb Download Times (binary transfer)			
64 k points	96.9 ms	191.7 ms	336.5 ms
16 k points	24.5 ms	48.4 ms	80.7 ms
4 k points	7.3 ms	14.6 ms	19.8 ms

#### General

Power Supply	CAT II 100 - 240 V @ 50/60 Hz (-5%, +10%) 100 - 120 V @ 400 Hz (±10%)
Power Consumption	50 VA max
Operating Environment	IEC 61010 Pollution Degree 2 Indoor Location
Operating Temperature	0°C to 55°C
Operating Humidity	5% to 80% RH, non-condensing
Operating Altitude	Up to 3000 meters
Storage Temperature	-30°C to 70°C
State Storage Memory	Power off state automatically saved. Four user-configurable stored states
Interface	USB, GPIB, and LAN standard
Language	SCPI - 1993, IEEE-488.2
Dimensions (W x H x D)	
Bench top	261.1 mm x 103.8 mm x 303.2mm
Rack mount	212.8mm x 88.3mm x 272.3mm
Weight	3.4 kg (7.5 lbs)
Safety Designed to	UL-1244, CSA 1010, EN61010
EMC Tested to	MIL-461C, EN55011, EN50082-1
Vibration and Shock	MIL-T-28800, Type III, Class 5
Acoustic Noise	30 dBA
Warm-up Time	1 hour
Warranty	1 year standard

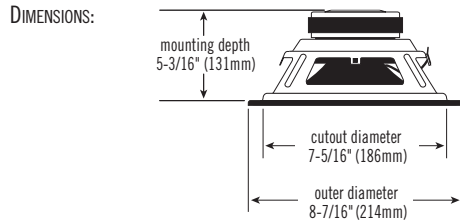
#### Footnotes

1. Add 1/10th of output amplitude and offset spec per °C for operation outside the range of 18°C to 28°C
2. Autorange enabled
3. DC offset set to 0 V
4. Spurious output at low amplitude is -75 dBm typical
5. Add 1 ppm/°C average for operation outside the range of 18°C to 28°C
6. FSK uses trigger input (1 MHz maximum)
7. Sine and square waveforms above 6 MHz are allowed only with an "infinite" burst count

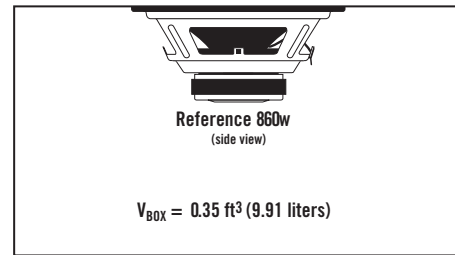
**Infinity** *Reference 860w 8" Woofer – Technical Data*

**SPECIFICATIONS**

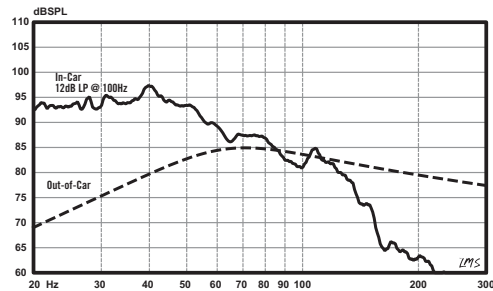
DIAMETER:	8" (200mm)
SENSITIVITY (2.83V @ 1m):	91dB
POWER HANDLING:	250W <sub>RMS</sub> (1000W <sub>PEAK</sub> )
FREQUENCY RESPONSE:	30Hz ~ 400Hz
NOMINAL IMPEDANCE:	4 OHMS
VOICE COIL DIAMETER:	2.0" (51.0mm)



**SEALED BOX VOLUME  
(INCLUDES DRIVER DISPLACEMENT)**



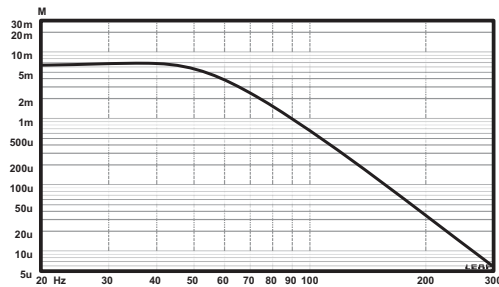
**SEALED ENCLOSURE  
FREQUENCY RESPONSE @ 2.83V**



**THIELE-SMALL PARAMETERS**

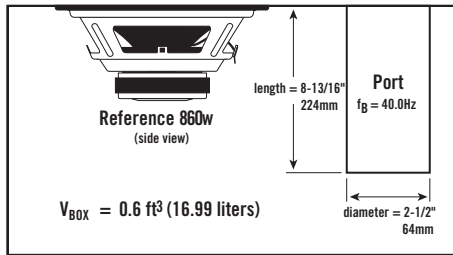
VOICE COIL DC RESISTANCE:	$R_{EVC}$ (OHMS) . . . . . 3.30
VOICE COIL INDUCTANCE @ 1kHz:	$L_{EVC}$ (MH) . . . . . 2.31
DRIVER RADIATING AREA:	$S_D$ (IN <sup>2</sup> ) . . . . . 33.17
	$S_D$ (M <sup>2</sup> ) . . . . . 214.00
MOTOR FORCE FACTOR:	$BL$ (TM) . . . . . 12.56
COMPLIANCE VOLUME:	$V_{AS}$ (FT <sup>3</sup> ) . . . . . 0.54
	$V_{AS}$ (LITERS) . . . . . 15.23
SUSPENSION COMPLIANCE:	$C_{MS}$ (µM/N) . . . . . 232.70
MOVING MASS, AIR LOAD:	$M_{MS}$ (GRAMS) . . . . . 124.20
MOVING MASS, DIAPHRAGM:	$M_{MD}$ (GRAMS) . . . . . 122.40
FREE-AIR RESONANCE:	$F_S$ (Hz) . . . . . 29.60
MECHANICAL Q:	$Q_{MS}$ . . . . . 6.10
ELECTRICAL Q:	$Q_{ES}$ . . . . . 0.483
TOTAL Q:	$Q_{TS}$ . . . . . 0.45
MAGNETIC-GAP HEIGHT:	$H_{AG}$ (IN) . . . . . 0.315
	$H_{AG}$ (MM) . . . . . 8.00
VOICE COIL HEIGHT:	$H_{VC}$ (IN) . . . . . 1.34
	$H_{VC}$ (MM) . . . . . 34
MAXIMUM EXCURSION:	$X_{MAX}$ (IN) . . . . . 0.513
	$X_{MAX}$ (MM) . . . . . 13.00

**SEALED ENCLOSURE  
CONE EXCURSION @ 250W**

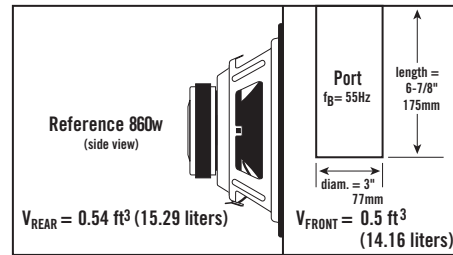


**Infinity** *Reference 860w 8" Woofer – Technical Data*

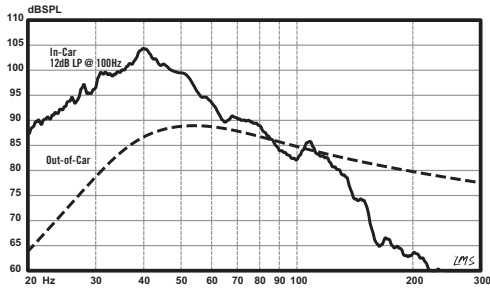
**VENTED BOX VOLUME  
(INCLUDES DRIVER/PORT DISPLACEMENTS)**



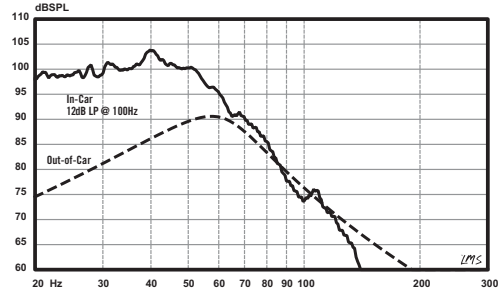
**BAND-PASS BOX VOLUME  
(INCLUDES DRIVER/PORT DISPLACEMENTS)**



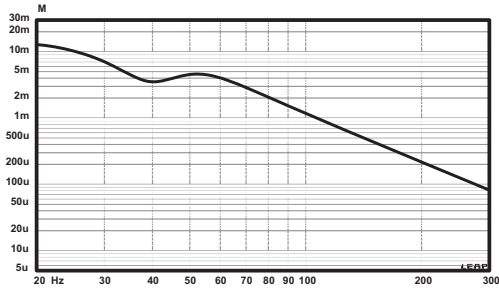
**VENTED ENCLOSURE  
FREQUENCY RESPONSE @ 2.83V**



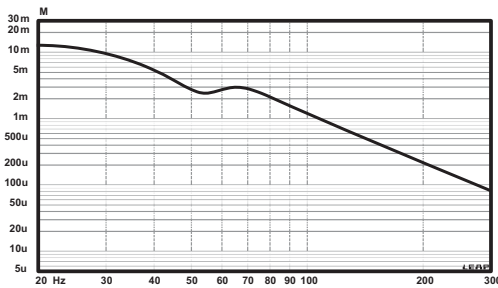
**BAND-PASS ENCLOSURE  
FREQUENCY RESPONSE @ 2.83V**



**VENTED ENCLOSURE  
CONE EXCURSION @ 250W**



**BAND-PASS ENCLOSURE  
CONE EXCURSION @ 250W**





2507 Warren Street, Elkhart, IN 46516 USA | 574.295.9495 | www.AETechron.com

The AE Techron **8102** power supply amplifier features an advanced switch-mode design that results in low noise and distortion, and high power density. It is configured as a single-channel, DC-coupled, controlled voltage amplifier ideal for reactive loads. The 8102 can provide up to 16 Arms or 235 Vrms continuous output. It offers a continuous, full-power frequency bandwidth of DC to 5 kHz.

The 8102 also features an integrated switching power supply that reduces weight and allows the unit to fit a standard 2U rack space. The 8102 operates from single-phase, 120-volt AC mains (230 VAC version available).

The 8102 amplifier is built and tested to the most stringent quality standards for long life and outstanding performance. The AE Techron brand is known throughout the world for its robust precision amplifiers as well as its product service and support.

**Performance**

*Specifications are for units driven into an 8-ohm load, (20 times voltage gain) and operating from 120 VAC, unless otherwise specified.*

*“Standard 1 kHz Power” refers to maximum average power in watts at 1 kHz with 0.1% THD.*

**Frequency Response:**

±3 dB from DC to 5 kHz at 1 watt

**Signal to Noise Ratio:**

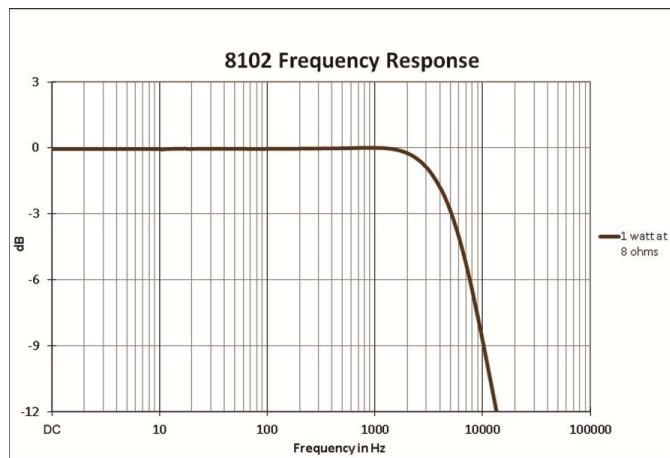
< 105 dB (ref. rated power, DC to 5 kHz, A-weighted).



**8102 SPECIFICATION SHEET**

**Features**

- Up to 16 Arms and 235 Vrms continuous output.
- Full-power frequency bandwidth of DC – 5 kHz.
- Compact design; only 2U of rack space and 27 lbs.
- Switching power supply for reduced weight.
- Installs easily into a standard 19-inch rack or stands alone for bench top operation.
- Built-in protection circuitry safely provides for sustained high-power output, with protection against input overloads, improper output connection (including shorts and improper loads), and excessive temperature, voltage or current.
- Operates from single-phase, 120-volt AC mains, (230 VAC version available).





**Total Harmonic Distortion (THD):**

<0.35% at full rated power, from DC to 5 kHz.

**I.M. Distortion:**

<0.35% at 60 Hz and 7 kHz at 4:1, from -40 dB to full rated power.

**DC Output Offset:**

< 15 mV

**Input Impedance** (nominally balanced, nominally unbalanced):

10 k ohms, 5 k ohms.

**Maximum Input Voltage:**

± 10 V balanced or unbalanced

**Common Mode Rejection (CMR)**

(20Hz to 1kHz, typical):

50 dB

**Load Impedance:**

2 – 62 ohm

**Gain Control** (when enabled, switch selectable):

Voltage gain adjustable from 20 to 0 or from 63 to 0

**Front Panel Controls and Indicators**

**Fault Indicator:**

Red LEDs, flash when the amplifier output has stopped operating. Usually this means that the amplifier must be serviced.

**Thermal Indicator:**

Red LEDs, illuminate when the amplifier has shut down, or is very near shutting down, due to thermal stress or overload.

**Ready Indicator:**

Green LEDs, illuminate when the amplifier is initialized and ready to produce output.

**Input Signal Indicator:**

Green LEDs, illuminate when the amplifier's input signal is above -40 dBu (8 mVrms).

**Output Signal Indicator, -20 dB:**

Green LEDs, illuminate when the amplifier's output signal is within 20 dB of clipping.

**Output Signal Indicator, -10 dB:**

Green LEDs, illuminate when the amplifier's output signal is within 10 dB of clipping.

**Clip Indicator:**

Red LEDs, illuminate when the amplifier's output signal reaches the onset of audible clipping. The Clip Indicators also will illuminate during Thermal Level Control (TLC) limiting or when the input compressor/limiter is protecting the amplifier from input overload.

**Cooling Vents:**

Front-to-rear forced airflow.

**Power Indicator:**

Blue LED indicates AC power has been applied and is within the safe operating range of the power supply. The LED will flash when the AC line voltage is approximately 15% above or 25% below the nominal rated value.

**Data Indicator:**

Feature not implemented.

**Bridge Indicator:**

Illuminates when the amplifier is receiving AC power.

**Power Switch:**

Push-on / push-off switch.

**Back Panel Controls and Connectors**

**Power Cord Connector:**

Standard 15 amp IEC inlet. A circuit breaker located near the IEC power inlet protects the amplifier from excessive AC current draw.

**Reset Switch:**

Resets the circuit breaker that protects the power supply.

**Ventilation Grille:**

Air flow is front to back. Do not block the ventilation grilles.

## Foundry Service & Supplies, Inc.

FUSED SILICA  
HOT PRESS PLATENS  
CASTABLE CERAMICS  
FIRED SHAPES  
AEROSPACE TOOLING

11808 E. Burke Street, Santa Fe Springs, CA 90670  
Telephone: (562) 945-6511  
Fax: (562) 696-1633

HI-TEMP INSULATIONS  
CALCIUM SILICATE BOARDS  
MILLBOARD AND BLANKET  
PAPERS AND CEMENTS  
CUTTING AND FABRICATING

 **Thermal Ceramics**  
INNOVATIVE SOLUTIONS FOR HEAT-INTENSIVE PROBLEMS

**KAOWOOL® LOW  
TEMPERATURE**

KAOWOOL VACUUM FORMED

### KAOWOOL LOW TEMPERATURE VACUUM FORMED PRODUCTS

Thermal Ceramics vacuum formed products are a rigid self-supporting fiber insulation manufactured from a slurry consisting of Kaowool ceramic fibers and binders. Thermal Ceramics products offer excellent thermal conductivity, strength and thermal stability at elevated temperatures. Thermal Ceramics products have the capability to withstand chemical attack. Exceptions include hydrofluoric acid, phosphoric acid, and strong alkalis. A small amount of combustible binder will burn out at approximately 300°F. Additional hardness and strength can be achieved with post treatments. Board capabilities are 48 x 36 x 1/4 to 3" with the exception of PM Board which can be made 1/8" thick.

**Kaowool PM** is manufactured to close tolerances with an excellent surface finish. Kaowool PM has a good thermal conductivity and can easily be die-cut.

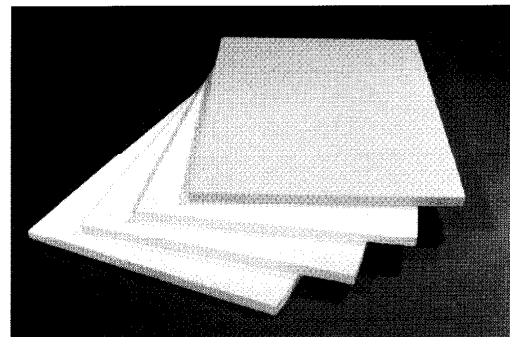
**Kaowool M** is a low cost general duty insulation product available in a variety of sizes and thicknesses. Kaowool M is a rigid self-supporting product that can be produced in different strength ranges to fit individual applications.

**Kaowool S** is a higher strength product with good non-ferrous molten metal resistance.

**Kaowool HD** is a low cost high strength product recommended for tough mechanical stress areas. Also, very good for back-up behind dense refractories.

**Kaowool HS** is a high strength product recommended for tough mechanical stress areas. Also, very good for back-up behind dense refractories.

**Kaowool HS45** is designed for a temperature rating of 2400°F with very high compressive and flexural strengths. Each board is machined to a thickness tolerance  $\pm 1/4 - 1/16$ ". Kaowool HS45 is non-wetting to molten aluminum metal and exhibits good resistance to chemical attack.



#### Chemical Properties

**Caution should be exercised during initial heating. Adequate ventilation should be provided to avoid potential flash ignition of the binder out-gassing or avoid air entry while at elevated temperature.**

#### Typical Applications

- Appliance and heat processing insulation
- Back up in steel ladle and torpedo cars
- Backup insulation to dense refractories
- Combustion chamber construction
- Expansion joint material
- Flue and chimney linings
- Furnace, kiln, and oven hot face linings
- General molten metal contact
- Glass coffin walls
- Glass regenerator insulation
- Glass tank side, end wall and port neck
- Glass tank wall and port neck insulation
- Heat shields
- High temperature gaskets and seals
- High mechanical stress areas
- Kiln furniture
- Trough linings in contact with aluminum

*Foundry Service & Supplies, Inc.*

FUSED SILICA  
HOT PRESS PLATENS  
CASTABLE CERAMICS  
FIRED SHAPES  
AFROSPACE TOOLING

11808 E. Burke Street, Santa Fe Springs, CA 90670  
Telephone: (562) 945-6511  
Fax: (562) 696-1633

HI-TEMP INSULATIONS  
CALCIUM SILICATE BOARDS  
MILLBOARD AND BLANKET  
PAPERS AND CEMENTS  
CUTTING AND FABRICATING

Ceramic Fiber • Insulating Firebrick • Refractory Castables and Monolithics • Mortars • Firebrick • Fired Refractory Shapes

**KAOWOOL VACUUM FORMED**

	Kaowool PM	Kaowool M	Kaowool S	Kaowool HD	Kaowool HS	Kaowool HS-45
<b>Physical Properties</b>						
Color.....	white	beige	brown	beige	beige	white
Nominal density, pcf.....	15	17	20	26	28	42
Maximum temperature rating, °F.....	2300	2300	2300	2400	2300	2400
Continuous use limit, °F.....	2100	2000	2000	2300	2200	2400
Melting point, °F.....	3200	3200	3200	3200	3200	2800
Modulus of rupture, psi.....	175-250	100-130	150-180	150 - 175	230-260	450-550
Compressive strength, psi						
@ 5% deformation.....	15-25	20-30	30-50	50 -70	60-80	200-250
@ 10% deformation.....	25-40	30-40	50-60	70 - 90	80-100	250-300
Linear shrinkage, %						
24 hrs @ 1500°F.....	0.2	1.2	1.0	0.1	0.8	0.5
24 hrs @ 1800°F.....	1.9	2.2	2.0	1.4	1.9	0.7
24 hrs @ 2000°F.....	2.4	2.8	2.3	2.5	2.1	0.4
24 hrs @ 2200°F.....	3.4	-	-	2.8	0.2	0.6
24 hrs @ 2400°F.....	-	-	-	-	+0.3	+0.8
<b>Chemical Analysis</b>						
Alumina, Al <sub>2</sub> O <sub>3</sub> .....	44	42	46	41	18	55
Silica, SiO <sub>2</sub> .....	56	56	53	53	81	35
Calcium Oxide, CaO.....	-	-	-	5	-	8
Other.....	<1	2	-	-	-	2
Loss of Ignition.....	4-7	4-7	5-8	5-8	5-8	5-8
Organic Material.....	3-6	3-6	4-7	4-7	4-7	4-7
<b>Thermal Conductivity, BTU•in/hrs•ft<sup>2</sup>•°F</b>						
Mean temperature						
@ 500°F.....	0.40	0.47	0.59	0.57	0.68	1.02
@ 1000°F.....	0.59	0.71	0.80	0.80	0.84	0.96
@ 1500°F.....	0.87	1.04	1.12	1.13	1.12	1.16
@ 2000°F.....	1.27	1.52	1.58	1.60	1.58	1.72

Data are average results of tests conducted under standard procedures and are subject to variation. Results should not be used for specification purposes.

Refer to the Material Safety Data Sheet (MSDS) for recommended work practices and other product safety information.

## Appendix B: Product Data Sheets



### MPA Series Microphones

MPA201 / MPA231 / MPA215 / MPA416 / MPA436 / MPA418 / MPA401

Model	MPA201	MPA231	MPA215	MPA416*	MPA436*	MPA418	MPA401
Photos							
Diameter	1/2"	1/2"	1/2"	1/4"	1/4"	1/4"	1/4"
Standards (IEC61672)	Class I	Class I	Class II	Class I	Class I	Class II	Class I
Microphone	MP201	MP231	MP215	Integrated	Integrated	MP418	MP401
Optimized	Free Field	Free Field	Free Field	Free Field	Free Field	Free Field	Free Field
Preamplifier	MA231(TEDS optional)	MA231(TEDS optional)	MA231(TEDS optional)	Integrated	Integrated	MA418	MA401
Frequency Response (Hz)	20 ~ 20k	20 ~ 20k	20 ~ 12.5k	20 ~ 20k	20 ~ 20k	20 ~ 16k	20 ~ 70k
Open-circuit Sensitivity (mV/Pa) ( $\pm 2$ dB)	45	40	40	50	12.5	10	5
Output Impedance ( $\Omega$ )	< 50	< 50	< 110	< 110	< 110	< 110	< 110
Dynamic Range (dBA)	16 ~ 134	17 ~ 136	23 ~ 135	29 ~ 127	35 ~ 130	36 ~ 135	35 ~ 155
Inherent Noise (dBA)	< 16	< 17	< 23	< 29	< 35	< 36	< 35
Operating Temperature ( $^{\circ}$ C)	-30 ~ 80	-30 ~ 80	-20 ~ 80	-10 ~ 50	-10 ~ 50	0 ~ 40	-20 ~ 80
Operating Humidity (RH)	0 ~ 95%	0 ~ 95%	0 ~ 95%	0 ~ 95%	0 ~ 95%	0 ~ 98%	0 ~ 98%
Temperature Coefficient (dB/ $^{\circ}$ C)	0.005	0.005	$\leq \pm 0.3$ dB (0 ~ 40 $^{\circ}$ C) with 250Hz, at reference temperature 23 $^{\circ}$ C	15 ~ 35 $^{\circ}$ C: $\leq \pm 0.3$ dB; 0 ~ 40 $^{\circ}$ C: $\leq \pm 1.5$ dB; -10 ~ 50 $^{\circ}$ C: $\leq \pm 3.0$ dB; with 1000Hz, at reference temperature 23 $^{\circ}$ C	23 $^{\circ}$ C(15 ~ 35 $^{\circ}$ C): $\leq \pm 0.3$ dB; 0 ~ 40 $^{\circ}$ C: $\leq \pm 1.5$ dB; -10 ~ 50 $^{\circ}$ C: $\leq \pm 3.0$ dB; with 1000Hz, at reference temperature 23 $^{\circ}$ C	$\leq \pm 0.6$ (0 ~ 40 $^{\circ}$ C) at reference temperature 23 $^{\circ}$ C	-0.009
Humidity Coefficient (dB/%RH)	0.003	0.003	0.007	20% ~ 90% RH: $\leq \pm 0.8$ dB with 1000Hz, at reference temperature 23 $^{\circ}$ C, Humidity 50% RH	20% ~ 90% RH: $\leq \pm 0.8$ dB with 1000Hz, at reference temperature 23 $^{\circ}$ C, Humidity 50% RH	0.015	0.003
Pressure Coefficient (250 Hz) (dB/kPa)	-0.004	-0.004	-0.03	-0.06	-0.06	-0.06	-0.007
Length (mm)	91	91	91	61	24	64	67
Input Connector	BNC	BNC	BNC	SMB	SMB	SMB	SMB
Corresponding Model with TEDS	MPA261	MPA271	MPA265	MPA466	--	--	--

\*The MPA416 & MPA436 are the most suitable models for array uses. The frequency responses meet the IEC 61672 Class 1 requirements.

## Appendix B: Product Data Sheets



### Microphone Conditioning Units

MC102 / MC141 / MC104 / MC711 / MC722

Model	MC102	MC141	MC104	MC711	MC722
Photos					
Number of Input Channels	2	1	4	1	2
Connector of Input	BNC	BNC	BNC	7-pin LEMO	7-pin LEMO
Number of Output Channels	2	1	4	1	2
Connector of Output	BNC	BNC	BNC	BNC	BNC
Frequency Response (Hz)	5 ~ 200k	5 ~ 200k	5 ~ 200k	1 ~ 1M	5 ~ 200k
Gain	--	$\times 1, \times 10$	$\times 0.1, \times 1, \times 10$	--	-20 dB, 0 dB, 20 dB, 40dB
Polarization Voltage	0 V	0 V	0 V	200 V or 0 V	200 V or 0 V
Output Power for Preamp	4 mA	4 mA	4 mA	28 V	28 V or 120 V
Power Supply	1 x 9 V Battery or 220 V	220 V	220 V	220 V	220 V
Filter	--	--	--	--	Lin, AW, HP, Dir
Operating Temperature (°C)	-10 ~ 50	-10 ~ 50	-10 ~ 50	-10 ~ 50	-10 ~ 50
Operating Humidity (RH)	0 ~ 95%	0 ~ 95%	0 ~ 95%	0 ~ 95%	0 ~ 95%
Dimension (mm)	113 x 70 x 45	113 x 70 x 45	310 x 250 x 65	113 x 70 x 45	260 x 60 x 150
Weight (g)	160	160	1500	190	1130





**CA111/CA114/CA115** is small sound source for calibrating measurement microphones, sound level meters, and other sound measurement equipments. The calibrator can be used on 1/2-inch and 1/4-inch microphones with adaptor.

**CA111** conforms to IEC 60942:2003 Class 1, ANSI S1.40-1984 and GB/T 15173-1994.

**CA114/115** conforms to IEC 60942:2003 Class 2 standards.



### APPLICATIONS

- Calibration of measurement microphones, sound level meters, and other sound measurement equipments.
- Checking the linearity of equipments.

### FEATURES

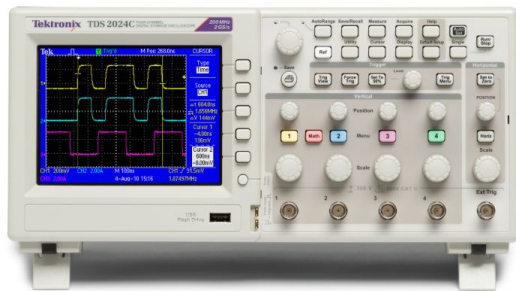
- Conforms to IEC60942:2003 Class 1/Class 2, ANSI S1.40-1984, and GB/T 15173-1994.
- 1 kHz calibration frequency for all weighting networks.
- CA111: Dual 94 & 114 dB sound pressure level outputs.
- CA114: 94 dB sound pressure level outputs.
- CA115: 114 dB sound pressure level outputs.
- Calibration accuracy  $\pm 0.3$  dB.
- Designed with highly stable level and frequency.
- CA111 for two-keypad operation and CA114/115 for one-keypad operation.
- Fits 1/2" microphones and 1/4" microphones with adaptor.
- Powered by 2×AAA battery and automatic power off to conserve battery life.

### SPECIFICATIONS

Sound Calibrators		
Model	CA111	CA114/CA115
Standard	IEC60942:2003 Class 1, ANSI S1.40-1984, GB/T 15173-1994	IEC60942:2003 Class 2, ANSI S1.40-1984, GB/T 15173-1994
Sound Pressure Level	94.0 dB $\pm 0.3$ dB and 114.0 dB $\pm 0.3$ dB	94.0dB/114.0 dB $\pm 0.3$ dB
Frequency	1000Hz $\pm 0.5\%$	
Microphone Diameter	According to IEC61094-4: 1/2" & 1/4"	
Harmonic Distortion	<2% Stabilization Time: <10 s	
Equivalent Free-field Level	-0.2 dB for 1/2" Microphones	
Equivalent Random Incidence Level	+0.0 dB for 1/2", 1/4"	
Reference Conditions	Ambient Temperature: 25°C (77°F) / Ambient Pressure: 101.3 kPa / Humidity: 55% RH / Effective Load Volume: 250 mm <sup>3</sup>	
Environmental Conditions	Temperature: -10°C-50°C (14°F -122°F) Pressure: 65 kPa to 108 kPa Humidity: 10 to 90%RH (non-condensing)	
Power Supply	Batteries: 1.5 V LR6 (AA battery) $\times 2$ Lifetime: Typically 40 hours with alkaline batteries at 25°C (77°F)	
Dimension(mm)	48 $\times$ 70 $\times$ 70mm	
Weight	180 g, including batteries	



## Digital Storage Oscilloscopes TDS2000C Series Datasheet



The TDS2000C Digital Storage Oscilloscope Series provides you with affordable performance in a compact design. Packed with standard features - including USB connectivity, 16 automated measurements, limit testing, data logging, and context-sensitive help - the TDS2000C Series oscilloscopes help you get more done in less time.

### Key performance specifications

- 200 MHz, 100 MHz, 70 MHz, 50 MHz bandwidth models
- 2- and 4-channel models
- Up to 2 GS/s sample rate on all channels
- 2.5k point record length on all channels
- Advanced triggers including pulse width trigger and line-selectable video trigger

### Key features

- 16 automated measurements and FFT analysis for simplified waveform analysis
- Built-in waveform limit testing
- Automated, extended data logging feature
- Autoset and signal auto-ranging
- Built-in context-sensitive help
- Probe check wizard
- 11-language user interface
- 144 mm (5.7 inch) active TFT color display
- Small footprint and lightweight - only 124 mm (4.9 inches) deep and 2 kg (4.4 lb)
- USB 2.0 host port on the front panel for quick and easy data storage

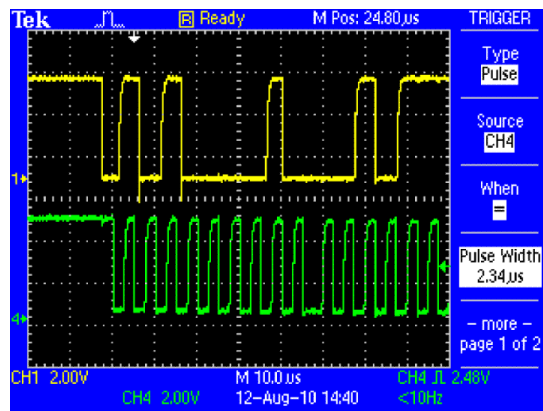
- USB 2.0 device port on the rear panel for easy connection to a PC or for direct printing to a PictBridge®-compatible printer
- Includes National Instrument's LabVIEW SignalExpress™ TE Limited Edition and Tektronix OpenChoice® Software for connecting to your bench
- Lifetime warranty. Limitations apply. For terms and conditions, visit [www.tektronix.com/lifetimewarranty](http://www.tektronix.com/lifetimewarranty)

### Digital precision for accurate measurements

With up to 200 MHz bandwidth and 2 GS/s maximum sample rate, no other digital storage oscilloscope offers as much bandwidth and sample rate for the price. Tektronix proprietary sampling technology provides real-time sampling with a minimum of 10X oversampling on all channels, all the time to accurately capture your signals. Sampling performance is not reduced when using multiple channels.

### Critical tools for troubleshooting your device

Advanced triggers - rising/falling edge, pulse width, and video - help you quickly isolate your signals of interest. Once you've captured a signal, advanced math capabilities and automated measurements can speed your analysis. Quickly perform an FFT or add, subtract, or multiply waveforms. Sixteen automated measurements quickly and reliably calculate important signal characteristics such as frequency or rise time, while the built-in Limit Test function enables you to easily identify problems in your signal.



Quickly and easily capture waveforms with advanced triggering.

## Specifications

All specifications apply to all models unless noted otherwise.

### Overview

	TDS2001C	TDS2002C	TDS2004C	TDS2012C	TDS2014C	TDS2022C	TDS2024C
Display (QVGA LCD)	TFT on all models						
Bandwidth	50 MHz	70 MHz	70 MHz	100 MHz	100 MHz	200 MHz	200 MHz
Channels	2	2	4	2	4	2	4
External trigger input	Included on all models						
Sample rate on each channel	500 MS/s	1.0 GS/s	1.0 GS/s	2.0 GS/s	2.0 GS/s	2.0 GS/s	2.0 GS/s

### Vertical system

Record length	2.5k points at all time bases on all models
Vertical resolution	8 bits
Vertical sensitivity	2 mV to 5 V/div on all models with calibrated fine adjustment
DC vertical accuracy	±3% on all models
Vertical zoom	Vertically expand or compress a live or stopped waveform
Maximum input voltage	300 V <sub>RMS</sub> CAT II; derated at 20 dB/decade above 100 kHz to 13 V <sub>p-p</sub> AC at 3 MHz
Position range	2 mV to 200 mV/div +2 V; >200 mV to 5 V/div +50 V
Bandwidth limit	20 MHz for all models
Input impedance	1 MΩ in parallel with 20 pF
Input coupling	AC, DC, GND on all models

### Horizontal system

Time base accuracy	50 ppm
Horizontal zoom	Horizontally expand or compress a live or stopped waveform

## Datasheet

### Trigger system

<b>Trigger modes</b>	Auto, Normal, Single Sequence
<b>Trigger types</b>	
<b>Edge (rising/falling)</b>	Conventional level-driven trigger. Positive or negative slope on any channel. Coupling selections: AC, DC, Noise Reject, HF Reject, LF Reject
<b>Video</b>	Trigger on all lines or individual lines, odd/even or all fields from composite video, or broadcast standards (NTSC, PAL, SECAM)
<b>Pulse width (or glitch)</b>	Trigger on a pulse width less than, greater than, equal to, or not equal to, a selectable time limit ranging from 33 ns to 10 s
<b>Trigger source</b>	
<b>2-channel models</b>	CH1, CH2, Ext, Ext/5, AC Line
<b>4-channel models</b>	CH1, CH2, CH3, CH4, Ext, Ext/5, AC Line
<b>Trigger view</b>	Displays the trigger signal while the Trigger View button is depressed
<b>Trigger signal frequency readout</b>	Provides a frequency readout of the trigger source

### Acquisition system

<b>Acquisition modes</b>	
<b>Peak detect</b>	High-frequency and random glitch capture. Captures glitches as narrow as 12 ns (typical) at all time base settings from 5 $\mu$ s/div to 50 s/div
<b>Sample</b>	Sample data only
<b>Average</b>	Waveform averaged, selectable: 4, 16, 64, 128
<b>Single sequence</b>	Use the Single Sequence button to capture a single triggered acquisition sequence
<b>Roll mode</b>	At acquisition time base settings of >100 ms/div

### Waveform measurements

<b>Automatic waveform measurements</b>	Period, Frequency, +Width, -Width, Rise Time, Fall Time, Max, Min, Peak-to-Peak, Mean, RMS, Cycle RMS, Cursor RMS, Duty Cycle, Phase, Delay
<b>Cursors</b>	
<b>Types</b>	Amplitude and time
<b>Measurements</b>	$\Delta T$ , $1/\Delta T$ (frequency), $\Delta V$

### Waveform math

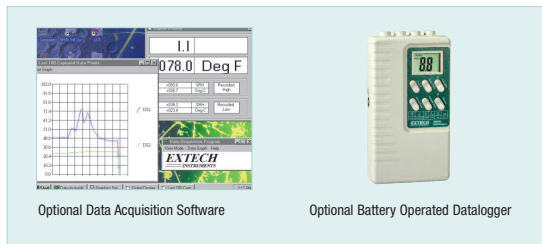
<b>Operators</b>	Add, Subtract, Multiply, FFT
<b>Sources</b>	
<b>2-channel models</b>	CH1 - CH2, CH2 - CH1, CH1 + CH2, CH1 x CH2
<b>4-channel models</b>	CH1 - CH2, CH2 - CH1, CH3 - CH4, CH4 - CH3, CH1 + CH2, CH3 + CH4, CH1 x CH2, CH3 x CH4
<b>FFT</b>	Windows: Hanning, Flat Top, Rectangular 2,048 sample points

## Heavy Duty Hot Wire Thermo-Anemometer

 **Telescoping probe is designed to fit into small openings**  
And measures airflow down to 40ft/min (0.2m/s)

### Features:

- Telescoping probe is ideal for measuring in HVAC ducts and other small vents; extends up to 7ft (2.1m) maximum length with cable
  - Super large 1.4" (36mm) dual LCD display
  - MAX/MIN, Data Hold
  - Optional Data Acquisition software (407001) and Datalogger (380340);
  - Complete with telescoping probe with cable, six AAA batteries and protective holster.
- NOTE: AC Adaptor not available for this model.



Specifications	Resolution	Basic Accuracy
Air Velocity		
0.2 to 20m/s	0.1m/s	±3%
40 to 3940ft/min	10ft/min	
0.5 to 45MPH	0.1MPH	
1.0 to 31knots:	0.1knots	
0.7 to 72km/h	0.1km/h	
Temperature & Windchill		
0 to 50°C	0.1°	±0.8°C
32 to 122°F	0.1°	±1.5°F
Dimensions	7 x 2.9 x 1.3" (178 x 74 x 33mm)	
Weight	17oz (482g)	

### Ordering Information:

- 407123 .....Heavy Duty Hot Wire Thermo-Anemometer  
 407123-NIST .....Heavy Duty Hot Wire Thermo-Anemometer w/ Calibration Traceable to NIST.  
 407001 .....Data Acquisition Software and Serial Cable  
 407001-USB .....USB Adaptor for 407001  
 380340 .....Battery Operated Datalogger  
 153117 .....117V AC Adaptor  
 153220 .....220V AC Adaptor



## DATA SHEET

For the most current version visit [www.visionresearch.com](http://www.visionresearch.com)  
Subject to change Rev September 2013



Phantom v641  
Shown with optional CineMag interface  
and On-Camera Controls

### Key Benefits:

#### WHEN IT'S TOO FAST TO SEE, AND TOO IMPORTANT NOT TO®

The Phantom v641 is the second generation v640 camera. It's smaller and lighter than its predecessor and has a number of new convenience features requested by users.

The v641 provides a 4 megapixel sensor and greater than 6 gigapixels/second throughput. That means full-resolution frame rates of 1450 frames-per-second (fps), and 1920 x 1080 HD-resolution frame rates of 2560 fps. The minimum frame rate is 10 fps.

**Take the wide view** with our custom-designed 2560 x 1600 pixel CMOS sensor. The aspect ratio of the v641 allows you to keep moving targets in-frame longer and see more of the event you are recording.

## v641

2560 x 1600 resolution

10-1450 fps at full resolution

Breakthrough sensitivity

Phantom CineMag® compatible

### Key Features:

- 10-1450 frames-per-second (fps) at full resolution.  
Maximum FPS: 219,000 @ 256 x 8
- 2560 x 1600 CMOS sensor
- Minimum Exposure (shutter speed): 1  $\mu$ s
- High-resolution timing system: Better than 20 ns resolution
- Extreme Dynamic Range (EDR): two different exposures within a single frame
- Internal Shutter Mechanism: hands-free/remote current session reference (CSR)
- Memory Segmentation: Up to 63 segments
- Non-volatile, hot-swappable Phantom CineMag memory magazines (128 GB, 256 GB & 512 GB)
- CineMag to CineStation®
- Range Data input
- Built-in Memory: 8 GB, 16 GB, 32 GB
- Breakthrough Sensitivity: ISO (ISO-12232 SAT Method)  
Mono: 16,000 T and 6400 D  
Color: 1600 T and 1600 D  
QE 60% peak; NEP 0.011 fJ
- Pixel Bit-depth: 12-bit
- Gb Ethernet, 10 Gb Ethernet with optional CineStream X2SR module
- Image-Based Auto-Trigger
- Burst Mode
- IRIG & SMPTE Time Code
- Genlock

**AMETEK**  
MATERIALS ANALYSIS DIVISION

DATA SHEET



when it's too fast to see, and too important not to.®

v641

Phantom v641 provides a 4 megapixel sensor and greater than 6 gigapixels/second throughput.

Shutter speeds down to 1 microsecond and a **global electronic shutter** allow for crisp, sharp images with little or no image blur or motion artifacts.

With a peak quantum efficiency (QE) of 60% – greatly improved over current sensor designs – and a significant reduction in readout noise, along with the addition of microlens technology, the v641's **four megapixel resolution can be used to full advantage** at speeds that normally called for large-pixel, lower resolution cameras.

That makes the v641 ideal for applications where **high sensitivity and high resolution** are needed. Coupled with a 1.4 microseconds straddle time the v641 is ideal for **PIV applications**, for example.

Each camera supports **12-bit pixel depth**. Smaller bit-depth gives you more recording time and smaller files. Greater bit-depth gives you more gray levels and finer detail. With the greater latitude of 12 bits, you can pull more detail out of the image.

The v641's **high-resolution timing system** yields a timing resolution of better than 20 nanoseconds. Frame rate, frame synchronization and exposure accuracy are all improved over previous generations of high-speed cameras. And, an external frame synchronization signal is available via a dedicated BNC for easier cabling and increased signal integrity. A GenLock input is available for synchronizing the playback of recorded cines to other video gear.

Of course, the v641 offers our unique **Extreme Dynamic Range (EDR)** feature giving you the ability to get two different exposures within a single frame. And, with **auto exposure**, the camera adjusts to changing lighting conditions automatically.

There is an **internal shutter** for cutting off all light to the sensor when doing a session-specific black reference (CSR). You now can do **remote CSRs** through software control without the need to manually cover the lens!

The v641 comes standard with 8 GB of high-speed dynamic RAM, but you can order 16 GB or 32 GB versions. Our **segmented memory** allows you to divide this into up to 63 segments so you can take multiple shots back-to-back without the need to download data from the camera.

You are able to record directly to our **Phantom CineMag** non-volatile, hot-swappable memory magazines. They mount on the CineMag compatible version of the camera. **Continuously record** full-resolution cines into

non-volatile memory at up to 195 fps (360 fps for 1920 x 1080). That's about 4.5 minutes of continuous recording into the 256 GB CineMag or 9 minutes into the 512 GB CineMag.

Or, record at higher speeds into camera RAM, then manually or automatically move your cine to the CineMag. If you need to **take multiple shots back-to-back**, you don't have to wait for a time-consuming download of camera memory over Ethernet. Instead, just upload the camera memory to a CineMag at about 800 megapixels/second, then take your next shot!

With CineMag storage you get maximum data protection and an ideal storage medium for secure environments.

Move the CineMag from the camera to a **CineStation** connected to a PC and view, edit, and save your cines using the Phantom Software supplied with the camera.

Keep them in their original cine raw format, or convert them to TIFF, QuickTime, AVI, or a number of other formats. Move the files from the CineStation to a disk or tape deck via 10 Gb Ethernet, dual HD-SDI, or Component Video outputs.

When used on a tracking mount, elevation and azimuth data can be transferred to the camera and associated with image frames through our unique **Range Data** input.

**View your recordings immediately.** There are two **Versatile Dual HD-SDI ports** that can be used in one of four different modes: 2 identical 4:2:2 outputs; 1 dual HD-SDI 4:4:4 output; independent 4:2:2 outputs where one is live and one is playback; or 4:4:4 playback on the dual HD-SDI while you have a live image on the component viewfinder. Yes, a component video viewfinder port has been added so any viewfinder compatible with our Phantom HD camera can now be used with the v641.

The v641 is controlled by the feature-rich Phantom Software. If you've used any Phantom camera before, you will know how to run the v641. As an option, you can add **On-Camera Controls (OCC)** to get full control of the camera without the need to connect to a PC. We also provide a full-featured **Remote Control Unit (RCU)** for wired or wireless control.

The v641 comes in two base models, either with or without a CineMag interface. An optical low-pass filter is available as an option.

H	V	FPS*
256	8	219,200
256	64	90,200
256	128	53,900
256	256	29,800
512	384	16,200
512	512	12,300
640	480	10,700
800	600	7,370
1280	720	5,350
1280	800	4,820
1280	1024	3,780
1920	1080	2,560
2048	1024	2,700
2048	1600	1,730
2560	1600	1,450

\*Typical results

ISO SAT			
Mono		Color	
ISO SAT T	ISO SAT D	ISO SAT T	ISO SAT D
16,000	6400	1600	1600

## Trusted Results at Your Fingertips

### Worry-free Weighing, 0.01 – 0.1 g



#### Metal housing ensures long balance lifetime

The full die-cast aluminum housing not only protects the weighing cell from environmental influences and impacts, it is also resistant to harsh chemicals, including acetone.



#### Proven weighing cell delivers reliable results

Our renowned MonoBloc weighing cell, with proFACT automatic internal adjustment, delivers consistently reliable results. Built-in overload protection ensures a long balance lifetime.



#### MinWeigh function assists dosing process

During weighing-in, the weight value remains red until the net sample weight is above the pre-programmed minimum value. It is clear to see when process tolerances have been met.



#### Built-in function simplifies balance leveling

The built-in LevelControl function issues a warning when the balance is not level and provides onscreen guidance to help you level the balance correctly within seconds.



### MS-TS Precision Balances Engineered for Reliable Performance

The robust construction of the MS-TS precision balances makes them perfect for heavier tasks in the laboratory or out on the factory floor. The unique MonoBloc weighing cell delivers the accuracy you need and is fully protected against accidental overload.

Delivering consistently reliable results, even in harsh environments, these balances will also deliver a fast return on your investment.

The 7" extra-large color TFT touchscreen display is operable through cotton, silicon and rubber gloves. An intuitive user interface and 18mm high digits bring comfort to your daily tasks.

METTLER TOLEDO

## Appendix B: Product Data Sheets

### MS-TS Precision Balances, 0.01 – 0.1 g

Technical Specifications	MS1602TS	MS3002TS	MS4002TS	MS4002TSR	MS6002TS	MS6002TSR	MS12002TS	MS8001TS
<b>Limit values</b>								
Maximum capacity	1620 g	3200 g	4200 g	4200 g	6200 g	6200 g	12200 g	8200 g
Maximum capacity, fine range	–	–	–	820 g	–	1220 g	–	–
Readability	0.01 g	0.01 g	0.01 g	0.1 g	0.01 g	0.1 g	0.01 g	0.1 g
Readability, fine range	–	–	–	0.01 g	–	0.01 g	–	–
Repeatability	0.01 g	0.01 g	0.01 g	0.06 g	0.01 g	0.06 g	0.01 g	0.1 g
Repeatability, fine range	–	–	–	0.01 g	–	0.01 g	–	–
Linearity deviation	0.02 g	0.02 g	0.02 g	0.08 g	0.02 g	0.08 g	0.025 g	0.2 g
<b>Typical values</b>								
Repeatability	0.007 g	0.007 g	0.007 g	0.05 g	0.007 g	0.05 g	0.007 g	0.07 g
Repeatability, fine range	–	–	–	0.007 g	–	0.007 g	–	–
Linearity deviation	0.006 g	0.006 g	0.006 g	0.06 g	0.006 g	0.06 g	0.008 g	0.06 g
Sensitivity offset (test weight)	0.018 g (1600 g)	0.018 g (3000 g)	0.024 g (4000 g)	0.024 g (4000 g)	0.036 g (6000 g)	0.036 g (6000 g)	0.048 g (12000 g)	0.24 g (8000 g)
USP minimum sample weight (5% load, k=2, U=0.10%)	14 g	120 g						
Minimum sample weight (5% load, k=2, U=1%)	1.4 g	12 g						
Settling time	1.5 s	1 s						
<b>Dimensions</b>								
Weighing pan size, WxD (mm)	170 x 200	190 x 226						

#### Features

<b>Accurate Results</b>	MonoBloc weighing cell Strong overload protection proFACT internal adjustment MinWeigh warning function Full metal housing
<b>Efficient Operation</b>	7" Extra-large color TFT touchscreen 18mm high digits LevelControl function Statistical data analysis Easy cleaning LevelLock
<b>Quality Assurance</b>	ISO-Log Sample ID input Passcode protection
<b>Seamless Process</b>	3 interfaces: USB device, USB host, RS232 Bluetooth option PC Direct application

#### Accessories

##### P-5x thermal printers



Fast, high quality printouts on paper, self-adhesive labels and continuous self-adhesive paper (including barcodes).

##### Pan protectors



Self-adhesive sheet protects your balance and absorbs minor spills. Peel off and replace as required.

##### Bluetooth adaptors



Wirelessly sends data between the balance and a PC, tablet or printer. No additional software needed.

##### External draft shield



The large draft shield protects your balance from air currents. Get faster and more accurate results.

#### Embedded applications

Weighing, statistics for all applications, check weighing, totaling, piece counting, formulation, percent weighing, factor weighing, dynamic weighing, density, dosing and PC Direct (for easy data transfer).

For further information on accessories, please visit [www.mt.com/lab-accessories](http://www.mt.com/lab-accessories)

**GWP®**  
Good Weighing Practice™  
[www.mt.com/GWP](http://www.mt.com/GWP)



**Mettler-Toledo AG**  
Laboratory Weighing  
CH-8606 Greifensee, Switzerland  
Tel. +41 44 944 22 11  
Fax +41 44 944 30 60

Subject to technical changes  
© 01/2015 Mettler-Toledo AG  
30248772  
Global MarCom Switzerland

[www.mt.com/ms-precision](http://www.mt.com/ms-precision)

For more information

# Bibliography

- [1] P.J. DiNenno and G.M. Taylor. Halon and halon replacement agents and systems. In A.E. Cote, editor, *Fire Protection Handbook*, pages 17.93–17.121. National Fire Protection Association, Quincy, MA, twentieth edition, 2008.
- [2] S. McCormick, M. Clauson, and H. Cross. Us army ground vehicle crew compartment halon replacement program. In *Halon Options Technical Working Conference*, pages 229–236, May 2000.
- [3] R.M. Gagnon. *Design of Special Hazard and Fire Alarm Systems*. Thomson Delmar Learning, Clifton Park, NY, second edition, 2008.
- [4] G.M. Whiteside. Instant flame suppression. Technical report, United States Department of Defense, 2013.
- [5] F.A. Williams. *Combustion Theory*. Benjamin/Cummings Publishing Company, Menlon Park, CA, 2 edition, 1985.
- [6] J.G. Quintiere and A.S. Rangwala. A theory for flame extinction based on flame temperature. *Fire and Materials*, 28:387–402, 2004.
- [7] Y. Jin and B.D. Shaw. Computational modeling of n-heptane droplet combustion in air–diluent environments under reduced-gravity. *International Journal of Heat and Mass Transfer*, 53(25–26):5782–5791, 2010.

- [8] H.Z. Yu and J.S. Newman. Theories of fire extinguishment. In A.E. Cote, editor, *Fire Protection Handbook*, pages 2.80–2.92. National Fire Protection Association, Quincy, MA, twentieth edition, 2008.
- [9] S.H. Won, S. Dooley, F. L. Dryer, and Yiguang Ju. A radical index for the determination of the chemical kinetic contribution to diffusion flame extinction of large hydrocarbon fuels. *Combustion and Flame*, 159(4):541–551, 2012.
- [10] F. Kreith, S.A. Berger, S.W. Churchill, J.P. Tullis, F.M. White, A.T. McDonald, A. Kumar, J.C. Chen, T.F. Irvine, M. Capobianchi, F.E. Kennedy, E.R. Booser, D.F. Wilcock, R.F. Boehm, R.D. Reitz, S.A. Sherif, and B. Bhushan. Fluid mechanics. In F. Kreith, editor, *Mechanical Engineering Handbook*. CRC Press, Boca Raton, FL, 1999.
- [11] K.K. Kuo and R. Acharya. *Fundamentals of Turbulent and Multiphase Combustion*. John Wiley & Sons, Hoboken, NJ, 2012.
- [12] K.W. Jenkins, M. Klein, N. Chakraborty, and R.S. Cant. Effects of strain rate and curvature on the propagation of a spherical flame kernel in the thin-reaction-zones regime. *Combustion and Flame*, 145:415–434, 2006.
- [13] S.M. Candel and T.J. Poinso. Flame stretch and the balance equation for the flame area. *Combustion Science and Technology*, 70(1–3):1–15, 1990.
- [14] A. Liñán. The asymptotic structure of counterflow diffusion flames for large activation energies. *Acta Astronautica*, 1:1007–1039, 1974.
- [15] B. Karlovitz, D.W. Denniston, D.H. Knapschafer, and F.E. Wells. Fourth symposium (international) on combustion studies on turbulent flames. *Symposium (International) on Combustion*, 4(1):613–620, 1953. ISSN 0082-0784.
- [16] V.R. Katta, T.R. Meyer, M.S. Brown, J.R. Gord, and W.M. Roquemore. Extinction criterion for unsteady, opposing-jet diffusion flames. *Combustion and Flame*, 137(1–2):198–221, 2004. ISSN 0010-2180.

- [17] J.G. Quintiere. *Fundamentals of Fire Phenomena*. John Wiley & Sons, West Sussex, England, 2006.
- [18] V.R. Lecoustre, P. Narayanan, H.R. Baum, and A. Trouve. Local extinction of diffusion flames in fires. *Proceedings of the Tenth International Symposium on Fire Safety Science*, pages 583–596, 2011.
- [19] S.R. Turns. *An Introduction to Combustion*. McGraw-Hill, New York, NY, 3 edition, 2007.
- [20] S. McAllister, J.Y. Chen, and A.C. Fernandez-Pello. *Fundamentals of Combustion Processes*. Springer, New York, NY, 2011.
- [21] J.S. Kim and F.A. Williams. Contribution of strained diffusion flames to acoustic pressure response. *Combustion and Flame*, 98:279–299, 1994.
- [22] W.C. Strahle. A theoretical study of droplet burning: Transient and periodic solutions. Technical report, National Aeronautics and Space Administration, 1963.
- [23] D.J. McKinney and D. Dunn-Rankin. Acoustically driven extinction in a droplet stream flame. *Combustion Science and Technology*, 161:24–48, 2000.
- [24] C.I. Sevilla-Esparza, J. L. Wegener, S. Teshome, J. I. Rodriguez, O. I. Smith, and A. R. Karagozian. Droplet combustion in the presence of acoustic excitation. *Combustion and Flame*, 161:1604–1619, 2014.
- [25] S.K. Kim, H.S. Choi, H.J. Kim, Y.S. Ko, and C.H. Sohn. Finite element analysis for acoustic characteristics of combustion stabilization devices. *Aerospace Science and Technology*, 42:229 – 240, 2015. ISSN 1270-9638.
- [26] J. O’Connor, V. Acharya, and T. Lieuwen. Transverse combustion instabilities: Acoustic, fluid mechanic, and flame processes. *Progress in Energy and Combustion Science*, 49:1–39, 2015. ISSN 0360-1285.

- [27] A. Miglani, S. Basu, and R. Kumar. Suppression of instabilities in burning droplets using preferential acoustic perturbations. *Combustion and Flame*, 161(12):3181–3190, 2014. ISSN 0010-2180.
- [28] H.Y. Wang, J.K. Bechtold, and C.K. Law. Forced oscillations in diffusion flames near diffusive-thermal resonance. *International Journal of Heat and Mass Transfer*, 51:630–639, 2008.
- [29] S. Kartheekyan and S.R. Chakvarthy. An experimental investigation of an acoustically excited laminar premixed flame. *Combustion and Flame*, 146: 513–529, 2006.
- [30] Q. Wang, H.W. Huang, H.J. Tang, M. Zhu, and Y. Zhang. Nonlinear response of buoyant diffusion flame under acoustic excitation. *Fuel*, 103:364–372, 2013.
- [31] Y. Hardalupas and A. Selbach. Imposed oscillations and non-premixed flames. *Progress in Energy and Combustion Science*, 28:75–104, 2002.
- [32] K. Deng, Z. Shen, M. Wang, Y. Hu, and Y.J. Zhong. Acoustic excitation effect on {NO} reduction in a laminar methane-air flame. *Energy Procedia*, 61:2890–2893, 2014. ISSN 1876–6102. International Conference on Applied Energy, {ICAE2014}.
- [33] L.W. Chen, Q. Wang, and Y. Zhang. Flow characteristics of diffusion flame under non-resonant acoustic excitation. *Experimental Thermal and Fluid Science*, 45:227–233, 2013.
- [34] Li-Wei Chen. Application of piv measurement techniques to study the characteristics of flame–acoustic wave interactions. *Flow Measurement and Instrumentation*, 45:308–317, 2015. ISSN 0955-5986.
- [35] F. Nicoud and T. Poinsot. Thermoacoustic instabilities: Should the rayleigh criterion be extended to include entropy changes? *Combustion and Flame*, 142:153–159, 2005.

- [36] S. Nair. *Acoustic characterization of flame blowout phenomenon*. PhD thesis, Georgia Institute of Technology, School of Aerospace Technology, May 2006.
- [37] W.W. Seto. *Schaum's Outline of Theory and Problems of Acoustics*. McGraw-Hill, New York, NY, 1<sup>st</sup> edition, 1971.
- [38] C.K. Law. *Combustion Physics*. Cambridge University Press, New York, NY, 2006.
- [39] A.C. Fernandez-Pello, S.R. Ray, and I. Glassman. Eighteenth symposium (international) on combustion flame spread in an opposed forced flow: the effect of ambient oxygen concentration. *Symposium (International) on Combustion*, 18(1):579 – 589, 1981. ISSN 0082-0784.
- [40] J.N. De Ris. Spread of a laminar diffusion flame. *Symposium (International) on Combustion*, 12(1):241 – 252, 1969. ISSN 0082-0784.
- [41] L. Hu, S. Liu, Y. Xu, and D. Li. A wind tunnel experimental study on burning rate enhancement behavior of gasoline pool fires by cross air flow. *Combustion and Flame*, 158(3):586 – 591, 2011. ISSN 0010-2180.
- [42] M.A. Fox and J. K. Whitesell. *Core Organic Chemistry*. Jones and Bartlett, Sudbury, MA, 1997.
- [43] M. Matalon. Lecture 8: Flame stretch and lewis number effects. <https://www.princeton.edu/cefric/Files/201120Lecture20Notes/Matalon/Lecture-8.pdf>, 2011.
- [44] H.W. Emmons. The film combustion of liquid fuel. *Z. angew. Math. Mech.*, 36:60–71, 1956.
- [45] V. Raghavan, A.S. Rangwala, and J.L. Torero. Laminar flame propagation on a horizontal fuel surface: Verification of classical emmons solution. *Combustion Theory and Modelling*, 13(1):121–141, 2009.

- [46] D.J. Rashbash. A flame extinction criterion for fire spread. *Combustion and Flame*, 26:411–412, 1976.
- [47] A. Tewarson. Generation of heat and chemical compounds in fires. In *SFPE Handbook*. National Fire Protection Association, Quincy, MA, third edition, 2002.
- [48] L. Hu, S. Liu, and L. Wu. Flame radiation feedback to fuel surface in medium ethanol and heptane pool fires with cross air flow. *Combustion and Flame*, 160(2):295–306, 2013.
- [49] NIST chemistry webbook. <http://webbook.nist.gov/chemistry/>. Accessed: 2015-07-12.
- [50] R. Arnold and W.E. Anderson. Droplet burning jp-8/silica gels. *48th AIAA Aerospace Sciences Meeting*, 48(421), 2010.
- [51] T. Edwards, B. Harrison, and L. Maurice. Properties and usage of air force fuel: Jp-8. In *39th Aerospace Sciences Meeting and Exhibit, AIAA, 2001*, volume 39 of *Aerospace Sciences Meeting*. American Institute of Aeronautics and Astronautics, August 2001.
- [52] T.J. Bruno, M. Huber, A. Laesecke, E. Lemmon, M. McLinden, S.L. Outcalt, R. Perkins, B.L. Smith, and J.A. Widegren. Thermodynamic, transport, and chemical properties of “reference” JP-8. Technical Report NISTIR 6659, National Institute of Standards and Technology, July 2010.
- [53] Defense Technical Information Center. DTIC-132106 (unclassified): Aviation fuel properties. Technical report, United States Department of Defense, 1983.
- [54] Exxon Mobile. World jet fuel specification. Technical report, 2005.
- [55] MIL-DTL-83133E Detail specification; turbine fuels, aviation, kerosene types, nato f-34 (jp-8), nato f-35, and jp-8+100. Technical report, United States Department of Defense, 2005.

- [56] D.B. Spalding. The combustion of liquid fuels. *Proc. 4th International Symposium on Combustion*, pages 847–864, 1953.
- [57] F.P. Incropera, David P. Dewitt, and et al. *Fundamentals of Heat and Mass Transfer*. John Wiley and Sons, Danvers, MA, 6 edition, 2007.
- [58] A.F. Miles. *Basic Heat and Mass Transfer*. Irwin, Inc., Chicago, IL, 1995.
- [59] J.F. Brady. Nusselt numbers of laminar, oscillating flows in stacks and regenerators with pores of arbitrary cross-sectional geometry. *Journal of the Acoustical Society of America*, 133(4):2004–2013, 2013.
- [60] B. Karlsson and J. Quintiere. *Enclosure Fire Dynamics*. CRC Press, Boca Raton, FL, 2000.
- [61] J. Borwick. *Loudspeaker and Headphone Handbook*. Focal Press, Oxford, third edition, 2001.
- [62] J. Volcler. *Extremely Loud: Sound as a Weapon*. The New Press, New York, NY, 2013.